

Doctoral Thesis

**Search for electromagnetic  
counterparts to neutrinos and  
gravitational waves**

**Searching for sources of astrophysical neutrinos and gravitational  
waves**

Robert Stein

April 29, 2021

Humboldt Universitaet Berlin

## **Disclaimer**

You can edit this page to suit your needs. For instance, here we have a no copyright statement, a colophon and some other information. This page is based on the corresponding page of Ken Arroyo Ohori's thesis, with minimal changes.

### **No copyright**

©⑧ This book is released into the public domain using the CC0 code. To the extent possible under law, I waive all copyright and related or neighbouring rights to this work. To view a copy of the CC0 code, visit:

<http://creativecommons.org/publicdomain/zero/1.0/>

### **Colophon**

This document was typeset with the help of **KOMA-Script** and **L<sup>A</sup>T<sub>E</sub>X** using the **kaobook** class.

The source code of this thesis is available at:

<https://github.com/robertdstein/kaobook>,

while the scripts used to generate the plots is available at:

[https://github.com/robertdstein/thesis\\_code](https://github.com/robertdstein/thesis_code)

The template is a modification of the open-source kaobook class, available at:

<https://github.com/fmarotta/kaobook>

### **Publisher**

First printed in Feb 2021 by Humboldt Universitaet Berlin

A neutrino is not a big thing to be hit by.  
In fact it's hard to think of anything much smaller by which  
one could reasonably hope to be hit. And it's not as if being  
hit by neutrinos was in itself a particularly unusual event for  
something the size of the Earth. Far from it. It would be an  
unusual nanosecond in which the Earth was not hit by  
several billion passing neutrinos.

*–The Hitchhiker's Guide to The Galaxy*



# Preface

I am of the opinion that every  $\text{\LaTeX}$  geek, at least once during his life, feels the need to create his or her own class: this is what happened to me and here is the result, which, however, should be seen as a work still in progress. Actually, this class is not completely original, but it is a blend of all the best ideas that I have found in a number of guides, tutorials, blogs and [tex.stackexchange.com](http://tex.stackexchange.com) posts. In particular, the main ideas come from two sources:

- ▶ Ken Arroyo Ohori's [Doctoral Thesis](#), which served, with the author's permission, as a backbone for the implementation of this class;
- ▶ The [Tufte-Latex Class](#), which was a model for the style.

The first chapter of this book is introductory and covers the most essential features of the class. Next, there is a bunch of chapters devoted to all the commands and environments that you may use in writing a book; in particular, it will be explained how to add notes, figures and tables, and references. The second part deals with the page layout and design, as well as additional features like coloured boxes and theorem environments.

I started writing this class as an experiment, and as such it should be regarded. Since it has always been intended for my personal use, it may not be perfect but I find it quite satisfactory for the use I want to make of it. I share this work in the hope that someone might find here the inspiration for writing his or her own class.

*Federico Marotta*

# Contents

Preface	v
Contents	vi
<b>AN INTRODUCTION TO MULTI-MESSENGER ASTRONOMY</b>	<b>1</b>
<b>NEUTRINO ASTRONOMY WITH ICECUBE</b>	<b>3</b>
<b>1 Statistical Analysis in IceCube</b>	<b>5</b>
1.1 Hypothesis Testing . . . . .	6
1.2 Null Hypothesis and Background Modelling . . . . .	7
1.3 Signal Hypothesis . . . . .	9
1.4 Likelihoods and Wilk's Theorem . . . . .	13
1.5 Pseudo-trials, P-values and trial corrections . . . . .	14
1.6 Sensitivities, Discovery Potentials and Upper Limits . . . . .	16
1.7 Stacking Multiple Sources . . . . .	19
1.8 Combining seasons . . . . .	20
1.9 Cluster-search algorithm . . . . .	20
1.10 Fitting the relative source weights . . . . .	22
1.11 Flarestack in practice . . . . .	22
<b>2 Neutrino Cosmology</b>	<b>25</b>
2.1 Cosmological Source Rates . . . . .	25
2.2 Differential flux and K-corrections . . . . .	27
2.3 Comparing Source Classes . . . . .	30
<b>3 Stacking Analyses with IceCube</b>	<b>35</b>
3.1 Tidal Disruption Events . . . . .	35
3.2 AT2018cow and FBOTs . . . . .	42
3.3 Robustness of Limits . . . . .	44
<b>OPTICAL FOLLOW-UP WITH ZTF</b>	<b>47</b>
<b>4 AT2019dsg</b>	<b>49</b>
4.1 Observations of AT2109dsg . . . . .	49
4.2 Probability of Chance Coincidence . . . . .	60
4.3 Neutrino production in AT2019dsg . . . . .	61
4.4 Compatibility with stacking limit . . . . .	65
4.5 Implications of AT2019dsg . . . . .	67
<b>CONCLUSION</b>	<b>69</b>

<b>APPENDIX</b>	<b>71</b>
A TDE Catalogue Results	73
Bibliography	77
Alphabetical Index	87

# List of Figures

1.2	Event rate as a function of $\sin(\delta)$ . . . . .	8
1.1	Rolling average of final-level event rate during detector uptime. . . . .	8
1.3	Declination-normalised event rate as a function of azimuth. . . . .	9
1.4	Background energy proxy distribution, normalised in bins of $\sin(\delta)$ . . . . .	9
1.5	Background energy proxy distribution, normalised in bins of azimuth. . . . .	9
1.6	Left: Declination-normalised MC rate as a function of azimuth. Right: Ratio of declination-normalised Signal and Background PDFs. . . . .	12
1.7	Left: Energy proxy distribution as a function of $\sin(\delta)$ , for various signal hypotheses. Right: Ratio of declination-normalised Signal and Background PDFs. . . . .	13
1.8	Background TS distribution for the standard Point Source Likelihood (Equation 1.17). . . . .	15
1.9	Background TS distribution for a Point Source Likelihood without an energy term. . . . .	15
1.10	Signal TS distribution for the standard Point Source Likelihood (Equation 1.17), with $\approx 3$ injected neutrinos. . . . .	16
1.11	Signal TS distribution for the Point Source Likelihood without an energy term, with $\approx 3$ injected neutrinos. . . . .	16
1.12	Sensitivity for the standard Point Source Likelihood (Equation 1.17), using the background TS distribution from Figure 1.8. . . . .	17
1.13	Sensitivity for the Point Source Likelihood without an energy term, using the background TS distribution from Figure 1.9. . . . .	17
1.14	$5\sigma$ Discovery Potential for the standard Point Source Likelihood (Equation 1.17), using background TS distribution from Figure 1.8. . . . .	17
1.15	$5\sigma$ Discovery Potential for the Point Source Likelihood without an energy term, using background TS distribution from Figure 1.9. . . . .	17
1.16	Effective area as a function of neutrino energy and declination. . . . .	18
1.17	Sensitivity and Discovery potential as a function of declination for an $E^{-2}$ spectrum. . . . .	18
1.18	Visualisation of a spatial PDF. . . . .	20
1.19	Visualisation of an energy proxy PDF. . . . .	20
1.20	Visualisation of the cluster search algorithm. . . . .	21
1.21	Estimated $5\sigma$ Discovery Potential for AT2018cow as a function of flare length, given in units of total fluence for an $E^{-2}$ spectrum over the 130 day search window. . . . .	21
2.1	Various transient rate densities as a function of redshift. . . . .	26
2.2	Various transient rates as a function of redshift. . . . .	27
2.3	Contributed flux at earth as a function of redshift. . . . .	30
2.4	Cumulative flux at earth as a function of redshift. . . . .	30
2.5	CDF as a function of spectral index for TDEs. . . . .	30
2.6	CDF as a function of source evolution. . . . .	30
2.7	Completeness correction factor as a function of source evolution. . . . .	31
2.8	$N_{sig}$ vs $N_{bkg}$ . . . . .	32
2.9	Statistical significance of excess coincidence as a function of number of follow-up . . . . .	33

3.1	Limits on the neutrino emission for each catalogue. . . . .	39
3.2	Limits on the contribution of jetted and non-jetted TDEs to the diffuse neutrino flux. . . . .	40
3.3	Limits on the contribution of jetted and non-jetted TDEs to the diffuse neutrino flux, under the assumption of a source evolution proportional to the Star Formation Rate. . . . .	41
3.4	Limits on neutrino emission from AT2018cow, as a function of spectral index.	43
3.5	Limits on neutrino emission from FBOTs, using the limits from AT2018cow under the assumption of neutrino standard candles. . . . .	44
3.6	Sensitivity of the Point Source Likelihood for a point source as a function of energy. . . . .	45
4.1	Visualisation of IC191001A in the IceCube detector. The colour corresponds to the light arrival time, from early orange pulses on the left to late blue ones on the right. The arrow illustrates the best fit reconstructed trajectory of the event. . . . .	50
4.2	UV/Optical photometry of AT2019dsg. The vertical dotted line illustrates the arrival of IC191001A. . . . .	50
4.3	X-ray lightcurve of AT2019dsg. The vertical dotted line illustrates the arrival of IC191001A. . . . .	52
4.4	X-ray count map from <i>XMM-Newton</i> (50 days after discovery). The yellow circle indicates the source region, while the blue circular region was used to measure the background. . . . .	52
4.5	Soft X-ray spectrum of AT2019dsg measured by <i>XMM-Newton</i> , fitted with an absorbed disk blackbody model. . . . .	53
4.6	Radio observations of AT2019dsg. . . . .	53
4.7	Inferred energy of the synchrotron-emitting outflow of AT2019dsg. . . . .	55
4.8	Inferred radius of the synchrotron-emitting outflow of AT2019dsg. . . . .	56
4.9	LAT counts map of the Region Of Interest (ROI) in the integrated search period G3, showing the IC191001A 90% localisation region in orange. The neutrino best-fit position is marked with a orange ‘x’. . . . .	57
4.10	LAT lightcurve for the source <i>Fermi</i> -J2113.8+1120 in the time interval G3, with evenly spaced binning of 28 days. Vertical error bars represent $1\sigma$ intervals, horizontal bars denote bin width. $2\sigma$ upper limits are shown for bins with $TS \leq 9$ . The orange dashed vertical line marks the arrival time of IC-191001A.	58
4.11	The spectroscopic evolution of AT2019dsg, beginning with the publicly available classification spectrum taken with the NTT [164], and further spectra from LDT, Lick, Keck and P200. The Balmer lines are highlighted in cyan, the HeII lines in gray, and the Bowen fluorescence lines (OIII at 3760Å, NIII at 4100Å and 4640Å) in black. Telluric lines are marked with +. . . . .	59
4.12	Left: temporal evolution of the three emission zones for AT2019dsg. Right: Illustration of the geometry of these three zones. . . . .	61
4.13	Cumulative distribution function (CDF) for TDE neutrino emission as a function of redshift, with the CCSN CDF plotted for comparison. . . . .	66

## List of Tables

2.1	Summary of assumptions on source classes. . . . .	31
-----	---	----

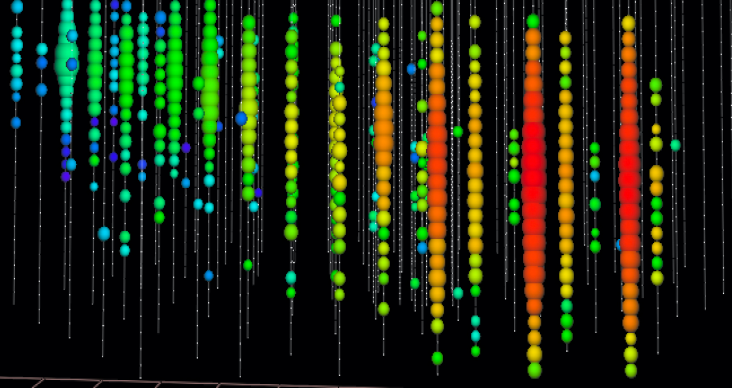
3.1	Summary of the four TDE catalogues. . . . .	37
3.2	Summary of results for the four TDE catalogues. For each, an independent stacking analysis was performed. The catalogues covered sources from May 2008 to October 2017, matching the IceCube data-taking period. . . . .	38
3.3	Summary of the five individual TDEs for which the temporal-cluster-search method was applied. All but AT2018cow were included in the stacking analysis. . . . .	42
4.1	Peak frequency and peak flux density of the radio observations. . . . .	54
4.2	Summary of the synchrotron modelling for the <i>equipartition case</i> . All inferred properties are given in $\log_{10}$ scale, with errors given in brackets. . . . .	55
4.3	Summary of the synchrotron modelling with the inclusion of protons. All inferred properties are given in $\log_{10}$ scale, with errors given in brackets. . . . .	55
4.4	Gamma-ray energy flux upper-limits for a point-source with power-law index $\Gamma=2.0$ at the position of AT2019dsg integrated over the analysis energy range 0.1-800 GeV. . . . .	57
A.1	Summary of the Jetted TDE catalogue. . . . .	73
A.2	Summary of the Golden TDE catalogue. . . . .	74
A.3	Summary of the Silver TDE catalogue. . . . .	74
A.4	Summary of the Obscured TDE catalogue. . . . .	75

**AN INTRODUCTION TO  
MULTI-MESSENGER ASTRONOMY**



# **NEUTRINO ASTRONOMY WITH ICECUBE**





# 1 Statistical Analysis in IceCube

“ Every experiment may be said to exist only in order to give the facts a chance of disproving the null hypothesis. ”

Ronald Fischer, *The Design of Experiments*, 1935

As a field, Neutrino Astronomy is still very much in its infancy. While most branches of astronomy are focussed on characterising the properties of astrophysical objects, neutrino astronomy primarily seeks to just identify such objects in the first place. Given the characteristic signal-to-noise of neutrino detectors, determined by their limited resolution and event rate with an enormous atmospheric background, a significant fraction of correlations in data will be due simply to background fluctuations. This statement applies both to clustering within the neutrino data, and to correlations between neutrinos and external data.

Neutrino astronomy is thus predominantly a process of statistical analysis, seeking both to identify correlations and to evaluate whether these are coincidental or physical. As introduced in Chapter ??, we have access to three key observables when performing this analysis with IceCube:

- ▶ **Event arrival time**,  $t$ , with nanosecond precision.
- ▶ **Reconstructed direction**, zenith ( $\theta$ ) and azimuth ( $\phi$ ), in local detector coordinates. This quantity has a significant uncertainty, which can also be estimated, providing an additional observable ( $\sigma$ ). The reconstructed direction, in combination with the time, can be uniquely mapped to celestial coordinates Right Ascension ( $\alpha$ ) and Declination ( $\delta$ ).
- ▶ **Event energy proxy**,  $E_p$ . It can be converted through *unfolding* to give a probability distribution of true neutrino energies, but this requires certain assumptions about the underlying neutrino spectrum and retains typical uncertainties of factor 10.

This chapter outlines the process by which these observables are analysed, and correlations are established. A software designed to perform

1.1 Hypothesis Testing . . . . .	6
1.2 Null Hypothesis and Background Modelling . . . . .	7
1.3 Signal Hypothesis . . . . .	9
1.4 Likelihoods and Wilk’s Theorem . . . . .	13
1.5 Pseudo-trials, P-values and trial corrections . . . . .	14
1.6 Sensitivities, Discovery Potentials and Upper Limits .	16
1.7 Stacking Multiple Sources .	19
1.8 Combining seasons . . . . .	20
1.9 Cluster-search algorithm .	20
1.10 Fitting the relative source weights . . . . .	22
1.11 Flarestack in practice . . . . .	22

[106]: Stein et al. (2020), [icecube/flarestack](#)

such analysis, `flarestack`, was developed by the author to study correlations in IceCube data [106].

## 1.1 Hypothesis Testing

Neutrino Astronomy with IceCube uses a *Frequentist* approach to statistical inference, and in particular uses the method of *statistical hypothesis testing* to establish correlations. Statistical hypothesis testing begins with the definition of a particular hypothesis to test,  $\mathcal{H}_1$ , and a null hypothesis,  $\mathcal{H}_0$ , that would be expected in the absence of any correlation. Ultimately, we wish to determine which hypothesis better describes our data. Hypothesis testing adopts the default position that the null hypothesis describes the data, and evaluates whether this description can be disproven. We define a test statistic (TS) to quantify how well data is described, and define a threshold at which we would be confident in reaching a conclusion. If our test statistic exceeds this threshold, we *reject the null hypothesis*. This means we are confident that the null hypothesis does not describe our data. It does not necessarily follow that our signal hypothesis is correct, we can only say that it better describes our data than the null hypothesis. Conversely, if the TS does not exceed the threshold, we *do not reject the null hypothesis*. In this case, we are not confident that the null hypothesis does not describe our data. This does not mean that the signal hypothesis is wrong, but rather that we cannot be sure the null hypothesis is wrong.

**Table 1.1:** Hypothesis Testing

	not rejected	rejected
$\mathcal{H}_0$ true	✓	Type I
$\mathcal{H}_0$ false	Type II	✓

As illustrated in Table 1.1, there are two things that can go wrong with a hypothesis test. Type I error, or a false positive, occurs when we reject the null hypothesis although it is true. Type II error, or a false negative, occurs when we do not reject the null hypothesis even though it is false. By construction, every test must balance the risk of Type I and Type II errors, and both cannot be eliminated simultaneously. We typically construct our test by fixing a threshold for acceptable rate of Type I error. This Type I error rate is quantified by a *p-value*, defined as the probability of observing a result under the null hypothesis that is at least as significant as the one found. One common p-value threshold is 0.05, i.e. only accepting results with a probability  $< 5\%$  to arise under the null hypothesis. The p-value can also be converted to a *significance*, equal to the number of standard deviations required for a one-sided Gaussian distribution to yield that p-value. A typical threshold for a discovery, common in particle physics, is  $5\sigma$ . This corresponds to a p-value of less than  $3 \times 10^{-7}$ .

While the simplest hypothesis test is a binary case in which one well-defined hypothesis  $\mathcal{H}_1$  is compared to the null hypothesis, the procedure is often generalised to cover multiple hypotheses,  $\mathcal{H}_i$ , which can be either discrete or continuous. We pick the hypothesis with the smallest p-value, and compare that to our null hypothesis.

## 1.2 Null Hypothesis and Background Modelling

For neutrino astronomy, the null hypothesis is that *events are distributed according to the background model*. At the stage of defining background models, IceCube-specific physics is added to the pure mathematical basis of hypothesis testing. As outlined in Chapter ??, IceCube data in the northern hemisphere is dominated by the *atmospheric neutrino background*, while events in the southern hemisphere are dominated by *atmospheric muon bundles*, and in both hemispheres the astrophysical neutrino component is subdominant. This astrophysical neutrino flux likely consists of components from multiple source classes, so there is in principle an additional *astrophysical background* for contributions not included in the signal hypothesis.

It is common in IceCube to take the simplifying assumption that *the data is sufficiently background-dominated to be used as a background model*. The motivation is twofold, it is firstly approximately true, but more importantly the colossal muon rate ( $\sim 3\text{kHz}$ ) makes it very difficult to simulate the small fraction of muons which form a signal-like background for the southern hemisphere [107]. In the absence of any adequate simulated model for background in the southern hemisphere, we are forced to instead use a data-based model as a null hypothesis.

The simplification has a number of drawbacks, primarily that Probability Density Functions (PDFs) derived from data are necessarily coarser because the available statistics are limited. An alternative approach, used for the sample of northern through-going muons tracks in which there is negligible atmospheric muon background, is to use Monte-Carlo based modelling to construct a model for background [108]. This ultimately introduces the risk of data-MC disagreement, with uncertainties introduced for example with by atmospheric and astrophysical flux modelling. However, this is typically offset by the high-resolution PDFs which can be constructed using these much larger sample sizes.

In either case, distributions are then constructed for the background model  $\mathcal{B}$ . Using our observables, we can construct a composite background model consisting of a spatial, temporal and energy component:

$$\mathcal{B}(t, \theta, \phi, \sigma, E_p) = \mathcal{B}_{\text{time}} \times \mathcal{B}_{\text{space}} \times \mathcal{B}_E \quad (1.1)$$

In the following, data-based background PDFs are illustrated for the IceCube all-sky ten year point source dataset ('ps tracks version v003-p02') [95].

### Background Time PDF

The IceCube detector is characterised by extremely high uptime of >99%, divided into runs separated by small downtime breaks. Even after processing to final-level event selections, samples typically consists of live-time at >90%, with the remaining time lost to partial detector operation, testing or temporary DOM failure. The arrival time of background events in Icecube is typically *assumed to be uniform during detector uptime*. This is again only approximately true, as evidenced by Figure 1.1. Six peaks

[107]: Aartsen et al. (2017), "The IceCube Neutrino Observatory: Instrumentation and Online Systems"

[108]: IceCube Collaboration et al. (2018), "Search for steady point-like sources in the astrophysical muon neutrino flux with 8 years of IceCube data"

[95]: Aartsen et al. (2020), "Time-Integrated Neutrino Source Searches with 10 Years of IceCube Data"

[109]: Heix et al. (2019), “Seasonal Variation of Atmospheric Neutrinos in IceCube”

corresponding to winters in the northern hemisphere are clearly visible, corresponding to  $\pm \sim 5\%$  rate variations.

The atmospheric background rates depend on atmospheric densities which are ultimately temperature-dependent, leading to seasonal variations and clearly-visible annual cycles. This variation is itself an area of scientific interest, being exploited to measure climate variations with neutrinos [109]. These effects are partially mitigated in data-based models by the standard method of shuffling measured neutrino arrival times rather than drawing them from a PDF. In any case, the arrival time anisotropy is a small one.

Given this, we can approximate the background time PDF as uniform over periods of detector operation, with normalisation:

$$\mathcal{B}_{\text{time}} \approx \frac{1}{\text{livetime}} \quad (1.2)$$

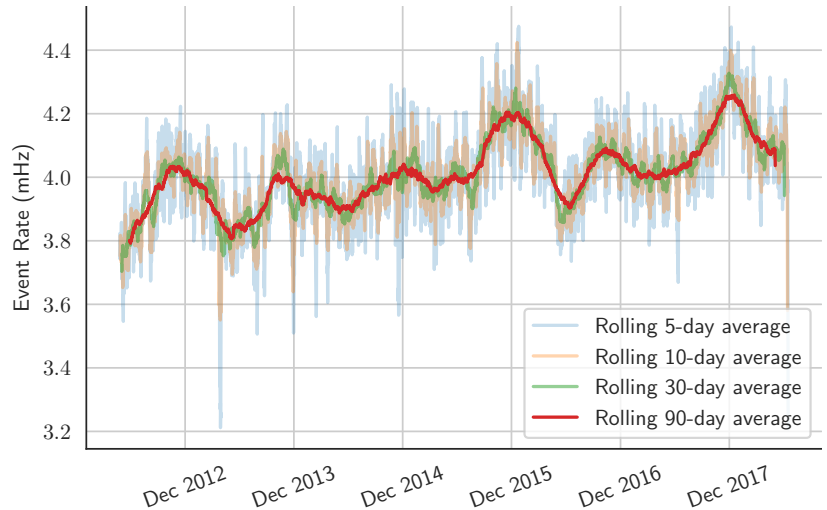


Figure 1.1: Rolling average of final-level event rate during detector uptime.

## Background Spatial PDF

The spatial distribution of the background can be neatly factorised into two distinct components, namely a zenith and an azimuth component:

$$\mathcal{B}_{\text{space}}(\theta, \phi) = \mathcal{B}_\theta(\theta) \times \mathcal{B}_\phi(\phi, \theta) \quad (1.3)$$

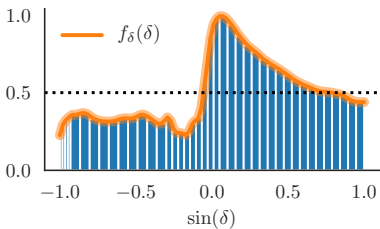


Figure 1.2: Event rate as a function of  $\sin(\delta)$ .

Owing to IceCube’s convenient location at the geographic south pole, the zenith-dependent detector response can be uniquely mapped into a declination-dependent one. With a data-driven background model, we can define a PDF  $f_\delta(\delta)$  based on the declination-dependent event rate, as seen in Figure 1.2.

$$\mathcal{B}_\delta(\delta) = f_\delta(\delta) \quad (1.4)$$

The additional azimuthal component can be seen in Figure 1.3. The detector itself (see Chapter ??) has 6 string axes, and these are clearly visible with elevated event rates. These variations reach up to  $\sim 40\%$  variations

for the southern hemisphere. Additionally, the impact of *ice anisotropy* can be seen from an event rate deficit at and below the horizon [110], aligned with the axes of maximal charge deficit at  $\sim 2\pi/3$  and  $5\pi/3$ .

However, string axes will all be traced out over the course of each day. Thus, for typical data periods of many years, these azimuthal variations will be averaged out. It is therefore typically assumed that *any variations due to azimuthal asymmetry are negligible*. An exception must be made for searches targeting clustering over short (sub-day) time periods, where this azimuthal asymmetry may have an impact. Beyond this, as long as the azimuth asymmetry can be neglected, we then find that the distribution in right ascension is uniform:

$$\mathcal{B}(\alpha) = \frac{1}{2\pi} \quad (1.5)$$

By substituting Equations 1.4 and 1.5, we can then replace Equation 1.3 with:

$$\mathcal{B}_{\text{space}}(\delta) = \frac{1}{2\pi} \times f(\delta) \quad (1.6)$$

## Background Energy PDF

Having factorised the declination dependence of events in equation 1.4, we can then consider the expected energy proxy distribution for a given spatial position. The normalised energy proxy distribution as a function of  $\sin(\delta)$  is given in Figure 1.4, with the median and central 90% ranges marked by dotted lines. It is clear that in the northern hemisphere, this distribution is essentially flat, reflecting the homogeneity of atmospheric neutrino backgrounds in this regime. However, the median energy proxy swiftly increases into the southern hemisphere, as more aggressive cuts are employed to remove the additional atmospheric muon background. The final turnover at the pole reflects the impact of the IceTop surface detector, which can be used to veto muon bundles from vertically-inclined showers.

In contrast to the strong declination dependence, Figure 1.5 shows that there is no azimuthal dependence for events in the northern hemisphere, and negligible variation in the southern hemisphere. We can thus construct simple two-dimensional background energy PDFs using the distribution shown in Figure 1.4:

$$\mathcal{B}_E(\delta, E_{\text{proxy}}) = f_E(E_{\text{proxy}}, \delta) \quad (1.7)$$

## 1.3 Signal Hypothesis

Signal hypotheses in IceCube are a composite of the background model with a small number of additional signal-like neutrinos ( $n_s$ ). It is assumed that *the total number of neutrino events is essentially fixed by background*,

[110]: Chirkin et al. (2019), “Light diffusion in birefringent polycrystals and the IceCube ice anisotropy”

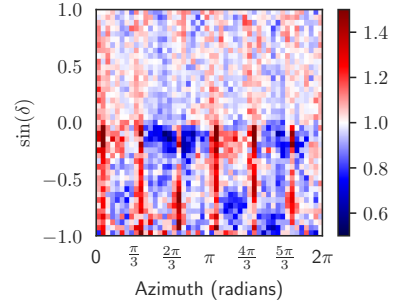


Figure 1.3: Declination-normalised event rate as a function of azimuth.

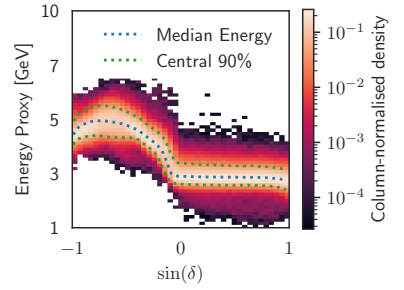


Figure 1.4: Background energy proxy distribution, normalised in bins of  $\sin(\delta)$ .

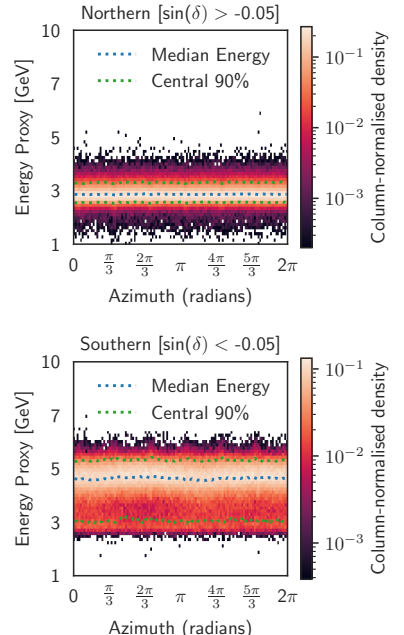


Figure 1.5: Background energy proxy distribution, normalised in bins of azimuth.

so that  $N = n_s + n_b$ . In this case, we define our signal hypothesis as the normalised sum of a background PDF  $\mathcal{B}$  and signal PDF  $\mathcal{S}$ :

$$\mathcal{H} = \frac{n_s}{N} \mathcal{S} + \frac{N - n_s}{N} \mathcal{B} \quad (1.8)$$

Much like the background, the signal PDF is a product of energy, temporal and spatial PDFs:

$$\mathcal{S} = \mathcal{S}_{\text{time}} \times \mathcal{S}_{\text{space}} \times \mathcal{S}_{\text{E}} \quad (1.9)$$

In IceCube, it is common to test hypotheses in which the number of signal neutrinos,  $n_s$ , is a free parameter. It is also common to assume that the intrinsic signal energy PDF is an unbroken power law with some spectral index,  $E^{-\gamma}$ , where the spectral index  $\gamma$  is an additional free parameter.

## Signal Time PDF

In almost all IceCube analyses, the signal time PDF is assumed to be a uniform distribution over a fixed period of livetime. This could be for the entire duration of a dataset, corresponding to a steady neutrino source. This special case is typically referred to as a *time-integrated analysis*, because it cancels out exactly the assumed background time PDF, yielding a likelihood that does not depend on time. This thesis is concerned with *transient* sources, which are only active over fixed periods of time. Transient source hypotheses require a *time-dependent analysis*, in which the signal is not assumed to be uniform over the full data-taking duration.

The uptime of the detector can be characterised by a boolean detector response function,  $f_{\text{uptime}}(t)$ , that is either on (1) or off (0). The signal time PDF is then a product of the underlying source PDF and this detector response PDF. For this thesis, the only relevant transient time PDF was a simple *box model*. This is a uniform signal normalised over the livetime,  $\Delta_T$ , between start time  $T_0$  and end time  $T_1$ :

$$\Delta_T = \int_{T_0}^{T_1} f_{\text{uptime}}(t) dt \quad (1.10)$$

$$\mathcal{S}_{\text{time}}(t) = \begin{cases} f_{\text{uptime}}(t) \times \frac{1}{\Delta_T} & T_0 < t < T_1 \\ 0 & \text{otherwise} \end{cases} \quad (1.11)$$

## Signal Spatial PDF

The standard spatial signal PDF is typically stated to be *the assumption of a circular Gaussian PSF centered on the position of a source*. For an event at  $\vec{x}$  with a localisation uncertainty  $\sigma$  and a source at position  $\vec{d}$ , we then have:

$$r^2 = (\vec{x} - \vec{d})^2 \quad (1.12)$$

$$\mathcal{S}_{\text{space}}(\vec{x}) = \frac{1}{2\pi\sigma^2} e^{-r^2/2\sigma^2} \quad (1.13)$$

In reality, even under the limit of a perfect muon track reconstruction, the unmeasurable energy-dependent kinematic angle between the incoming neutrino and outgoing muon will limit the resolution of any search. The signal PSF thus depends on the signal hypothesis, where higher-energy neutrinos are better reconstructed even for fixed  $\sigma$ .

Ultimately, the performance of directional reconstructions is verified on MC events, and energy-dependent biases in uncertainty estimates are corrected in a process known as pull corrections (see Chapter ??). So, more precisely, the signal spatial PDF is *assumed to follow the distribution found in baseline MC simulations weighted with an unbroken  $E^{-2}$  power law*, and further *it is assumed that this distribution can be approximated by a circular Gaussian PSF with a single per-event energy-corrected uncertainty parameter*. The first assumption clearly requires that the impact of systematic uncertainties on MC simulation is negligible. The validity of these assumptions is discussed further in Chapter N, but it should be noted that neither approximation is completely valid.

A Gaussian term for the spatial PDF also indirectly *assumes that the Signal PDF does not depend on azimuth*. It is clear in the left panels of Figure 1.6 that azimuthal asymmetry is increasingly visible for soft spectra in the northern hemisphere, and approximately resembles the pattern seen in Figure 1.3. However, for both the southern sky and a hard  $E^{-1}$  spectrum, there is no such asymmetry. As can be clearly seen in Figure 1.7, these corresponds to regimes where the signal is dominated by high-energy events. In general, *the effective area at lower energies is azimuth-dependent, while at higher energies it is approximately uniform*. This is because, at lower energies, only tracks which pass close to the DOMs will be detected. In any case, as can be seen in the right-hand panels of Figure 1.6, azimuth has very little discriminating power for any spectral index, and can thus be safely neglected for analysis.

## Signal Energy Proxy PDF

The energy PDF is most commonly *assumed to be an unbroken power of index  $\gamma$  extending over the entire energy range of sensitivity for the IceCube detector*, namely from 100 GeV to 10 PeV. This energy spectrum is then convolved with the detector response function through use of weighted MC simulation, yielding an expected distribution of energy proxy values:

$$\mathcal{S}_E(\delta, E_p, \gamma) = f_E(\delta, E_p, \gamma) \quad (1.14)$$

An illustration of the expected signal distribution, derived from MC for a range of spectral indices, is illustrated in the left panels of Figure 1.7. It is clear that hard spectra result in events with energies substantially above those expected in background, but for softer spectra the distribution narrows and is much more similar to that in Figure 1.4. Much of the discriminating power in IceCube comes from the identification

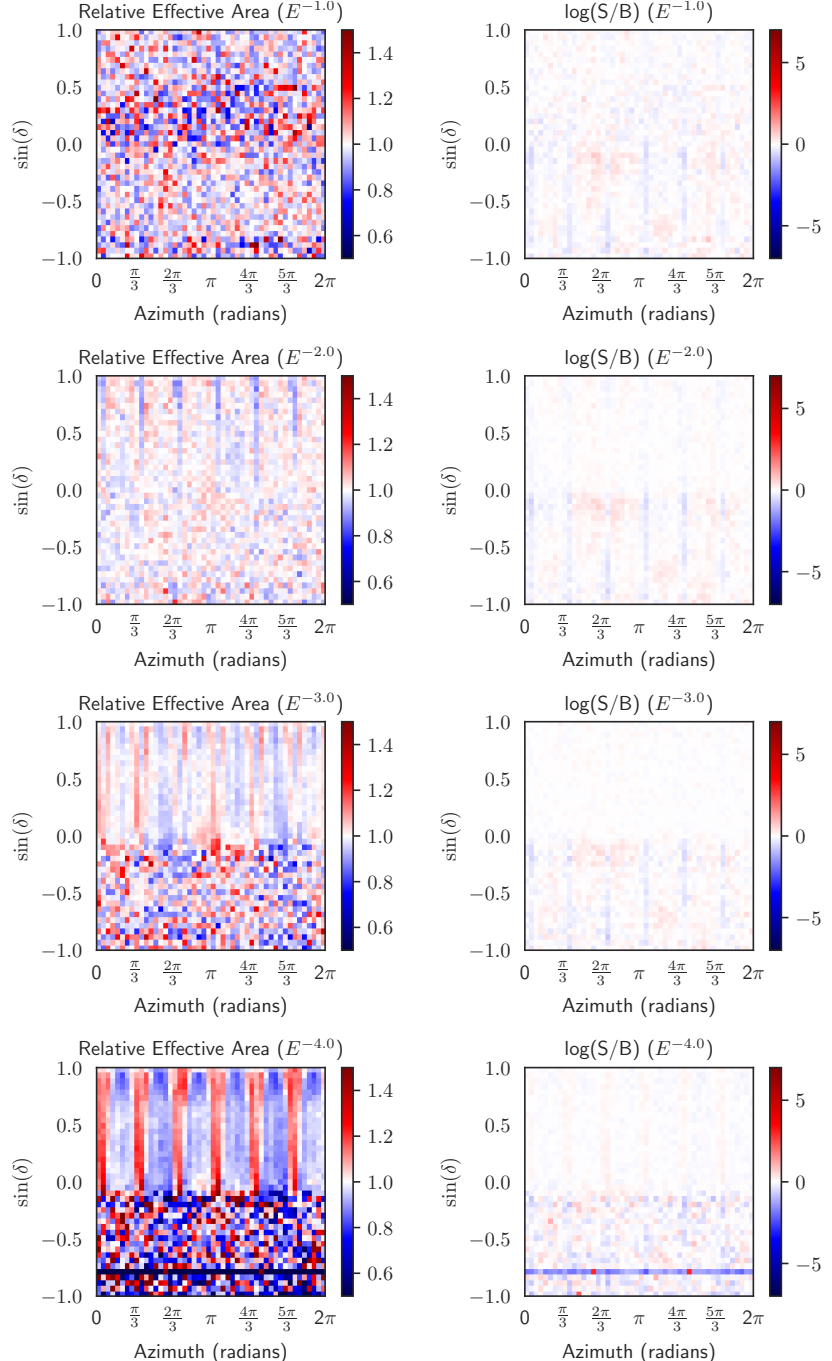


**Figure 1.6:** Left: Declination-normalised MC rate as a function of azimuth. Right: Ratio of declination-normalised Signal and Background PDFs.

of these high-energy neutrinos, which are unlikely to arise from atmospheric backgrounds but should arise from hard  $\sim E^{-2}$  spectra expected for most astrophysical neutrino sources.

Similar to the spatial PDF, the signal energy proxy PDF *ultimately assumes that the baseline MC accurately describes the expected energy proxy distribution*. This again implicitly assumes that systematic uncertainties have a negligible impact on energy proxy distributions.

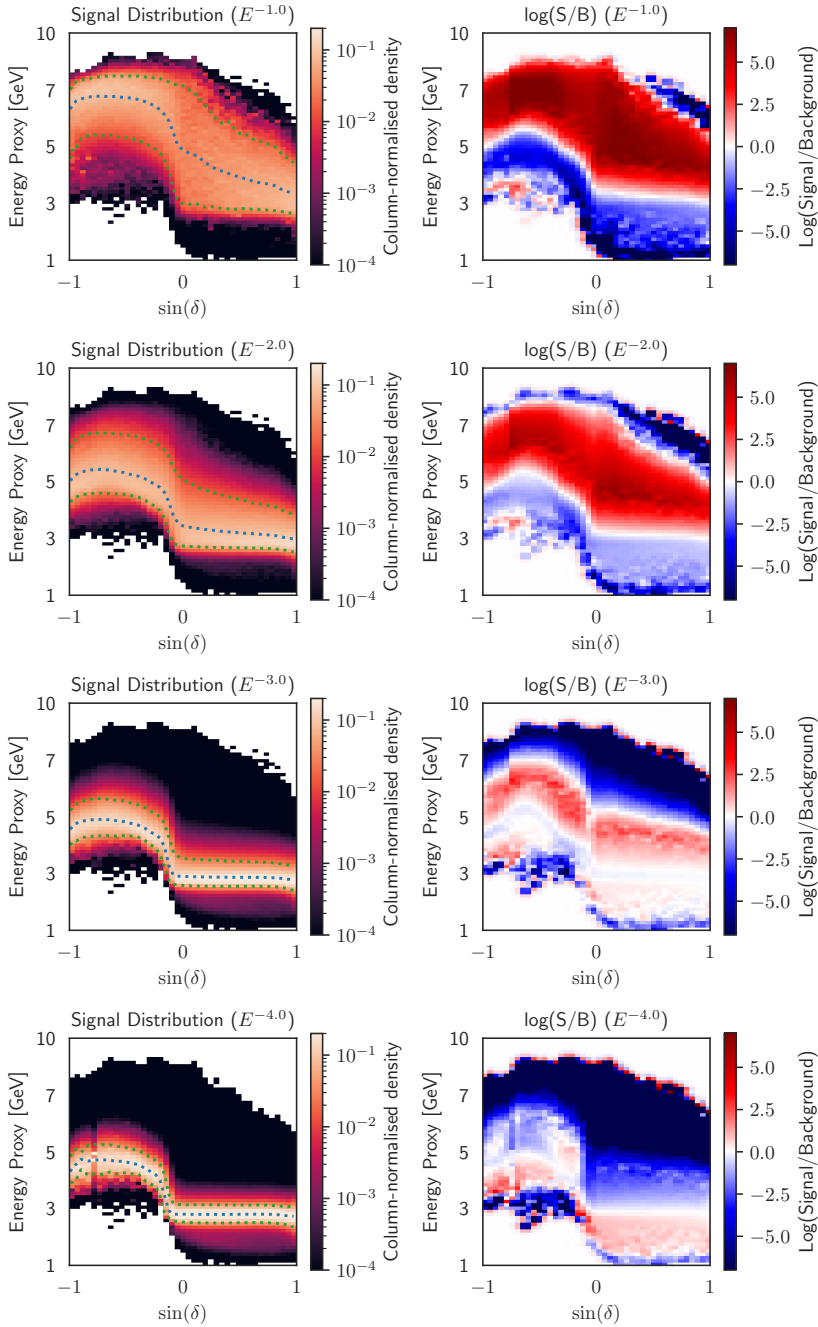


**Figure 1.7:** Left: Energy proxy distribution as a function of  $\sin(\delta)$ , for various signal hypotheses. Right: Ratio of declination-normalised Signal and Background PDFs.

## 1.4 Likelihoods and Wilk's Theorem

One method of quantifying agreement between a hypothesis and data is to calculate the *likelihood*,  $\mathcal{L}$ , of observing our data given that hypothesis. Using the PDFs describing how we would expect observables to be distributed for each hypothesis, we can calculate the conditional probability,  $\mathcal{L}(x|\mathcal{H})$ , of observing our data  $x$  given that hypothesis. The likelihood values can be used to construct a test statistic:

$$TS(\mathcal{H}_i) = 2 \log \left( \frac{\mathcal{L}(x|\mathcal{H}_i)}{\mathcal{L}(x|\mathcal{H}_0)} \right) \quad (1.15)$$

The primary motivation for using this test statistic definition comes from

[111]: Neyman et al. (1933), “On the Problem of the Most Efficient Tests of Statistical Hypotheses”

[112]: Braun et al. (2008), “Methods for point source analysis in high energy neutrino telescopes”

the *Neyman-Pearson Lemma* [111], which states that the likelihood ratio test is the most powerful possible statistical test.

While this TS definition could be used for a likelihood that is evaluated for discrete regions of parameter space (a *Binned likelihood analysis*), it has long been customary in IceCube to instead evaluate the likelihood in a continuous event-wise fashion (an *Unbinned likelihood analysis*) [112]. A likelihood is constructed, and evaluated for each  $j$ th individual event, with the overall likelihood given by the product of these  $N$  independent events:

$$\mathcal{L} = \prod_i^N \mathcal{L}_i \quad (1.16)$$

Ultimately this yields the standard *Point Source Likelihood*:

$$\mathcal{L}(n_s, \gamma) = \prod_i^N \left( \frac{n_s}{N} \mathcal{S}(\theta_i, \gamma) + \frac{N - n_s}{N} \mathcal{B}(\theta_i) \right) \quad (1.17)$$

We are thus testing a continuum of hypotheses parameterised by  $n_s$  and  $\gamma$ , where both  $\mathcal{S}$  and  $\mathcal{B}$  depend on the event-specific observables  $\theta_j$ . We typically construct the negative log likelihood ( $-\log \mathcal{L}$ ), and then derive best-fit parameters  $\hat{n}_s$  and  $\hat{\gamma}$  by a process of maximum likelihood estimation. We take the combination of parameters which maximises the likelihood, and use this as our final TS value.

## 1.5 Pseudo-trials, P-values and trial corrections

Given a particular TS value, we must then calculate a p-value to quantify whether or not the null hypothesis can be rejected. The most simplistic method is to perform simulated *pseudo-experiments* based on the null hypothesis, to quantify how often a given outcome occurs. This method critically relies on the assumption that *pseudo-experiments can be accurately simulated, and thus represent the expected distribution*.

Much like for Section 1.2, the null distribution can be simulated using either a data-based or MC-based model. In general, for any point source analysis, data-based methods perform well because the datasets are indeed background-dominated. Furthermore, the data can be easily randomised through use of *data-scrambling*, in which the detector symmetry is exploited by randomly assigning new values of right ascension to events. Furthermore, relying on the assumption that *the dataset is background-dominated at all relevant timescales*, the temporal variations of the background shown in Figure 1.1 can easily be accounted for by randomly reassigning the arrival time of events to other events. These methods work principally because a point source analysis is concerned with only a tiny fraction of the data, in a narrow right ascension/declination range, and thus the broader population distribution is almost completely independent of any signal hypothesis. Alternatively using MC-based models ensures there is absolutely no contamination of the background distribution with signal, but comes at the cost of introducing a dependence on the data-MC agreement for any subsequent conclusions.

An alternative method of calculating a p-value is to exploit Wilk's *Theorem* [113]. Wilk's Theorem states that the log likelihood ratio for an ensemble of datasets will be distributed according to a  $\chi^2$  distribution, with degrees of freedom equal to the number of independent parameters. Thus, for a hypothesis depending on a known number of independent parameters, we can analytically convert any TS value to a *p-value*. There are, however, caveats to Wilk's Theorem. The full formulation only applies in the limit of large samples, and in the absence of bounds on fit parameters. In IceCube this condition is usually satisfied, but there are exceptions particularly for searches on short-timescales relevant for GRB or FRB searches, where the data transitions from a background-dominated regime to a background-free one.

For most cases, including all analysis for this thesis, a hybrid approach is used. A large number of pseudotrials are generated, providing an ensemble of TS values. A  $\chi^2$  distribution is then fit to this dataset, with the degrees of freedom and normalisation being free parameters. This fitted distribution can then be used to extrapolate from the experimental distribution (typically several hundred thousand) to even smaller p-values, such as for the  $5\sigma$  TS value which would otherwise require several million trials.

An example distribution, for a source at the horizon, is illustrated in Figure 1.8. It is well-fit by the  $\chi^2$  distribution, with  $\sim 1.4$  degrees of freedom. Though this may appear to be unphysical, it illustrates the fact that the likelihood outlined in Equation 1.17 does not have two independent fit parameters. Rather, given that PS analyses search primarily for an excess of high-energy neutrinos,  $n_s$  and  $\gamma$  are in fact degenerate to a large degree. From the perspective of a likelihood analysis, a single high-energy neutrino on top of an abundant low-energy background does not appear very different to a single high-energy neutrino with a handful of lower-energy neutrinos against an abundant low-energy background. As can be seen in Figure 1.9, for a Point Source Likelihood without energy terms, the TS distribution is well fit by a  $\chi^2$  distribution with exactly 1 degree of freedom, as expected for a likelihood that depends only on  $n_s$ .

For a single hypothesis, the procedure would then be complete. However, it is common that multiple hypotheses are tested at once, for example in this thesis with multiple catalogues (see Chapter 3). Given that each independent test has a probability to randomly produce an overfluctuation, smaller p-values become increasingly likely as more tests are added. To counteract the multiple hypothesis problem, known as the *look-elsewhere effect*, a correction must be introduced, known as a *trial factor*. The trial factor quantifies the number of independent tests that have been performed, and thus quantifies how likely it is to find a small p-value. If the smallest pre-trial p-value is  $p_{\text{pre-trial}}$ , then for  $N$  independent trials we find:

$$p_{\text{post-trial}} = 1 - (1 - p_{\text{pre-trial}})^N \quad (1.18)$$

Defining what constitutes an independent trial can be difficult. It is a common misconception that the trial factor is particularly important for cases when two hypotheses are similar. In the limit that two hypotheses are so similar as to be essentially identical, there would be no need for

[113]: Wilks (1938), "The Large-Sample Distribution of the Likelihood Ratio for Testing Composite Hypotheses"

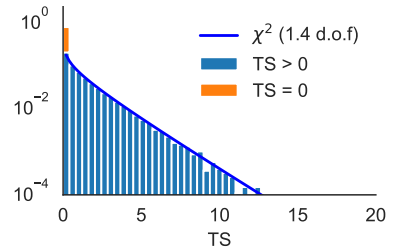


Figure 1.8: Background TS distribution for the standard Point Source Likelihood (Equation 1.17).

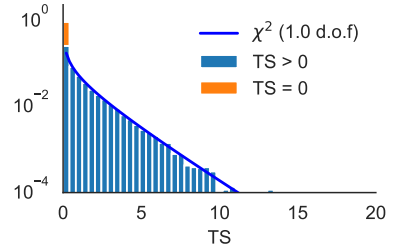


Figure 1.9: Background TS distribution for a Point Source Likelihood without an energy term.

a trial correction at all, since the test statistic for each would be identical. The trial factor should correct the degree to which hypotheses are capable of giving multiple independent TS values. Distinct catalogues which do not share sources are completely independent trials, and thus  $N$  is simply the number of source lists tested. For correlated tests, such as overlapping catalogues or identical catalogues with different intrinsic source weighting, the trial factor will always be smaller than the number of tests but there is no analytic solution to the exact factor. Instead, it can in principle be derived experimentally, by performing all tests on each pseudo-trial, and considering the distribution of smallest p-values. In this thesis, the conservative approach is employed instead, by counting tests and assuming they are independent.

## 1.6 Sensitivities, Discovery Potentials and Upper Limits

When developing and performing statistical analysis, we often wish to quantify how powerful a particular test is. As an extension of the background pseudo-experiments outlined in Section 1.5, we can also perform pseudo-experiments with our signal hypothesis. This is done through the process of *signal injection*, whereby a pseudo-dataset is constructed using a combination of the background model and a signal model. The resulting TS distribution, and all conclusions derived from it, again introduce an assumption that *the baseline MC can be used to represent signal*.

With a signal TS distribution, we can characterise the power of our test by assessing the degree to which the signal TS distribution differs from the background one. For a given p-value threshold, as defined by the background model, we can calculate how frequently a given signal hypothesis would lead to a rejection of the null hypothesis. This yields the Type II error rate for any test.

The principle can be extended to cover multiple hypotheses. In the case of neutrino astronomy, a signal hypothesis can be defined for any number of signal neutrinos,  $n_{\text{inj}}$ , that are injected. Since the detection of neutrinos is a random process, the number of signal neutrinos can be simulated with a poisson process of mean  $n_{\text{exp}}$ . We can thus parameterise a continuous set of signal hypotheses as a function of  $n_{\text{exp}}$ , under the assumption of a given spectral model.

An example signal TS distribution can be seen in Figure 1.10, which covers the same time-integrated horizon source shown in Figure 1.8 with the addition of  $\approx 3$  injected signal neutrinos. The signal TS distribution is notably shifted to higher TS values, with only 6% of trials yielding a TS=0. The same trend is seen for Figure 1.11, with the same number of injected signal neutrinos using a spatial-only likelihood.

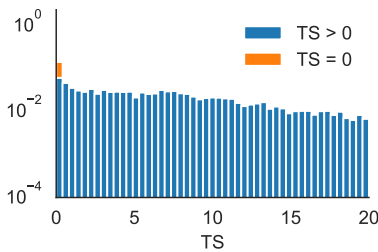


Figure 1.10: Signal TS distribution for the standard Point Source Likelihood (Equation 1.17), with  $\approx 3$  injected neutrinos.

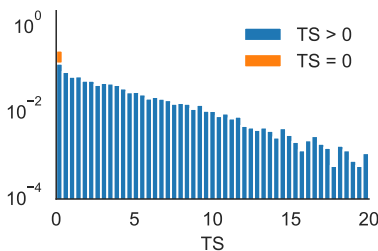


Figure 1.11: Signal TS distribution for the Point Source Likelihood without an energy term, with  $\approx 3$  injected neutrinos.

It is often useful to quantify the rate of both Type I and Type II errors associated with different regions of parameter space, especially those which rely on  $n_{\text{exp}}$ . One example is the *sensitivity* of a test, defined as the value of  $n_{\text{exp}}$  for which 90% of the signal trials will yield a TS value greater than the background median. Here the Type I error rate is 50%, and the Type II error rate is 10%.

Another common metric is the *median 5 $\sigma$  discovery potential*. This is the value of  $n_{\text{exp}}$  for which 50% of the signal trials will yield a p-value exceeding the 5 $\sigma$  threshold. In this case, the Type I error rate is  $\approx 3 \times 10^{-7}$ , while the Type II error rate is 50%. The 5 $\sigma$  discovery potential illustrates the region of signal parameter space for which a discovery could be expected.

An example of the sensitivity is shown in Figure 1.12, using the background median threshold (TS=0.0) from the distribution in Figure 1.8. For comparison, the spatial-only sensitivity is shown in Figure 1.13, relative to the corresponding background median distribution (TS=0.0) in Figure 1.9. While the standard Point Source Likelihood (Equation 1.17) has a sensitivity of  $\approx 3$  signal neutrinos, the spatial-only likelihood has a sensitivity of  $\approx 4$  signal neutrinos. The latter method thus requires  $\approx 33\%$  more signal to produce a ‘likely detection’, illustrating the enhanced power of the energy-dependent Point Source Likelihood as a statistical test. The discrepancy is even more extreme for discovery potential, with the standard method requiring  $\approx 10$  neutrinos (Figure 1.14) whereas the spatial-only method requires  $\approx 18$  neutrinos (using the extrapolation in Figure 1.15).

These metrics allow us quantify the performance of a test without requiring knowledge of the actual outcome of the test on real data. In this way, an analysis can be designed that is *blind*, and thus free from human bias. We optimise our analysis in terms of achieving the best possible sensitivity or discovery potential, and only then do we perform the test on real data. Applying this principle to the two cases outlined above, it clear that we should use the Point Source Likelihood with an energy term, and this conclusion has been reached without knowledge of the ultimate outcome of either test on the real dataset.

Once the analysis has been *unblinded*, we can also recycle these pseudo-experiments to set an upper limit. Following exactly the same procedure as for sensitivity, we can derive an upper limit at some confidence level, typically 90%, using the observed TS value and our pseudo-experiments with added signal. Our upper limit is defined as the signal expectation for which 90% of the pseudo-experiments would yield a TS greater than or equal to the value observed. By construction, for a median experimental result of the background hypothesis, the upper limit derived at 90% confidence level is exactly equal to the sensitivity. Conventionally, in IceCube, for results which yield an underfluctuation relative to background expectations (a TS value less than the median), the sensitivity is quoted as an upper limit.

Both sensitivity and discovery potential can be used to characterise and compare the relative power of statistics tests, in terms of signal events. However, through use of the effective area,  $A_{\text{eff}}(\delta)$ , we can convert these values of  $n_{\text{exp}}$  into corresponding values of muon neutrino flux normalisation.

Under the assumption that *the effective area, as derived with baseline MC, is an accurate description of the detector*, we then find for a flux of normalisation  $\phi_0$ :

$$n_{\text{exp}}(\gamma) = \phi_0 \int \mathcal{S}_{\text{time}}(t) dt \int A_{\text{eff}}(\delta, E_\nu) \times E_\nu^{-\gamma} dE_\nu \quad (1.19)$$

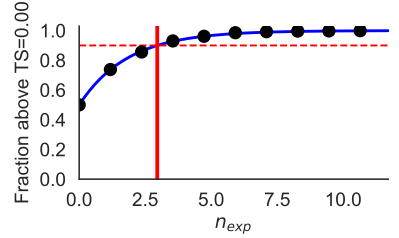


Figure 1.12: Sensitivity for the standard Point Source Likelihood (Equation 1.17), using the background TS distribution from Figure 1.8.

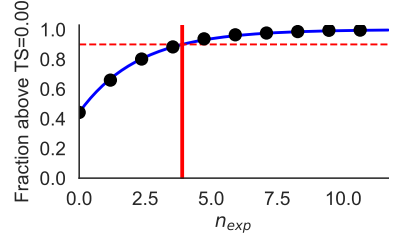


Figure 1.13: Sensitivity for the Point Source Likelihood without an energy term, using the background TS distribution from Figure 1.9.

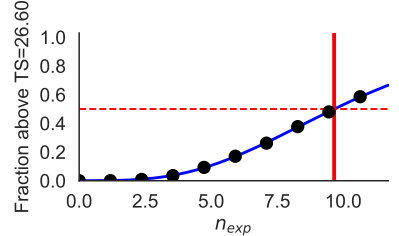


Figure 1.14: 5 $\sigma$  Discovery Potential for the standard Point Source Likelihood (Equation 1.17), using background TS distribution from Figure 1.8.

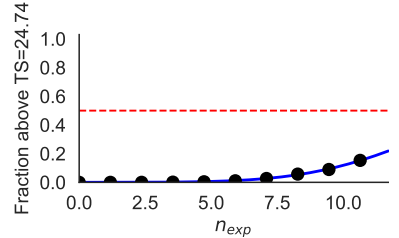
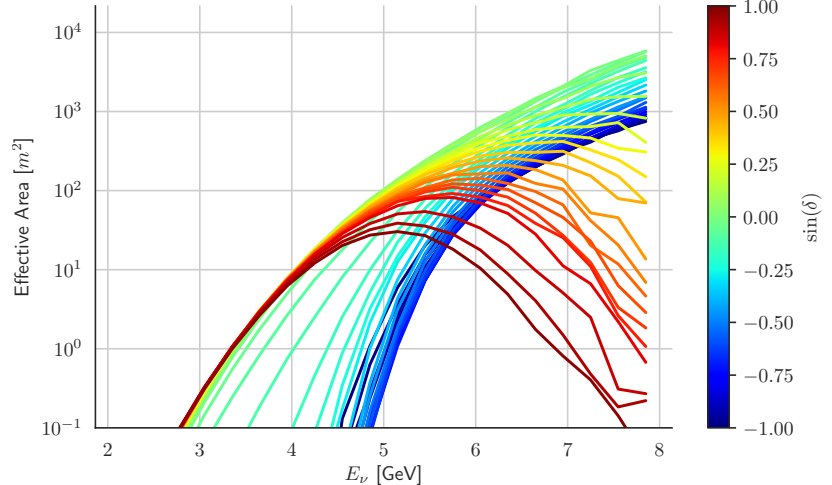


Figure 1.15: 5 $\sigma$  Discovery Potential for the Point Source Likelihood without an energy term, using background TS distribution from Figure 1.9.

The effective area as a function of declination,  $A_{\text{eff}}(\delta)$ , is shown in Figure 1.16. The effective area is highest at the horizon (green lines), where it increases with neutrino energy. However, for more northern declination (yellow to red lines), the increasing impact of earth absorption suppresses neutrino detection at energies greater than 100 TeV. For the southern hemisphere, increasingly aggressive cuts to reject atmospheric muons mean that the effective area is also lower overall (blue lines), though as with the horizon there is no earth absorption of neutrinos.



**Figure 1.16:** Effective area as a function of neutrino energy and declination.

With Equation 1.19, we can then characterise the properties of astrophysical neutrino sources for which we could expect a discovery, and conversely we can constrain these properties for a null result. This is illustrated in Figure 1.17, illustrating the sensitivity and  $5\sigma$  discovery potential for a point source at various declinations. The values are derived using the full Point Source Likelihood introduced in Equation 1.17, including an energy term. As expected from Figure 1.16, the detector is most sensitive at the horizon but gradually deteriorates at more northern declinations due to increasing Earth absorption. Below the horizon, the sensitivity rapidly deteriorates due to the higher muon background.

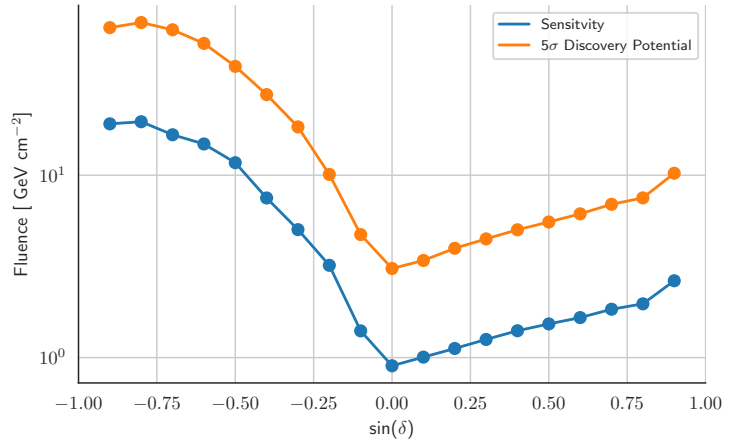


**Figure 1.17:** Sensitivity and Discovery potential as a function of declination for an  $E^{-2}$  spectrum.

## 1.7 Stacking Multiple Sources

The simple source hypothesis outlined in Equation 1.8 describes a single source, but can easily be expanded to include an ensemble of sources, known as a *Stacking Analysis*. For a multi-source hypothesis, the relative contribution of each source must be accounted for.

In most cases, it is *assumed that all sources share the same intrinsic neutrino spectrum*. A further assumption must be made on the fraction of catalogue flux,  $f_k$ , that each kth source will contribute. One common assumption is *equal weights*, so that each of M sources contributes equally:

$$f_k = \frac{1}{M} \quad (1.20)$$

Alternatively, another common assumption is *standard candles*, where the intrinsic luminosity of each source is equal. For each kth source at luminosity distance  $D_{L,k}$

$$f_k = \frac{1/D_{L,k}^2}{\sum_{k=1}^M (1/D_{L,k}^2)} \quad (1.21)$$

In any case, we can then calculate the expected number of signal neutrinos,  $n_k$ , for each source:

$$\phi_k = \phi_0 \times f_k \quad (1.22)$$

$$n_k(\gamma) = \phi_0 f_k \int \mathcal{S}_{\text{time}, k}(t) dt \int A_{eff}(\delta_k, E_\nu) \times E_\nu^{-\gamma} dE_\nu \quad (1.23)$$

Using Equation 1.23, we can then define the fractional source weight,  $w_k$ , of each kth source:

$$w_k(\gamma) = \frac{n_k(\gamma)}{\sum_{k=1}^M n_k(\gamma)} = \frac{f_k \int \mathcal{S}_{\text{time}, k}(t) dt \int A_{eff}(\delta_k, E_\nu) \times E_\nu^{-\gamma} dE_\nu}{\sum_{k=1}^M (f_k \int \mathcal{S}_{\text{time}, k}(t) dt \int A_{eff}(\delta_k, E_\nu) \times E_\nu^{-\gamma} dE_\nu)} \quad (1.24)$$

Unlike for Equation 1.23,  $w_k$  does not ultimately depend on the flux normalisation  $\phi_0$ . For fixed spectral index, the relative contribution of different sources is independent of the number of neutrinos. Using these source weights, we can then define our normalised Signal model:

$$\mathcal{S}(\gamma) = \sum_{k=1}^M (w_k(\gamma) \times \mathcal{S}_k(\gamma)) \quad (1.25)$$

Substituting this into Equation 1.17, we arrive at our stacked PS likelihood. Conveniently,  $\mathcal{S}_E(\gamma)$  does not vary by source, so can be factorised out of the sum. For steady neutrino sources,  $\mathcal{S}_{\text{time}}$  can also be factorised out, leaving only a sum over  $\mathcal{S}_{\text{space}, k}$ .

## 1.8 Combining seasons

We can generalise the procedure even further, to account for multiple IceCube seasons. As outlined in Chapter ??, the IceCube detector was constructed in phases, with multiple partial detector configurations each operating for roughly one year. It is conventional, as for *ps tracks v003*, to include data from IC40, IC59, IC79, and IC86, where ICn refers to the number of detector strings, n, in operation. The first year of IC86, (IC86-2011), corresponded to a different set of detector triggers, and is treated distinctly from IC86 for seasons 2012 and upward. Thus there are ultimately five distinct sets of detector operation in the ten-year point source dataset, each with a unique event selection.

These J seasons can be combined by treating them as independent datasets, and combining the likelihood for each ith neutrino in each jth season:

$$\mathcal{L} = \prod_j^J \prod_i^N \mathcal{L}_{i,j} \quad (1.26)$$

The procedure outlined in Sections 1.2 and 1.3 is followed for each dataset, yielding season-specific PDFs. The signal hypothesis can be divided in much the same way as for stacking, with a separate time PDF covering the uptime for each season ( $t_{0,j} - t_{1,j}$ ). Then, for each kth source and jth season:

$$n_{j,k}(\gamma) = \phi_0 \int_{t_{0,j}}^{t_{1,j}} \mathcal{S}_{\text{time, j, k}}(t) dt \int A_{eff,j}(\delta_k, E_\nu) \times E_\nu^{-\gamma} dE_\nu \quad (1.27)$$

$$\mathcal{S}_j(\gamma) = \sum_{k=1}^M (w_{k,j}(\gamma) \times \mathcal{S}_{j,k}(\gamma)) \quad (1.28)$$

$$n_j(\gamma) = n_s \sum_{k=1}^M w_{k,j}(\gamma) \quad (1.29)$$

$$\mathcal{L}(n_s, \gamma) = \prod_j^J \prod_i^N \left( \frac{n_j}{N} \mathcal{S}_j(\theta_i, \gamma) + \frac{N - n_j}{N} \mathcal{B}_j(\theta_i) \right) \quad (1.30)$$

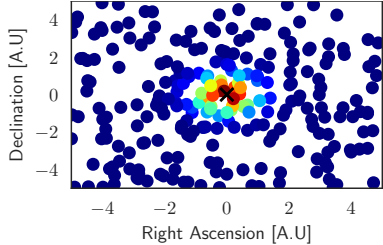


Figure 1.18: Visualisation of a spatial PDF.

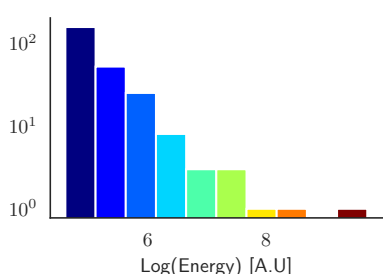


Figure 1.19: Visualisation of an energy proxy PDF.

## 1.9 Cluster-search algorithm

One possible modification to the likelihood outlined above is to search for neutrino emission that is clustered in time, within a larger search window. The procedure is implemented in `flarestack`, and is used in this thesis for analysis of some sources.

Multiple box time PDFs are tested for a given source, and the one with the highest TS value is selected. Flares have both a start point,  $T_0$ , and end point,  $T_1$ , yielding two additional fit parameters. However, the likelihood landscape has discontinuities from when single neutrinos passing in/out boundary of the time PDF. Therefore, to avoid issues with minimisation

by gradient descent, in *flarestack* the optimal flare is selected through a brute-force minimisation procedure. Though  $T_0$  and  $T_1$  are in principle continuous variables, the most significant possible cluster will always be one that begins and ends with the detection of a neutrino.

However, for  $N$  neutrinos in a dataset, there are  $N \times (N - 1)/2$  possible pairs to test. To further speed computation, a simplifying assumption is made that *the most significant cluster will begin and end with signal-like neutrinos*. The  $\mathcal{S}/\mathcal{B}$  ratio is calculated for all neutrinos, and only those with  $\mathcal{S} > \mathcal{B}$  are considered sufficiently signal-like to test. This procedure is illustrated in Figure 1.20.

However, there is an inherent bias in such a cluster search, because there are many possible small clusters in a search window but very few possible large ones. Background fluctuations are preferentially found as small clusters. To counter this effect, a marginalisation term must be introduced to balance this bias, yielding a *flare likelihood*. For a search window between  $t_0$  and  $t_1$ , with a flare from  $T_0$  to  $T_1$ , we find:

$$\Delta_{T, \text{flare}} = \int_{T_0}^{T_1} f_{\text{uptime}}(t) dt \quad (1.31)$$

$$\Delta_{T, \text{search}} = \int_{t_0}^{t_1} f_{\text{uptime}}(t) dt \quad (1.32)$$

$$\mathcal{L}(n_s, \gamma, T_0, T_1) = \prod_i^N \left( \frac{n_s}{N} \mathcal{S}(\theta_i, \gamma, T_0, T_1) + \frac{N - n_s}{N} \mathcal{B}(\theta_i) \right) \times \frac{\Delta_{T, \text{flare}}}{\Delta_{T, \text{search}}} \quad (1.33)$$

An example of this cluster search, as used for the source AT2018cow (see Chapter 3), demonstrates the impact on discovery potential. Given the additional degrees of freedom, there is more scope for background fluctuations, so the threshold for discovery is higher in the case that neutrino emission extends over the full search window. However, for shorter neutrino emission periods, the discovery potential is much reduced.

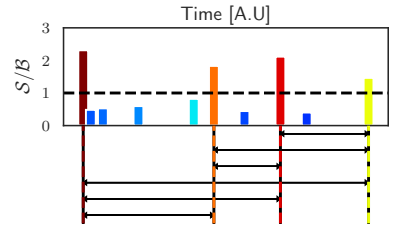


Figure 1.20: Visualisation of the cluster search algorithm.

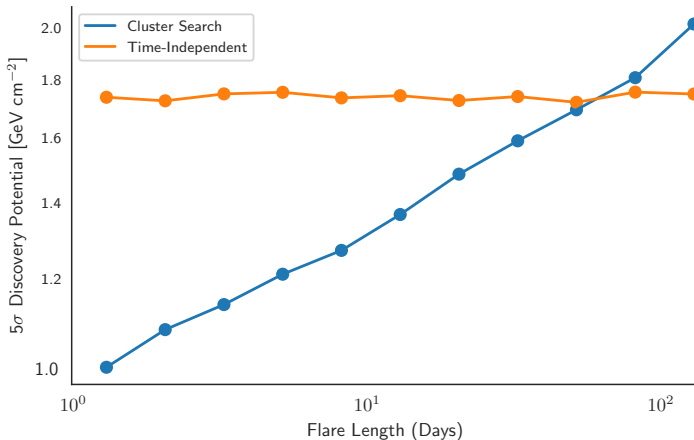


Figure 1.21: Estimated  $5\sigma$  Discovery Potential for AT2018cow as a function of flare length, given in units of total fluence for an  $E^{-2}$  spectrum over the 130 day search window.

## 1.10 Fitting the relative source weights

The direct implementation of a well-defined  $\mathcal{S}$  for a stacking analysis is the most powerful possible test, *under the assumption that the relative distribution of the signal is known*. This condition can be satisfied when a specific model is tested that accurately predicts the relative number of signal events produced by each source in an ensemble. A prediction using multi-wavelength emission as a proxy, or expectations for a population of neutrino standard candles, are common assumptions. However, in an agnostic search for neutrino emission from a source ensemble, the uncertainty of our knowledge should be ideally implemented through priors on our expectations of neutrino emission from each source. The standard *Point Source Likelihood* can be thought of as one extreme with maximum knowledge yielding  $\delta$ -function priors for the neutrino emission from each source. The other extreme is one of maximum ignorance, in which flat priors  $n_{s,k}$  for each kth source is allowed to vary completely independently. In that case, we can replace the point-source likelihood (Equation 1.17) with the *multi-source likelihood*:

$$\mathcal{L}(\vec{n}_s, \gamma) = \prod_j^N \left( \sum_k \left[ \frac{n_{s,k}}{N} \mathcal{S}_k(\theta_j, \gamma) \right] + \frac{N - \sum_k [n_{s,k}]}{N} \mathcal{B}(\theta_j) \right) \quad (1.34)$$

This approach is commonly referred to as *fitting the weights* of each source, in contrast to the standard method of *fixed source weights*. Additional flexibility comes at the expense of more independent fit parameters, and thus a higher TS threshold to achieve fixed significance. In the limit of many sources, each with sub-unity neutrino expectations, the number of degrees of freedom would exceed the number of expected signal events. It is most useful for analysing a small number of sources, in which the relative neutrino distribution is not known, but for which multiple neutrinos would be expected. This likelihood is used for some results in this thesis (see Chapter 3).

## 1.11 Flarestack in practice

The evaluation of this likelihood is time-consuming, and the implementation of this process in *flarestack* makes several standard simplifications to speed calculations [114].

[114]: Stasik (2017), “Search for High Energetic Neutrinos from Core Collapse Supernovae using the IceCube Neutrino Telescope”

The first is the recognition that the parameters which maximise the likelihood will also maximise the likelihood ratio, and thus the test statistic. Rather than evaluating two independent likelihoods, we can instead directly evaluate the test statistic:

$$TS = 2 \log \left( \frac{\mathcal{L}(\hat{n}_s, \hat{\gamma})}{\mathcal{L}(n_s = 0)} \right) \quad (1.35)$$

$$TS = 2 \log \frac{\prod_j^N \left( \frac{n_s}{N} \mathcal{S}(\theta_j, \gamma) + \frac{N-n_s}{N} \mathcal{B}(\theta_j) \right)}{\prod_j^N \mathcal{B}(\theta_j)} \quad (1.36)$$

By dividing this through, we find:

$$TS = 2 \log \left( \prod_j^N \left( \frac{n_s}{N} \left[ \frac{\mathcal{S}(\theta_j, \gamma)}{\mathcal{B}(\theta_j)} \right] + 1 - \frac{n_s}{N} \right) \right) \quad (1.37)$$

$$TS = 2 \sum_j^N \log \left( \frac{n_s}{N} \left[ \frac{\mathcal{S}(\theta_j, \gamma)}{\mathcal{B}(\theta_j)} - 1 \right] + 1 \right) \quad (1.38)$$

Equation 1.38 is faster to evaluate, because it bypasses the need to calculate both signal and background energy proxy PDFs explicitly. Instead, we can pre-computing the ratio  $\frac{\mathcal{S}}{\mathcal{B}}$  for a variety of spectral indices, saving a per-event division calculation.

An additional simplifying assumption is that neutrinos are typically localised to a resolution of  $\sim 1$  degree, so events which lie many degrees from a source have a negligible probability of being signal. For events lying outside a  $\pm 5$  degree box, and those within a  $\pm 5$  degree box but with a spatial likelihood ratio less than  $10^{-21}$ , we make the approximation that  $\mathcal{S} \approx 0$  so then  $TS \approx 0$ . Using the formulation in Equation 1.38, we see we can simply neglect to evaluate the likelihood for these events, without altering the final sum. This box cut thus removes the overwhelming majority of events from the likelihood evaluation step, yielding vast speed improvements while having a negligible impact on the fitting process.





## 2 Neutrino Cosmology

“ The universe is very big - there’s about 100,000 million galaxies in the universe, so that means an awful lot of stars. ”

---

Jocelyn Bell Burnell, *Beautiful Minds*, 2010

Often, the strictest limits on the neutrino emission of a population comes not from direct likelihood analysis, but rather from much simpler cosmological arguments. IceCube measures a diffuse astrophysical neutrino flux, setting a limit on the cumulative contribution that can come from a given population. This information can be illustrated by a *Kowalski Plot*, encompassing the product of a local rate and a mean neutrino luminosity per source (see Chapter ??).

As part of this thesis, a software framework was developed to analytically calculate neutrino emission from cosmological populations. This is integrated into the `Flarestack` python package, written by the author [106].

2.1 Cosmological Source Rates	25
2.2 Differential flux and K-corrections	27
2.3 Comparing Source Classes	30

[106]: Stein et al. (2020), *icecube/flarestack*

### 2.1 Cosmological Source Rates

Populations of astrophysical objects are characterised by their *local rate* (how often they occur in the local universe), and their source evolution (how does their rate change as a function of redshift). Rates are typically estimated from unbiased surveys, such as the ZTF Bright Transient Survey [115]. Since many astrophysical transients outlined in Chapter ?? are ultimately related to stages of stellar evolution, they tend to be strongly correlated to the *Star Formation Rate* (SFR), the rate at which stars are formed at a given redshift.

[115]: Perley et al. (2020), “The Zwicky Transient Facility Bright Transient Survey. II. A Public Statistical Sample for Exploring Supernova Demographics”

[116]: Madau et al. (2014), “Cosmic Star-Formation History”

[117]: Strolger et al. (2015), “The Rate of Core Collapse Supernovae to Redshift 2.5 from the CANDELS and CLASH Supernova Surveys”

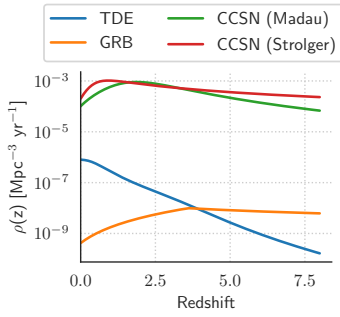


Figure 2.1: Various transient rate densities as a function of redshift.

[118]: Sun et al. (2015), “Extragalactic High-energy Transients: Event Rate Densities and Luminosity Functions”

The SFR can be directly inferred using multi-wavelength surveys of galaxies [116], exploiting the characteristic spectral ratios to quantify stellar contributions in each galaxy. Alternatively, the SFR rate can be indirectly derived using observed rates of core-collapse supernovae identified in surveys [117]. The Core-Collapse Supernova (CCSN) Rate is then directly proportional to the SFR, related by a constant of proportionality  $k_{cc}$ . These two CCSN rate estimates are illustrated in Figure 2.1, and broadly agree. The SFR peaks at  $z \approx 1-2$ , and declines thereafter. It initially has a *positive evolution*, i.e it increases with increasing redshift.

An alternative driver of evolution is the rate of supermassive black holes (SMBHs), which are connected with many other sources such as blazars, radio galaxies and TDEs. In contrast to the SFR, massive SMBHs are thought to be formed through mergers of smaller SMBHs. The rate of massive SMBHs has a tendency to increase over time, so is larger in the local universe than at higher redshifts. In contrast to the SFR, the SMBH rate thus has a *negative source evolution*. Of particular relevance to this thesis is the rate of TDEs, which have been proposed theoretically to follow this negative SMBH rate, as illustrated in Figure 2.1 [118]. Caution must be taken for this rate, since TDEs are primarily detected in the local universe, so the high-z rates are broadly unconstrained observationally.

With any chosen source rate and neutrino spectrum, we can calculate the corresponding *cumulative neutrino flux* arising from that population [20]. For steady sources, we simply find:

$$\overline{\rho(z)} \equiv \frac{dN(z)}{dV_C} \quad (2.1)$$

$$\overline{R(z)} \equiv \frac{dN(z)}{dz} = \overline{\rho(z)} \times \frac{dV_C}{dz} \quad (2.2)$$

If we instead consider transient objects, cosmological effects start to become important. In the following, we denote quantities in the source frame with  $x'$ , while those at Earth are given as  $x$ . It is clear that the number of particles itself must be invariant to the frame, i.e  $N' = N$ . However, there is in general a process of *cosmic time dilation*, where the passage of time at the source location,  $t'$ , is slowed when observed at Earth,  $t$ :

$$t = (1 + z)t' \quad (2.3)$$

$$\frac{dt'}{dt} = \frac{1}{1 + z} \quad (2.4)$$

For a transient rate density  $\rho(z)$  as a function of redshift, we can then calculate the rate of transients per redshift shell. The rate is given per unit time, but the impact of time dilation at higher redshifts suppresses the rate by a factor  $(1+z)$ .

$$\rho(z) \equiv \frac{dN(z)}{dV_C dt'} \quad (2.5)$$

$$R(z) \equiv \frac{dN(z)}{dt dz} = \rho(z) \times \frac{dV_C}{dz} \times \frac{1}{1+z} \quad (2.6)$$

These are illustrated in Figure 2.2. The differential comoving volume of a redshift shell is derived using the *astropy* package [119]. We can then calculate the transient rate in the universe:

$$R_{all} = \int_0^\infty R(z) dz \quad (2.7)$$

[119]: Astropy Collaboration et al. (2013), “Astropy: A community Python package for astronomy”

## 2.2 Differential flux and K-corrections

Having calculated the rate of sources, we must next calculate the neutrino flux produced by each individual object. We first consider the isotropic emission of a fixed number of particles,  $N$ , by a source. In that case, the particle count per unit area on Earth will ultimately depend only on the comoving distance to that object,  $D_c$ :

$$\frac{dN}{dA} = \frac{N}{4\pi D_c^2} \quad (2.8)$$

If we instead wish to consider the particle flux, we must differentiate this quantity with respect to time:

$$\frac{dN}{dAdt} = \frac{dN}{dt} \times \frac{1}{4\pi D_c^2} \quad (2.9)$$

Often, we only know the emission rate of particles in the source frame,  $\frac{dN}{dt'}$ , in which case we replace Equation 2.9 with:

$$\frac{dN}{dAdt} = \frac{1}{1+z} \times \frac{1}{4\pi D_c^2} \times \frac{dN}{dt'} \quad (2.10)$$

It may be more relevant to consider the luminosity of a source, where the intrinsic source luminosity is defined as:

$$L' \equiv \frac{d}{dt'} \left( \int E' dN \right) = \frac{d}{dt'} \left( \int E' \frac{dN}{dE'} dE' \right) \quad (2.11)$$

However, a second cosmological effect must here be accounted for. The expansion of the universe leads to a process of *redshifting*, so that  $E'$ , the energy of emitted particles, is not the same as  $E$ , the energy at which the particle observed:

$$E = \frac{E'}{1+z} \quad (2.12)$$

$$\frac{dE}{dE'} = \frac{1}{1+z} \quad (2.13)$$

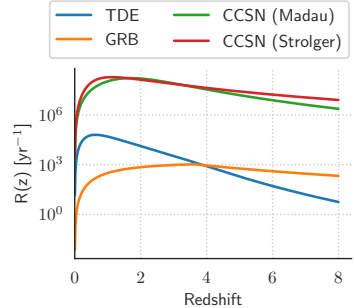


Figure 2.2: Various transient rates as a function of redshift.

We will thus observe a redshifted energy flux as a consequence of the redshifting of each individual particle energy E:

$$S \equiv \frac{d}{dtdA} \left( \int EdN \right) = \frac{1}{1+z} \times \frac{1}{4\pi D_C^2} \times \frac{d}{dt'} \left( \int EdN \right) \quad (2.14)$$

$$S = \frac{1}{1+z} \times \frac{1}{4\pi D_C^2} \times \frac{d}{dt'} \left( \int E \frac{dN}{dE'} dE' \right) \quad (2.15)$$

$$S = \frac{1}{(1+z)^2} \times \frac{1}{4\pi D_C^2} \times \frac{d}{dt'} \left( \int E' \frac{dN}{dE'} dE' \right) = \frac{1}{(1+z)^2} \times \frac{L'}{4\pi D_C^2} \quad (2.16)$$

Given the importance of luminosity and energy flux in astronomy, it is conventional to define a new distance measure known as *luminosity distance*,  $D_L$ :

$$D_L \equiv \sqrt{\frac{L'}{4\pi S}} = D_C(1+z) \quad (2.17)$$

In this case, Equation 2.16 is reduced to:

$$S = \frac{L'}{4\pi D_L^2} \quad (2.18)$$

However, telescopes/detectors are only sensitive in specific energy ranges, so it is typically more important to know the flux at a given energy. This quantity, known as the *differential energy flux*, is defined as:

$$S_E \equiv \frac{dS(E)}{dE} = (1+z) \times \frac{dS}{dE'} \quad (2.19)$$

$$S_E = (1+z) \times \frac{1}{4\pi D_L^2} \times \frac{dL'}{dE'} \quad (2.20)$$

For convenience, we define the *differential luminosity* (or *specific luminosity*):

$$L'_{E'} \equiv \frac{dL'}{dE'} = \frac{d}{dt'} \left( E' \frac{dN'(E')}{dE'} \right) \quad (2.21)$$

We can then compactly write:

$$S_E = (1+z) \times \frac{L'_{E'}}{4\pi D_L^2} \quad (2.22)$$

The above Equation 2.22 is the definition of a *k-correction*, a widely-used formula by which the intrinsic source properties of an object can be converted to the expected differential energy flux. This is a generic definition, and is valid for both photon and neutrino astronomy.

However, for particle detectors such as IceCube, it is instead more common to consider the differential particle flux, given by differentiating

Equation 2.10. To conserve particle number despite the impact of red-shifting, the observed count rate per unit energy at  $E$ , must be equal to the emission rate of particles at energy  $E'$ :

$$dN(E) = dN'(E') \quad (2.23)$$

$$\frac{dN(E)}{dE} = \frac{dN'(E')}{dE'} \times \frac{dE'}{dE} = (1+z) \times \frac{dN'(E')}{dE'} \quad (2.24)$$

Then we see:

$$\frac{dN}{dAdEdt} = \frac{1}{1+z} \times \frac{1}{4\pi D_C^2} \times \frac{dN(E)}{dEdt'} \quad (2.25)$$

$$\frac{dN}{dAdEdt} = \frac{1}{4\pi D_C^2} \times \frac{dN'(E')}{dE'dt'} \quad (2.26)$$

For this thesis, it is only relevant to consider the special case where source spectra are power laws with some spectral index,  $\gamma$ :

$$\frac{dN'(E', t')}{dE'dt'} = \phi_0(t') \times \left(\frac{E'}{E_0}\right)^{-\gamma} \quad (2.27)$$

$$L'_{E'}(t') \equiv E' \times \frac{dN'(E', t')}{dE'dt'} = E' \times \phi(t') \times \left(\frac{E'}{E_0}\right)^{-\gamma} \quad (2.28)$$

By substituting in Equation 2.12, we finally reach:

$$\frac{dN(E', t')}{dAdEdt} = (1+z)^2 \times \frac{1}{4\pi D_L^2} \times \phi(t') \times \left(\frac{E'}{E_0}\right)^{-\gamma} \quad (2.29)$$

$$\frac{dN(E, t')}{dAdEdt} = (1+z)^{2-\gamma} \times \frac{1}{4\pi D_L^2} \times \phi(t') \times \left(\frac{E}{E_0}\right)^{-\gamma} \quad (2.30)$$

Equation 2.30 is convenient for steady sources of known luminosity, where  $\phi(t') = \phi_0$ . For transients, it can be more helpful to consider the cumulative time-integrated particle flux per transient. We typically assume a constant flux for a fixed duration  $\Delta_T$ :

$$\phi(t') = \begin{cases} \phi_0 & T'_0 < t' < T'_1 \\ 0 & \text{otherwise} \end{cases} \quad (2.31)$$

$$\int_0^\infty \phi(t') dt' = \phi_0 \Delta_T \quad (2.32)$$

We then find:

$$\frac{dN(E)}{dAdE} = (1+z)^{2-\gamma} \times \frac{1}{4\pi D_L^2} \times \left(\frac{E}{E_0}\right)^{-\gamma} \times \int \phi(t') dt \quad (2.33)$$

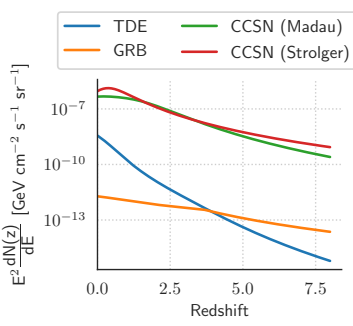


Figure 2.3: Contributed flux at Earth as a function of redshift.

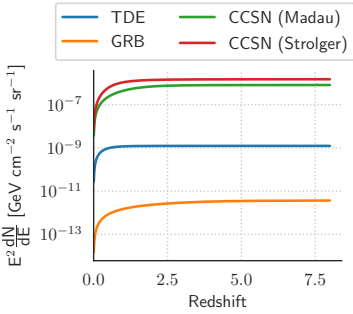


Figure 2.4: Cumulative flux at Earth as a function of redshift.

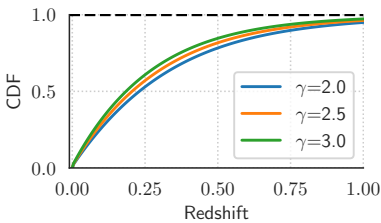


Figure 2.5: CDF as a function of spectral index for TDEs.

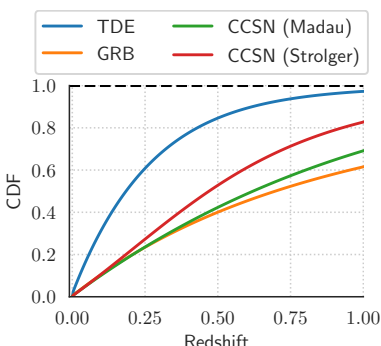


Figure 2.6: CDF as a function of source evolution.

$$\frac{dN(E)}{dAdE} = (1+z)^{3-\gamma} \times \frac{\phi_0 \Delta_{T'}}{4\pi D_L^2} \times \left(\frac{E}{E_0}\right)^{-\gamma} \quad (2.34)$$

Figure 2.3 shows the contributed diffuse flux at Earth as a function of redshift, assuming each transient contributes  $10^{50}$  erg in a power law from 1 GeV to 10 PeV. Ultimately, the diffuse flux measured by IceCube will be the integral of this flux-per-source multiplied by the source rate in Equation 2.6:

$$\frac{dN(E)}{dEdAdt} = \int_0^\infty \left[ (1+z)^{2-\gamma} \times \frac{\rho(z)\phi_0 \Delta_{T'}}{4\pi D_L^2} \times \left(\frac{E}{E_0}\right)^{-\gamma} \right] \frac{dV_C}{dz} dz \quad (2.35)$$

These cumulative neutrino fluxes are shown in Figure 2.4. For steady sources, using Equations 2.2 and 2.30, we similarly find:

$$\frac{dN(E)}{dEdAdt} = \int_0^\infty \left[ (1+z)^{2-\gamma} \times \frac{\overline{\rho(z)}\phi_0}{4\pi D_L^2} \times \left(\frac{E}{E_0}\right)^{-\gamma} \right] \frac{dV_C}{dz} dz \quad (2.36)$$

## 2.3 Comparing Source Classes

Equation 4.12 reveals differences in the characteristic behaviour of different possible neutrino source populations. The impact of differing the spectral index is illustrated in Figure 2.5, using the TDE rate. Given that high-z transients are already suppressed, the overall impact is relatively minor. However, as is clear in both Figure 2.3 and 2.6, the source evolution heavily impacts the relative contribution of nearby sources to the diffuse flux. A survey complete up to  $z=0.25$  would already account for 60% of all TDE neutrino emission, whereas it would contain just 20–25% of CCSN neutrino emission. Each curve in Figure 2.6 gives the per-neutrino probability of detecting a counterpart as a function of maximum redshift.

Figure 2.7 illustrates the completeness correction factor as a function of redshift. For a sample complete up to a redshift of  $z$ , multiplying the sample flux by the correction factor will yield the total population flux. Equivalently, this factor is the number of population neutrinos that would need to be followed up before one counterpart was identified, assuming that the follow-up instruments were sensitive up to redshift  $z$ . This Figure illustrates most starkly the challenge of optical follow-up of neutrinos, and the relative sensitivity to different source evolutions. For a TDE-like negative rate, the cumulative neutrino flux will be overwhelmingly dominated by nearby sources, while transients that evolve with the Star Formation Rate (e.g. CCSNe) have a much larger contribution from more distant sources.

To give a specific example revisited in Chapter 4, ZTF is approximately complete in identifying TDEs up to a redshift of 0.15. Per Figure 2.6, this volume will contain sources responsible for roughly 40% of the population flux, so from Figure 2.7, we see that we would expect to find roughly 2/5 of counterparts to TDE neutrinos. In contrast, CCSNe tend to be dimmer, and with completeness rapidly deteriorating above a redshift of  $z \sim 0.05$  [115]. Even neglecting this effect, with SFR-evolution only 12% of

**Table 2.1:** Summary of assumptions on source classes.

Source	Max redshift [z]	Length [yr]	Search Area [sq. deg.]	Detection Efficiency [%]	Local Rate [Mpc <sup>-3</sup> yr <sup>-1</sup> ]	Evolution
TDE (Non-jetted)	0.15	1.00	3.14	100.00	8e-07	
TDE (Jetted)	0.50	0.50	3.14	100.00	3e-11	
SN IIP	0.05	0.30	3.14	100.00	5.3e-05	
SN Ic	0.05	0.03	3.14	100.00	1.8e-05	
SN IIn	0.08	0.30	3.14	100.00	6.5e-06	
FBOT	0.25	0.30	3.14	100.00	7e-07	
GRB	1.00	0.00	314.16	100.00	4.2e-10	
FRB (complete)	1.00	0.00	3.14	100.00	0.072	
FRB (0.1%)	1.00	0.00	3.14	0.10	0.072	

neutrinos will be produced in the volume  $z < 0.15$ .

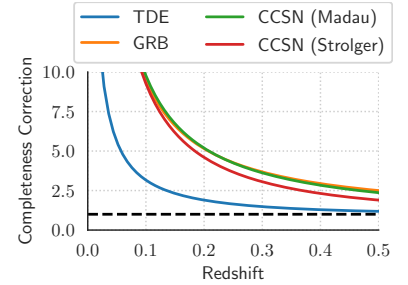
To approximately quantify the impact of this effect, we can consider the general power of tests probing this region. The signal,  $\mathcal{S}$  is proportional to the fraction of flux belonging to resolvable sources, while the background rate,  $\mathcal{B}$ , is proportional to the number of sources within this volume.

We consider a neutrino with typical properties for those issued as Ice-Cube realtime alerts. We assume it has a *signalness* of 50%, i.e that it has a 50% probability to be of astrophysical origin rather than from atmospheric backgrounds. Such alerts are typically reported with a median angular error of  $\sim 1$  degree. Any source class will then have a cumulative expectation of  $0.5 \times f_{\text{tot}}$ , where  $f_{\text{tot}}$  is the fraction of the total diffuse astrophysical neutrino flux contributed by that source class.

We consider a number of source classes, listed in Table 2.1. We calculate their expected background rate by considering their sky rate, given as a product of their local rate, integrated to a typical telescope horizon, and multiplied by a typical telescope detection efficiency. For each source, we also multiply the appropriate search window for neutrino emission, yielding a final background density for any point on the sky. Multiplying this by the neutrino localisation area gives us the ultimate background rate per follow-up. We also consider the expected signal per search, given as the neutrino population expectation multiplied by the fraction of flux which is produced by sources accessible to telescopes. These are illustrated in Figure 2.8 for a variety of source classes.

The intrinsic signal-to-noise of different source classes can be seen, with the white band indicating the transition from the red signal-dominated regions to the blue background-dominated regions. In general, the probability of observing a coincidence increases from lower left to upper right, while the significance of any coincidence increases from lower right to upper left. In all cases, the y axis represents the probability of observing a coincidence. For sources with  $N_{\text{bkg}} \lesssim 0.1$ , where the probability of multiple background events is negligible, the x axis corresponds to the p-value for a coincidence.

Neutrino-specific properties of signalness and localisation will linearly scale all points in the x or y direction respectively, but the relative positions of sources remains unchanged. Those sources near the top/left

**Figure 2.7:** Completeness correction factor as a function of source evolution.

[115]: Perley et al. (2020), “The Zwicky Transient Facility Bright Transient Survey. II. A Public Statistical Sample for Exploring Supernova Demographics”

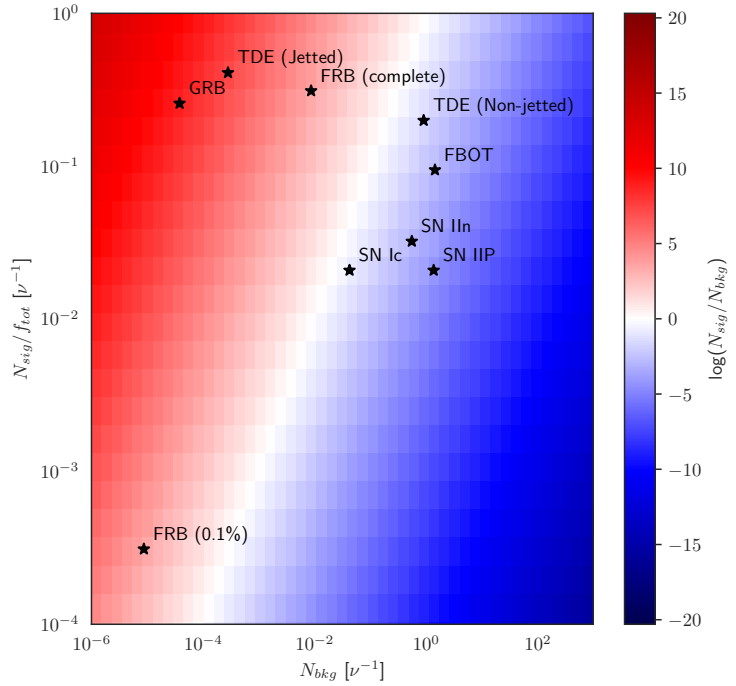


**Figure 2.8:**  $N_{sig}$  vs  $N_{bkg}$

of the Figure are those with the strictest existing limits, often at percent-level, while those nearer the lower/lower-right portion are only weakly constrained or could still produce the entire diffuse flux.

One particularly noteworthy class is FRBs, which are particularly favourable owing to their extremely stringent temporal localisation. Indeed, were telescopes fully efficient at detecting these across the sky, the limits on this class would be perhaps the most stringent of all. However, at the time of the most recent IceCube analysis, 21 FRBs were tested against an estimated rate of  $\sim 3000$  per sky per day, a sample for which no constraint could be placed on the FRB population [120]. It is precisely because the detection efficiency of FRBs is so low that a tiny fraction of signal is detectable. The expected signal to background ratio for FRBs is very high, and this statement is independent of detection efficiency, so any FRB-neutrino coincidence would be very strong evidence for a physical association. However, because the probability that an FRB counterpart would be detected at all is so low at present, no coincidence is likely to be found. This scenario is also illustrated in Figure 2.8, where with a more realistic assumed detection efficiency of 0.1% FRBs are a clear outlier source class.

We can further quantify how the expected significance would change with increasing numbers of follow-up campaigns for different possible source populations. This is shown in Figure 2.9, unsing the same assumptions listed in Table 2.1. Though Figure 2.9 contains no analysis of IceCube data, it is particularly notable that the position of sources correspond very directly to the relative constraints that have been placed on those classes by IceCube. The plot illustrates how well the full unbinned likelihood analysis method used by IceCube for neutrino astronomy can

[120]: Kheirandish et al. (2019), ‘‘Searches for neutrinos from fast radio bursts with IceCube’’

in fact be approximated by a poisson counting experiment. Those source classes on the left (TDEs, GRBs, FRBs with high detection efficiency) are those most favourable for detection with realtime follow-up programs such as the one introduced in Chapters ?? and ???. The starting x position of each curve indicates how many detections would be needed before one counterpart was detected, while the y position quantifies the significance of a signal detection given the background detection rate. As a lower detection efficiency will decrease the signal detection rate, it will be represented in Figure 2.9 as a shift of a curve to the right, as can be seen for the two FRB curves. However, because the background rate is also reduced proportionately, the y axis remains unaffected. In other words, with lower detection efficiency one must do more follow up campaigns to detect N coincidences, but the significance of each Nth coincidence found is independent of detection efficiency.

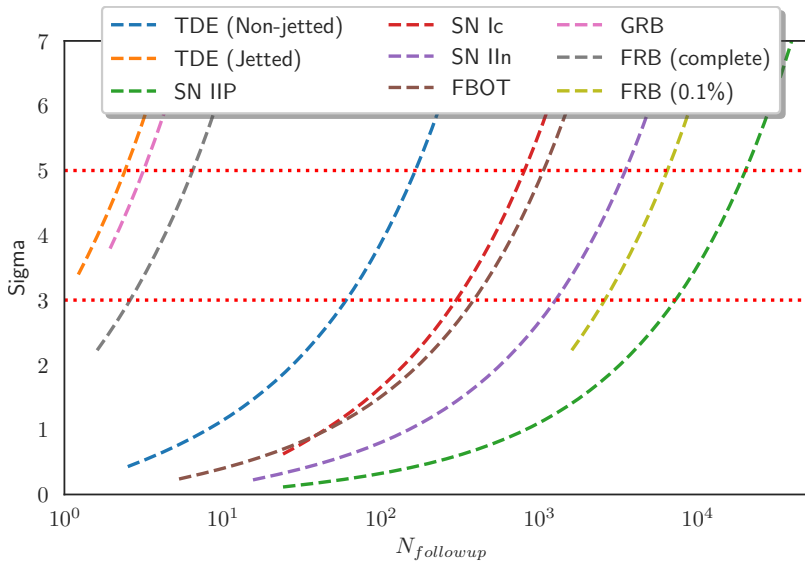


**Figure 2.9:** Statistical significance of excess coincidence as a function of number of follow-up





## 3 Stacking Analyses with IceCube

“ We are all in the gutter, but some of us are looking at the stars ”

Oscar Wilde, *Lady Windermere’s Fan*, 1893

A key component of this thesis is the application of the unbinned likelihood analysis method outlined in Chapter 1 to specific astrophysical objects, to test for correlations indicating neutrino emission. The outcomes of these tests were then analysed in the context of diffuse neutrino flux arising from astrophysical populations, following the framework introduced in Chapter 2. All results are outlined below.

All calculations were performed using the *Flarestack* code, developed by the author. Some results presented were previously published in proceedings written by the author [121].

3.1 Tidal Disruption Events . . . . .	35
3.2 AT2018cow and FBOTs . . . . .	42
3.3 Robustness of Limits . . . . .	44

[121]: Stein (2019), “Search for High-Energy Neutrinos from Populations of Optical Transients”

### 3.1 Tidal Disruption Events

One novel result of this thesis is a stacking analysis of Tidal Disruption Events (TDEs) (see Chapter ??), the first such experimental search for a TDE-neutrino correlation. The details of this analysis are outlined below.

#### Signal Hypothesis

As outlined Chapter ??, theoretical modelling of neutrino emission in TDEs generally distinguishes between those with relativistic jets and

those without. In recognition of this, we ultimately have two distinct hypotheses to test:

1. Neutrino emission from on-axis relativistic jets
2. Neutrino emission from other mechanisms

The timescales predicted for neutrino emission have varied substantially. In general, neutrino emission is expected to occur close to the peak EM brightness of the flare, with durations of a few hours to  $\sim 100$  days. There are no scenarios for neutrino emission preceding disruption.

## Catalogue Compilation

[122]: Auchettl et al. (2017), “New Physical Insights about Tidal Disruption Events from a Comprehensive Observational Inventory at X-Ray Wavelengths”

To perform a correlation analysis, a list of sources must first be compiled. One list of TDEs is maintained by the *OpenTDECatalog* [122], containing relevant metadata and photometry. The database prioritises completeness by containing all objects with a possible TDE classification, even when those classifications are ambiguous [122], and will thus by construction suffer from source contamination. The database itself is maintained by volunteers, and is thus not entirely complete. For the compilation of a catalogue for this thesis, the list from the *OpenTDECatalog* was supplemented by additional objects and data from the literature.

At the time of catalogue compilation in 2018, this database contained approximately 70 objects. Of these, 3 had clear evidence of on-axis relativistic jets, while the remaining 67 did not. We further exclude those objects with peaks  $>100$  days before the start of data-taking during the IC40 data season on 4th May 2008 (see Chapter ??), as these objects did not overlap our neutrino dataset. We are left with 53 TDEs for correlation.

From the starting point of all TDEs, one distinct subsample was created:

- **Jetted TDEs** are X-Ray-bright TDEs which launched relativistic jets pointing towards the Earth. There are three jetted TDEs, and neutrino emission is most promising from this category

These three jetted TDEs share similar properties, namely that they were all sufficiently bright to be discovered serendipitously by observations of the *Swift*-BAT X-ray telescope. They each have well-sampled lightcurves, with the time of jet-launching constrained to a window of a few days. Given the consistent observational features of luminous, hard X-ray emission which rapidly fades, it is likely that all three objects are indeed jetted TDEs. The jetted TDEs were used to test Hypothesis 1.

Hypothesis 2 could then be tested with the remaining “non-jetted” TDEs, defined as those TDEs without on-axis relativistic jets. These non-jetted TDEs form an observationally-distinct class of objects. They may have off-axis relativistic jets, or mildly relativistic outflows, but none exhibit the characteristic hard X-ray emission associated with on-axis relativistic jets .

Beyond this, the properties of non-jetted TDEs are highly heterogeneous. They are discovered across a range of wavelengths (e.g X-ray, Optical, IR)

**Table 3.1:** Summary of the four TDE catalogues..

Catalogue	Source Class	Size	Description
Jetted	Jetted TDEs	3	<i>Probable TDEs with on-axis jets</i>
Golden	Non-Jetted TDEs	13	<i>Probable TDEs with convincing classification</i>
Silver	Non-Jetted TDEs	24	<i>Candidate TDEs with ambiguous classification</i>
Obscured	Non-Jetted TDEs	13	<i>Candidate TDEs in dusty galaxies</i>

with varying multi-wavelength coverage. There are a handful of compelling TDE candidates, often with comprehensive multi-epoch spectroscopic observations, for which alternative explanations are disfavoured. However, in the vast majority of cases, a definite classification cannot be made. To avoid contamination from misclassified objects, primarily AGN or SN, we define a clean "golden sample" consisting solely of reliably-classified TDEs:

- ▶ **Golden TDEs** are strong candidates where the TDE interpretation is supported by multiple spectra

The remaining objects are then candidate TDEs, with a possible but not definitive classification.

There is one distinct subclass of candidates, containing flares observed in dusty galaxies via IR emission [123]. One possible explanation is that the flares arise from a dust-obscured TDE, with the dust then slowly reprocessing the electromagnetic radiation from the galaxy core. For such reprocessing, there would be a time delay between the disruption itself and the corresponding IR flare. As we expect that neutrinos should begin soon after disruption, the timescale for neutrino emission from obscured TDEs would have significant additional uncertainty.

[123]: Wang et al. (2018), "Long-Term Decline of the Mid-Infrared Emission of Normal Galaxies: Dust Echo of Tidal Disruption Flare?"

We thus treat these candidate *obscured TDEs* separately from the other candidate TDEs:

- ▶ **Obscured TDEs** are TDE candidates which occur in very dusty galaxies, and are only observed via reprocessed infra-red emission.
- ▶ **Silver TDEs** are all other candidates, where a TDE interpretation is either likely or not disfavoured.

All catalogues are summarised in Table 3.1, with full details provided in the Appendix (Chapter A).

## Search Windows

To account for the heterogeneous datasets, an individual search window was defined for each TDE, with the aim for identifying the period of peak electromagnetic emission. For jetted/gold/silver TDE, the following criteria were used:

- ▶ For TDEs in which the light curve was observed when rising, the first detection is taken as the window start.
- ▶ For TDEs without an observation during lightcurve rise, the last upper limit is taken as the window start.
- ▶ The maximum date was taken as the date on which the brightest TDE luminosity measurement was performed.

**Table 3.2:** Summary of results for the four TDE catalogues. For each, an independent stacking analysis was performed. The catalogues covered sources from May 2008 to October 2017, matching the IceCube data-taking period.

Catalogue	Source Class	Size	$n_s$	$\gamma$	TS	Pre-trial p-value
Jetted	Jetted	3	1.5	4.0	0.8	0.40
Golden	Non-Jetted	13	3.9	2.4	2.4	1.00
Silver	Non-Jetted	24	15.6	2.7	7.9	1.00
Obscured	Non-Jetted	13	29.4	2.8	14.8	0.04

- ▶ The window extends from the defined window start to 100 days after the maximum date

30 days

Applying these criteria gives a tailored search window for each TDE. Obscured TDEs instead had a search window extending from 300 days before peak to 100 days after peak, to account for potential delay following neutrino emission. The search window for each source is provided in Appendix Chapter A. It is the first such catalogue to contain time windows, and could also be used for stacking analyses of e.g gamma-ray emission.

## Analysis and Results

As outlined in Chapter 1, a standard *stacking analysis* requires an additional assumption on the expected relative neutrino emission of each source in a catalogue. However, these TDE catalogues are characterised by small numbers of heterogeneous sources. With a mix of observation cadences and multi-wavelength coverage, there is no obvious proxy for neutrino emission. A common standard-candle approximation, in which each source has the same intrinsic luminosity, is also not well-motivated. There is no evidence of standard-candle behaviour in EM wavelengths, so there is no reason to think it would hold for neutrino emission. We are left with no clear method to compare the relative contributions, and for this reason, an agnostic approach is instead applied. Using the method outlined in Section 1.10, we fit the contribution of each source in the catalogue individually, requiring only that they share a common neutrino spectrum.

Following the procedure in Chapter 1, we perform an unbinned likelihood analysis to obtain results for each catalogue, with fit parameters TS,  $\gamma$  and a number of signal events for each source ( $n_k$ ). We also obtain a final Test Statistic (TS) value, and calculate a p-value for this TS using pseudotrials. Table 3.2 summarises the results for each catalogue, including  $n_s = \sum n_k$ . The individual  $n_k$  values are provided in the Appendix Chapter A.

There was no significant correlation identified for any of the catalogues. While the Obscured TDE catalogue yielded the most significant pre-trial p-value, after trial correction using Equation 1.18 this is reduced to a value of  $p_{\text{post-trial}}=0.15$ , and is thus entirely consistent with background expectations. No discovery of neutrino emission from TDEs is claimed, and *we do not reject the null hypothesis that TDEs and neutrinos are uncorrelated*.

## Catalogue limits

Being unable to reject the null hypothesis, we can instead set an upper limit on neutrino emission, by ruling out scenarios for which we would have expected to reject the null hypothesis. We follow the procedure outlined in Section 1.6 to set an upper limit, at 90% confidence, using pseudoexperiments with simulated signal. In common with most IceCube studies, these limits are only valid *under the assumption that the signal looks like the baseline IceCube MC*, and thus that *the impact of all systematic effects are negligible*.

While our search results in Table 3.2 are agnostic to the relative neutrino contribution of each source, any pseudoexperiments involving simulated signal must make an assumption regarding the intrinsic neutrino luminosity of each source. Though it remains a poor approximation for EM emission, we inject neutrinos under *the assumption that each catalogue source emits the same number of neutrinos according to the same intrinsic energy spectrum*, i.e that TDEs are neutrino standard candles. The corresponding flux on Earth is thus proportional to the inverse distance squared of each source. This flux is injected uniformly across the search windows for each source, as defined in Appendix (Chapter A). To conserve energy, and the flux-per-source is then inversely proportional to the length of the search window.

The intrinsic energies are presented as *isotropic-equivalent*, and thus quoted assuming that the emission is emitted isotropically. This is of particular relevance for the Jetted TDEs, for which emission is likely to be highly beamed. As the exact beaming angle is unclear, it is conventional to present such isotropic-equivalent values for comparison, with the true energy likely to be somewhat lower. All limits derived below are only valid in the case that all of these assumptions are true. Upper limits are derived for combined neutrino+anti-neutrino emission under the *assumption of an unbroken neutrino power law, between 100 GeV and 10 PeV*, for a variety of spectral limits. These upper limits are shown in Figure 3.1, in units of integrated neutrino+anti-neutrino per-flavour energy for each source.

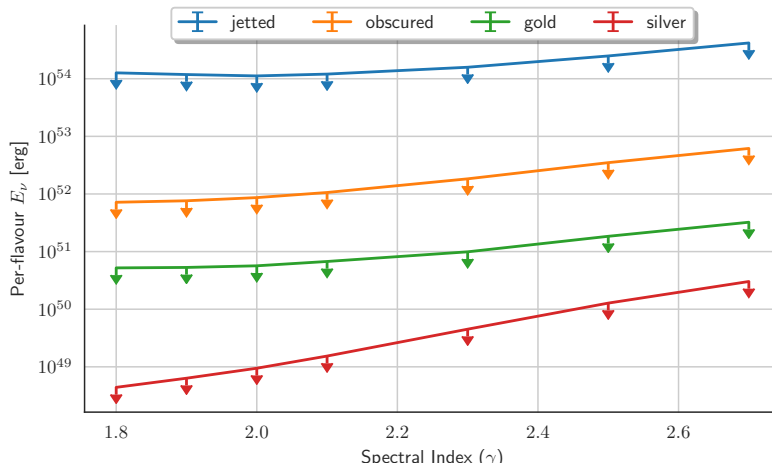


Figure 3.1: Limits on the neutrino emission for each catalogue.

## Population limits

While the limits presented above constrain the contribution of those catalogues tested, we ultimately wish to constrain neutrino emission for the TDE population as a whole. If we *assume that catalogue sources are representative of the broader population*, we can extrapolate from our per-source standard candle limits in Figure 3.1 to the population flux. We seek to constrain the flux of two populations, namely jetted and non-jetted TDEs. For the latter case, we rely on the results of the golden TDE catalogue, since the extrapolation *implicitly requires that the catalogues are not contaminated by misclassified objects*.

[104]: Aartsen et al. (2015), “A Combined Maximum-likelihood Analysis of the High-energy Astrophysical Neutrino Flux Measured with IceCube”

[124]: van Velzen (2018), “On the Mass and Luminosity Functions of Tidal Disruption Flares: Rate Suppression due to Black Hole Event Horizons”

[118]: Sun et al. (2015), “Extragalactic High-energy Transients: Event Rate Densities and Luminosity Functions”

Using the most recent IceCube global fit of the astrophysical neutrino flux [104], with a best-fit spectrum of  $E^{-2.50}$ , we follow the procedure outline in Chapter 2. We combine the golden TDE per-source limit shown in Figure 3.1, with a central local rate of  $8 \times 10^{-7} \text{ Mpc}^{-3} \text{ year}^{-1}$  [124] and a TDE source evolution [118] parameterised as:

$$\rho(z) \propto \left( (1+z)^{-0.4} + \left( \frac{1+z}{1.43} \right)^{6.4} + \left( \frac{1+z}{2.66} \right)^{14} \right)^{-\frac{1}{2}} \quad (3.1)$$

With this evolution, we constrain the contribution of non-jetted TDEs to be less than 25.3% of the total. For jetted TDEs, under the assumption that they follow the same underlying source evolution in Equation 3.1 with a central rate of  $3 \times 10^{-11} \text{ Mpc}^{-3} \text{ year}^{-1}$  [118], we find that they must contribute less than 1.3% of the total. These constraints are illustrated in Figure 3.2.

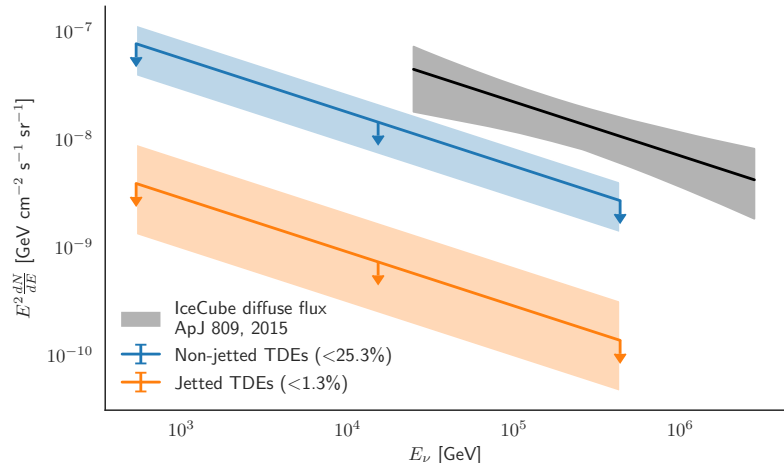


**Figure 3.2:** Limits on the contribution of jetted and non-jetted TDEs to the diffuse neutrino flux.

As the contribution from a population is directly proportional to the local population rate, the shaded bands indicate the uncertainty in our limits arising from rate estimates. For TDEs, these rates are a large source of uncertainty in neutrino flux. It will require systematic evaluation of observed TDE rates to enable more precise limits on neutrino emission. Any refined rate estimate can be used to linearly rescale these limits. Propagating through the current local rate uncertainty, we constrain non-jetted TDEs to be less than 12.7% - 38.0%, and jetted TDEs to be less than 0.4% - 3.0% of the total. With a more precise future measurement of

the local TDE rate, these values can be linearly rescaled to provide more accurate limits.

Such limits also critically depend on the source evolution of TDEs as a function of redshift, but this is not strongly constrained observationally because TDEs detections are generally confined to the local universe ( $z \lesssim 0.3$ ). Estimates are made primarily based on theoretical predictions derived from the rate of supermassive black holes (see Chapter 2) [118]. We can instead consider a source evolution similar to the Star Formation Rate (SFR) [116], parameterised as:

$$\rho(z) \propto \frac{(1+z)^{2.7}}{1 + ((1+z)/2.9)^{5.6}} \quad (3.2)$$

[116]: Madau et al. (2014), “Cosmic Star-Formation History”

With Equation 3.2, we would then find limits of 108.3% (54.2% - 162.5%) for non-jetted TDEs and 5.5 % (1.8% - 12.8%) for jetted TDEs. These limits are shown in Figure 3.3. For such a scenario, the contribution of unresolved non-jetted TDEs is so large that the measured flux itself provides a stricter constraint than the catalogue test. However, even in that extreme scenario, the contribution of jetted TDEs to the diffuse neutrino flux remains subdominant.

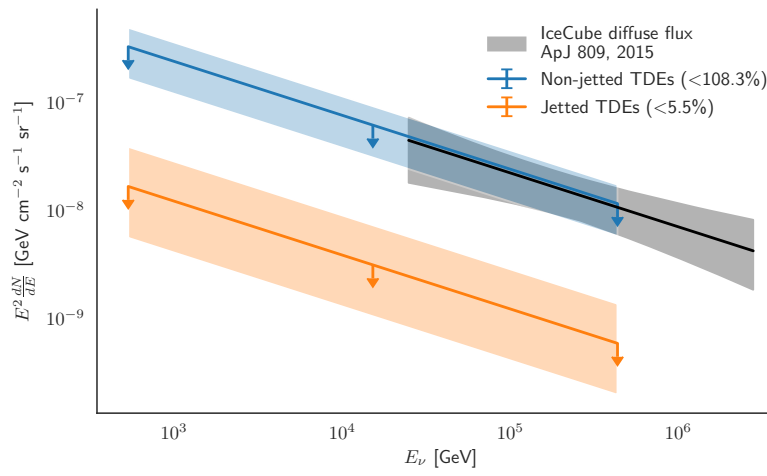


**Figure 3.3:** Limits on the contribution of jetted and non-jetted TDEs to the diffuse neutrino flux, under the assumption of a source evolution proportional to the Star Formation Rate.

## Individual TDEs

In addition to the stacking analysis, four TDEs were selected for individual analysis. Two of the three jetted TDEs, Swift J1644+57 and Swift J2058+05, were chosen due to their luminosity, as well as their position in the northern hemisphere where IceCube has the highest effective area. In addition, ASSASN-14li and XMMSL1 J0740-85 were chosen as non-jetted TDEs which were both nearby and bright. These four TDEs were the only catalogue sources that were also detected in radio observations, typically a tracer for relativistic particle acceleration. For each of the four individual TDEs, searches were conducted for neutrino clustering in both time and space, following the procedure outlined in Section 1.9. All single-object tests are described in Table 3.3.

The results of each fit are provided in Table 3.3, alongside pre-trial p-values. No significant emission was identified, and no discovery is claimed.

**Table 3.3:** Summary of the five individual TDEs for which the temporal-cluster-search method was applied. All but AT2018cow were included in the stacking analysis.

Source	R.A (deg.)	Dec (deg.)	T <sub>0</sub> (MJD)	T <sub>1</sub> (MJD)	n <sub>s</sub>	γ	t <sub>s</sub> (MJD)	t <sub>e</sub> (MJD)	TS
Swift J1644+57	251.21	57.58	55644.00	55749.00	0.68	1.98	55650.90	55746.25	0.06
Swift J2058+05	314.58	5.23	55694.00	55798.00	2.78	4.00	55774.25	55780.00	2.28
ASASSN-14li	192.06	17.77	56851.00	57072.00	2.95	2.53	57022.68	57032.75	1.52
XMMSL1 J0740-85	115.03	85.66	56718.00	56848.00	2.84	2.19	56806.95	56807.51	3.49
AT2018cow	244.00	22.27	58256.90	58386.90	5.91	2.98	58283.83	58298.53	3.91

Instead, upper limits are derived on neutrino emission for each source. As described in Section 1.9, the cluster-search method is more sensitive to shorter-scale emission. Upper limits were derived under the conservative assumption that neutrino emission was distributed uniformly in the search window, with any emission on shorter timescales being more constrained.

## 3.2 AT2018cow and FBOTs

Following the four stacking analyses and four cluster-search analyses described above, an additional analysis was later performed on AT2018cow [66], a transient first discovered in 2018. It is now thought that AT2018cow was a nearby example of the recently-identified population known as “Fast Blue Optical Transients” (FBOTs) introduced in Chapter ??.

However, at the time of discovery, AT2018cow was initially thought to be a bright Broad-Lined type Ic (Ic-BL) supernova, and thus a member of the rare subclass associated with long GRBs and relativistic jets [125]. As outlined in Chapter ??, many models predict that such SNe may be neutrino sources, so an IceCube *Fast Response Analysis* was run on AT2018cow shortly after discovery [38]. The IceCube search targeted choked-jet neutrino emission, and thus covered the 3-day period from the last non-detection to the first detection, aiming to isolate the supernova explosion time at which the neutrino emission would be expected. Ultimately, an excess of neutrinos was found in this time period, with a significance of  $1.8\sigma$  [126]. The excess itself consisted of two signal-like neutrinos, which were considered significant owing to the small expected background for such a short search window.

Later multi-wavelength observations of AT2018cow were not consistent with a traditional Ic-BL SN, and the transient was later identified as a nearby example of an FBOT [67]. The exact nature of these FBOTs had been difficult to probe, since they were primarily discovered at high redshift [65], but promptly-identified AT2018cow at 60 Mpc provided a rich multi-wavelength dataset. It has since variously interpreted as a TDE with an Intermediate-Mass Black Hole, an extreme supernova or a Magnetar . In light of these developments, AT2018cow was re-analysed by the author in the context of a potential TDE classification. As for the other four individual TDEs detailed above, a dedicated search for neutrino clustering on timescales up to 130 days, extending from 30 days before peak to 100 days afterwards, was undertaken. For this purpose, an additional year of IceCube data extending to October 2018 was analysed.

[66]: Margutti et al. (2019), “An Embedded X-Ray Source Shines through the Aspherical AT 2018cow: Revealing the Inner Workings of the Most Luminous Fast-evolving Optical Transients”

[125]: Woosley et al. (2006), “The Supernova Gamma-Ray Burst Connection”

[38]: Abbasi et al. (2020), “Follow-up of astrophysical transients in real time with the IceCube Neutrino Observatory”

[126]: Blaufuss (2018), “AT2018cow: IceCube neutrino search”

[67]: Perley et al. (2019), “The Fast, Luminous Ultraviolet Transient AT2018cow: Extreme Supernova, or Disruption of a Star by an Intermediate-Mass Black Hole?”

In this analysis of AT2018cow, a small excess was again found. Although the best-fit cluster from this search included the two signal-like neutrinos from the original IceCube analysis, when accounting for the expected fluctuations arising from background over the much longer 130 day search window, the significance of the excess was just  $0.5\sigma$ . The result is thus entirely consistent with expectations from atmospheric background, while not contradicting the original result published at the time. As such, no discovery is claimed and upper limits for AT2018cow are accordingly derived (illustrated in Figure 3.4). Though AT2018cow was not included in the catalogues when the stacking analysis was performed, it would naturally belong to the silver non-jetted TDE sample.

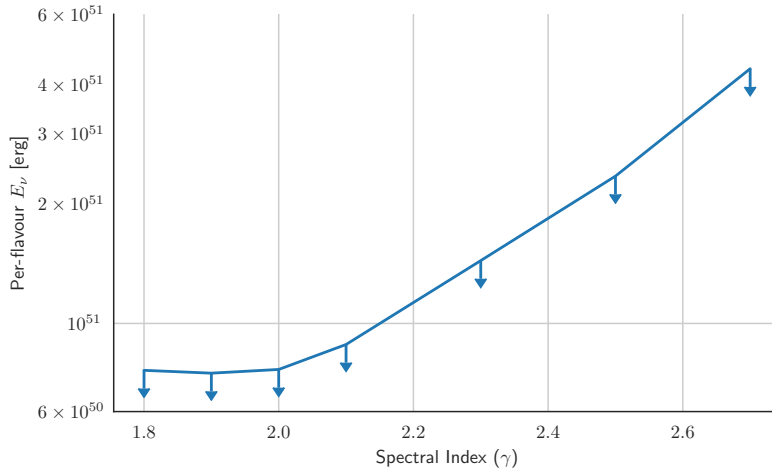


Figure 3.4: Limits on neutrino emission from AT2018cow, as a function of spectral index.

The analysis of AT2018cow is the first example of a test for neutrino emission from FBOTs. In the time since discovery in 2018, there have been theoretical studies considering possible neutrino emission from FBOTs in general, and AT2018cow in particular [127]. The predicted neutrino emission is typically several orders of magnitude below the limits presented in Figure 3.4, and thus further supports the likely atmospheric origin for the neutrino excess [126].

However, given that AT2018cow is by far the closest example of an FBOT, we can already consider the implications for the broader FBOT population emission. While initial estimates suggested that these objects might equal  $\sim 4\text{-}7\%$  of the CCSN rate [65, 127], these estimates have been superseded by results from magnitude-limited surveys such as ZTF, where a lack of additional FBOTs strongly suggest that the local rate must be  $\sim 0.1\%$  of the CCSN rate [ADD CITATION WHEN ZTF FBOT PAPER IS OUT]

Following the same procedure for TDEs, we find that FBOTs contribute less than 16% of the total diffuse neutrino flux *assuming that AT2018cow is representative of the broader FBOT population*. This further assumes a CCSN-like source evolution [116], proportional to the star formation rate, and a local FBOT rate of  $4 \times 10^{-7} \text{ Mpc}^{-3} \text{ yr}^{-1}$  [128]. These limits are agnostic to the exact nature of FBOTs, whether they are a distinct population or a rare subgroup of some broader object class. In any case, it is clear that any contribution of FBOTs to the diffuse neutrino flux must be subdominant.

[127]: Fang et al. (2019), “Multimessenger Implications of AT2018cow: High-energy Cosmic-Ray and Neutrino Emissions from Magnetar-powered Superluminous Transients”

[116]: Madau et al. (2014), “Cosmic Star Formation History”

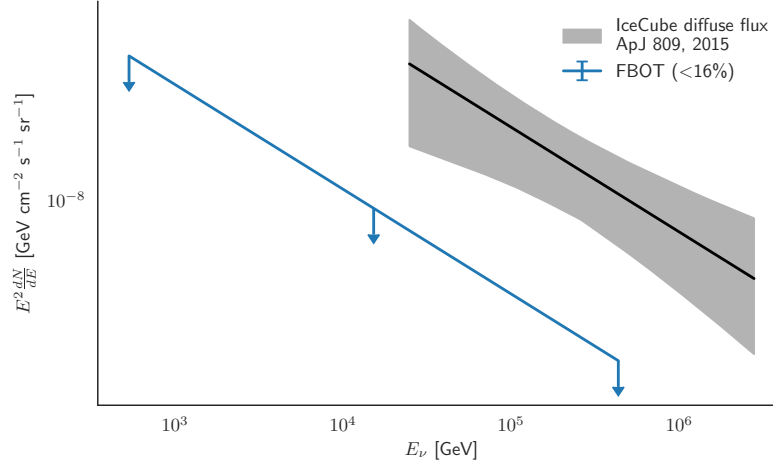


**Figure 3.5:** Limits on neutrino emission from FBOTs, using the limits from AT2018cow under the assumption of neutrino standard candles.

### 3.3 Robustness of Limits

[95]: Aartsen et al. (2020), “Time-Integrated Neutrino Source Searches with 10 Years of IceCube Data”

[129]: Aartsen et al. (2017), “All-sky Search for Time-integrated Neutrino Emission from Astrophysical Sources with 7 yr of IceCube Data”

One key additional point is how robust the derived constraints are, given the many stated caveats. Full systematic studies are not typically re-performed for each individual IceCube neutrino source analysis [95]. This is due primarily to evidence from previous studies which demonstrated that the impact of systematic uncertainties on a typical Icecube neutrino point source search is  $O(\sim 10\%)$ , dominated by uncertainty on ice optical properties and DOM performance [129]. This value is completely negligible in comparison to uncertainties on astrophysical population rates, as well as to additional uncertainties on the relative distribution of neutrinos across an astrophysical population.

The searches introduced above are time-dependent analyses performed on specific windows, and are thus completely insensitive to any neutrino emission which may fall outside these windows. However, while the duration of neutrino emission may be uncertain for transients, it is expected that at least some substantial fraction of neutrino emission should occur during the periods of peak electromagnetic brightness. Thus the limits derived above can be extrapolated to cover neutrino emission models extending beyond the tested period. For example, if one predicts that only 50% of neutrino emission from Jetted TDEs would occur in the first 100 days, the population limit would twice as high (2.6% rather than 1.3%) but still constraining.

A similar argument can be applied for deviations from an unbroken neutrino power law. For TDEs this would not be surprising, because the neutrino production models introduced in Chapter ?? would instead favour a peaked neutrino spectrum. However, while the energy weightings illustrated in Figure 1.7 are based on different power laws, the likelihood analysis will detect excesses from any neutrino spectrum. If the signal follows the same energy distribution of the background, the energy term in the Point Source Likelihood (Equation 1.17) will provide no discriminating power, but the analysis can still identify the corresponding spatial clustering. If however there is an additional excess of neutrinos at either high or low energies, that can be well-approximated by a hard or soft neutrino power law respectively. Given that discoveries can be made with just 10-20 neutrinos, the vast majority of which will be at

low energies, the ultimate difference in sensitivity for different spectra is minimal. This can be seen from Figure N, where the sensitivity is illustrated as a function of true neutrino energy. In the range X to Y, this does not vary by much, and thus any neutrino emission in this range will be strongly constrained regardless of spectrum.

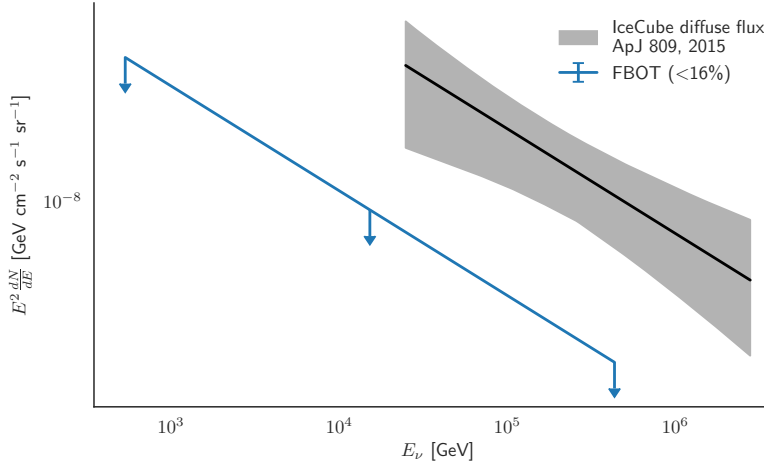


**Figure 3.6:** Sensitivity of the Point Source Likelihood for a point source as a function of energy.

As was demonstrated for both TDEs and FBOTs, uncertainty on the properties of a given astrophysical population remains an important source of uncertainty in constraining the overall population neutrino emission. The local rate itself remains challenging to constrain particularly for rare transient classes such as jetted TDEs or FBOTs, though wide-field time-domain surveys such as ZTF and LSST should lead to continuing improvements in precision. Constraining the rate evolution is more challenging, particularly because even deep surveys such as LSST will not probe transient rates at very high redshift where much of the neutrino emission is expected. Ultimately this source of uncertainty will likely continue to dominate limits even with next-generation neutrino detectors and transient surveys.



# **OPTICAL FOLLOW-UP WITH ZTF**





## 4 AT2019dsg

“ We are all in the gutter, but some of us are looking at the stars ”

Oscar Wilde, *Lady Windermere’s Fan*, 1893

One key result of this thesis was the identification of a Tidal Disruption Event, *AT2019dsg*, as a probable high-energy neutrino source. The object was found using the *AMPEL Follow-up Pipeline* as part of our ZTF neutrino follow-up program, (see Chapter ??), during a follow-up campaign for high-energy neutrino *IC91001A* (see Chapter ??). The association was first identified by the author, who led a multi-wavelength observation campaign to characterise this object. The data and analysis presented in this chapter are therefore the result of a collaboration between many people, not the sole work of the author. These results have also been published as a paper [130].

### 4.1 Observations of AT2109dsg

On 2019 October 1, the IceCube Neutrino Observatory reported the detection of a  $\sim 0.2$  PeV neutrino, *IC191001A*, with a 59% probability of being of astrophysical origin [131] (see Chapter ??). The event itself is shown in Figure 4.1. Seven hours later, the direction of the incoming neutrino was observed by ZTF as part of our neutrino follow-up program. The data was processed by the author’s multi-messenger pipeline introduced in Chapter ??, and the radio-emitting tidal disruption event *AT2019dsg* was identified as a candidate neutrino source [132].

4.1 Observations of AT2109dsg	49
4.2 Probability of Chance Coincidence . . . . .	60
4.3 Neutrino production in AT2019dsg . . . . .	61
4.4 Compatibility with stacking limit . . . . .	65
4.5 Implications of AT2019dsg . . . . .	67

[130]: Stein et al. (2021), “A tidal disruption event coincident with a high-energy neutrino”

[131]: Stein (2019), “IceCube-191001A - IceCube observation of a high-energy neutrino candidate event”

[132]: Stein et al. (2019), “Candidate Counterparts to IceCube-191001A with ZTF”

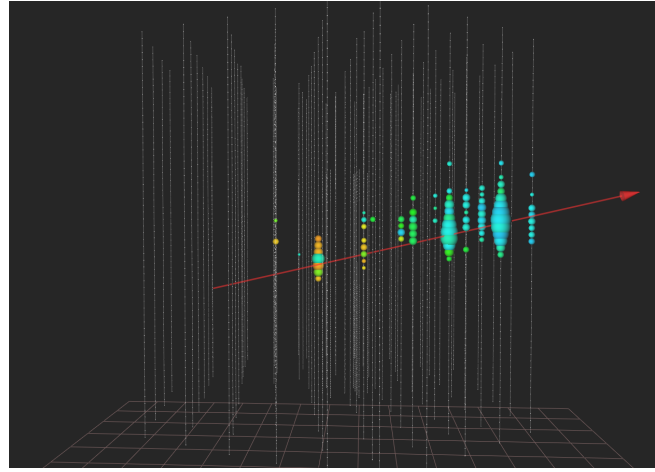


**Figure 4.1:** Visualisation of IC191001A in the IceCube detector. The colour corresponds to the light arrival time, from early orange pulses on the left to late blue ones on the right. The arrow illustrates the best fit reconstructed trajectory of the event.

AT2019dsg (R.A.[J2000] = 314.26 deg, Dec[J2000] = +14.20 deg) was spatially coincident with the 90% localisation of the neutrino IC191001A (R.A. =  $314.08^{+6.56}_{-2.26}$  deg, Dec =  $+12.94^{+1.50}_{-1.47}$  deg) [131], at a distance of 1.27 deg to the best-fit position. It was also temporally coincident, being detected by ZTF in the ToO observations following the neutrino detection. There were additionally three candidate supernovae found in the error region of IC191001A, consistent with background expectations.

AT2019dsg was the first TDE identified by our pipeline, and the first TDE to be reported in coincidence with any high-energy neutrino. As introduced in Chapter ??, TDEs have long been predicted as sources of neutrinos, where those TDEs with non-thermal emission are considered the most likely to be sources of high-energy neutrinos. Having already been detected at radio wavelengths, AT2019dsg was thus quickly identified as a promising candidate counterpart. The following subsections detail the electromagnetic observations of AT2019dsg, as published in [130], but were not led by the author of this work.

## UV/Optical Observations

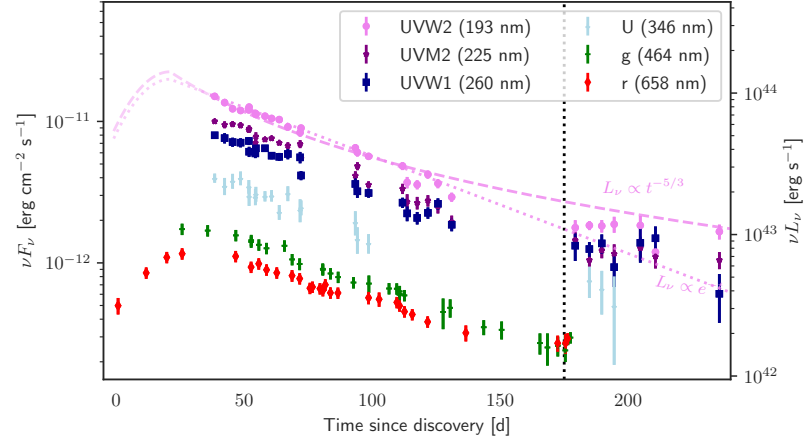


**Figure 4.2:** UV/Optical photometry of AT2019dsg. The vertical dotted line illustrates the arrival of IC191001A.

[133]: Nordin et al. (2019), “ZTF Transient Discovery Report for 2019-04-22”

AT2019dsg was first discovered by ZTF on 2019 April 9 [133], and was had already been repeatedly detected by ZTF P48 telescope as part of the

public MSIP survey prior to the detection of IC191001A. These data were also supplemented by photometric observations from the 2m Liverpool Telescope [134] and SEDM [135] photometry obtained using the P60 telescope on Mt Palomar. AT2019dsg was selected as a probable TDE as part of a systematic search for optical TDEs with ZTF, each of which is assigned a nickname based on a character from HBO’s TV Series *Game of Thrones*, and was accordingly dubbed *ZTF-BranStark* [59].

UV observations of AT2019dsg were conducted as part of a systematic survey of UV properties of all ZTF-identified TDEs [59], using the Ultra-Violet/Optical Telescope (UVOT) on board the *Neil Gehrels Swift Observatory (Swift)* [136, 137]. The first UV observation was performed 15 days after the optical peak on 2019 May 17, and a bright source spatially coincident with the TDE was detected. Subsequent observations continued at a cadence of 2–3 days, up to 2019 September 7. In this period, AT2019dsg continued to steadily dim. An additional observation occurred shortly before the neutrino detection on 2019 September 27. Follow-up observations were then triggered by the identification of a possible association with IC191001A, beginning on 2019 October 5.

Like most TDEs [59], the optical/UV continuum of AT2019dsg was well described by a single blackbody photosphere. For AT2019dsg, this had an inferred radius of  $10^{14.59 \pm 0.03}$  cm and a near-constant inferred temperature of  $10^{4.59 \pm 0.02}$  K, with the latter being in the top 5% of the 40 known optical TDEs to date [59]. AT2019dsg was also particularly noteworthy for its high bolometric energy flux, the second highest of the ZTF sample. Not only was AT2019dsg relatively nearby for a TDE, but the peak luminosity of  $10^{44.54 \pm 0.08}$  erg s<sup>-1</sup> was in the top 10% of known optical TDEs [59].

The late-time evolution, with an apparent UV plateau, is inconsistent with the canonical expectations for a steady power-law or exponential decay introduced in Chapter ???. However, this behaviour is compatible with the rapid formation of an accretion disk [138], which would be expected on these relatively short timescales for disruptions around higher-mass SMBHs. The total mass of the host galaxy of AT2019dsg is indeed in the top 10% of all optical TDEs, with an estimated black hole mass of  $\sim 3 \times 10^7 M_\odot$  using a galaxy bulge scaling relation [59], further supporting this explanation. The source also appeared to redden in the optical bands at late times, a possible signature of reverberation due emission from TDE-heated dust which has been observed previously for some other objects [139].

## X-ray Observations

As shown in Figure 4.3, AT2019dsg was also detected in X-rays beginning 37 days after discovery. It was first observed on 2019 May 17 by the X-Ray Telescope (XRT) [140], also on board *Swift* [137], as part of a program to categorise the X-ray properties of TDEs [59]. Observations continued with a cadence of 2–3 days, and indicated a sharply-declining X-ray flux. One more sensitive observation was performed with the *X-ray Multi-Mirror Mission (XMM-Newton)* telescope [141] on 2019 May 30, with the source clearly visible as seen in Figure 4.4. AT2019dsg was last detected by XRT on 2019 June 14, and not detected again in any of the

[134]: Steele et al. (2004), “The Liverpool Telescope: performance and first results”

[135]: Blagorodnova et al. (2018), “The SED Machine: A Robotic Spectrograph for Fast Transient Classification”

[59]: van Velzen et al. (2020), “Seventeen Tidal Disruption Events from the First Half of ZTF Survey Observations: Entering a New Era of Population Studies”

[136]: Roming et al. (2005), “The Swift Ultra-Violet/Optical Telescope”

[137]: Gehrels et al. (2004), “The Swift Gamma-Ray Burst Mission”

[138]: Mummery et al. (2020), “The spectral evolution of disc dominated tidal disruption events”

[139]: van Velzen et al. (2016), “Discovery of Transient Infrared Emission from Dust Heated by Stellar Tidal Disruption Flares”

[140]: Burrows et al. (2005), “The Swift X-Ray Telescope”

[137]: Gehrels et al. (2004), “The Swift Gamma-Ray Burst Mission”

[141]: Jansen et al. (2001), “XMM-Newton observatory. I. The spacecraft and operations”

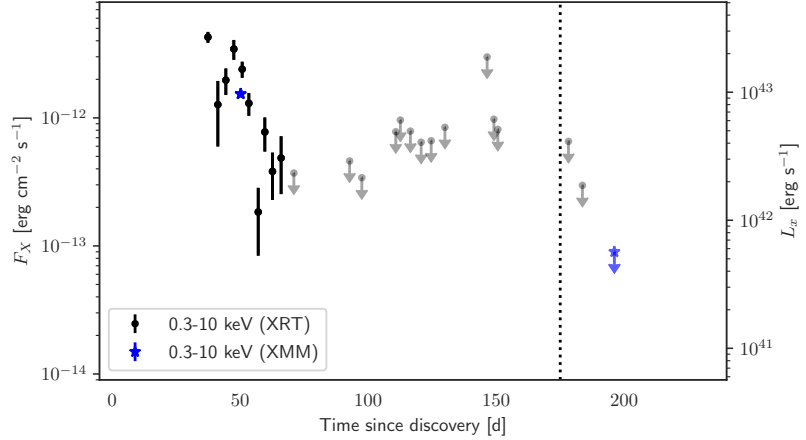


**Figure 4.3:** X-ray lightcurve of AT2019dsg. The vertical dotted line illustrates the arrival of IC191001A.

following observations continuing until 2019 September 7. Following the identification of AT2019dsg as a candidate counterpart to IC191001A, additional X-ray observations were triggered but AT2019dsg was again not detected. An additional *XMM* observation on 2019 October 23 yielded a deep upper limit of  $9 \times 10^{-14}$  erg cm<sup>-2</sup> s<sup>-1</sup> (0.3–10 keV).

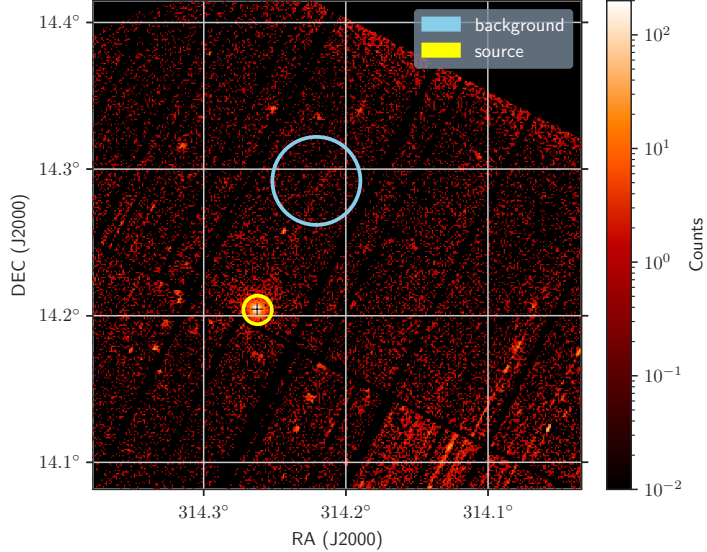


**Figure 4.4:** X-ray count map from *XMM-Newton* (50 days after discovery). The yellow circle indicates the source region, while the blue circular region was used to measure the background.

Though the first X-ray observation indicated a bright source, with a high X-ray to optical ratio of  $L_X/L_{\text{opt}} \sim 0.1$ , this X-ray flux faded extremely rapidly. This rate of decline is unprecedented, with at least a factor of 50 decrease in X-ray flux over a period of 159 days. Similar to the optical/UV emission, the observed X-ray spectrum was consistent with thermal emission, but from a blackbody of temperature  $10^{5.9}$  K ( $0.072 \pm 0.005$  keV) and, assuming emission from a circular disk, a radius  $\sim 2 \times 10^{11}$  cm. This can be seen in Figure 4.5. Since these X-ray observations probe close to the Wien tail of the thermal spectrum, the observed exponential decrease of the X-ray flux could simply be caused by cooling of the newly-formed TDE accretion disk [138], or it could instead result from increasing X-ray obscuration.

[138]: Mummery et al. (2020), “The spectral evolution of disc dominated tidal disruption events”

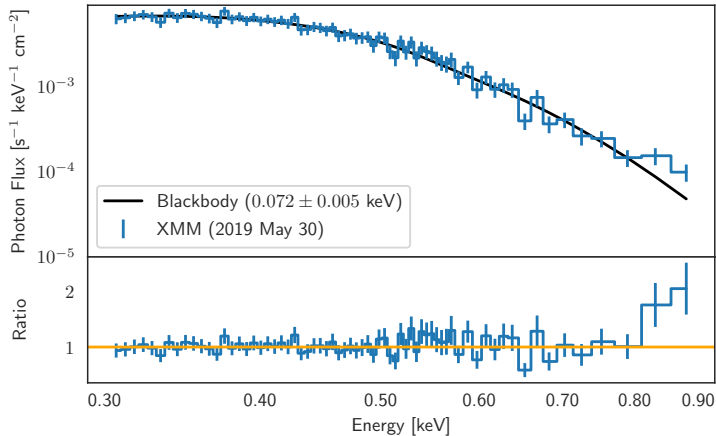


**Figure 4.5:** Soft X-ray spectrum of AT2019dsg measured by *XMM-Newton*, fitted with an absorbed disk blackbody model.

As for most X-ray-detected TDEs, the blackbody radius appears much smaller than the Schwarzschild radius ( $R_S \sim 10^{13}$  cm) inferred from galaxy scaling relations [142]. Because X-ray emission is generally expected to arise close to the Schwarzschild radius, this inferred X-ray blackbody radius can be misleading. Small emitting areas can arise from an edge-on orientation, because the relativistic velocities at the inner disk can Doppler boost a large area of the disk out of the X-ray band. Additionally, when extrapolating from the Wien tail behaviour, any decrease in inferred temperature due to unaccounted-for absorption would lead to a significantly underestimated blackbody radius and luminosity.

## Radio Observations

Quasi-simultaneous radio observations of AT2019dsg were conducted across a range of frequencies using the Karl G. Jansky Very Large Array (VLA) [143], the AMI Large Array (AMI-LA) [144], and the MeerKAT telescope [145]. These observations are shown in Figure 4.6. For all radio observations, the reported uncertainties include both the image background rms and a 5% fractional calibration uncertainty, added in quadrature.

The four radio spectral energy distributions (SEDs) for AT2019dsg can be described by transient synchrotron emission from a population of relativistic electrons. It was assumed that the electrons are accelerated into a power-law distribution in energy  $dN_e/d\gamma \propto \gamma^{-P}$ . In addition to the transient radio emission from AT2019dsg, the observations also contain some steady radio emission from the host galaxy. This baseline flux density was parameterised as:

$$F_{\nu, \text{baseline}} = F_{\text{baseline}} \left( \frac{\nu}{1.28 \text{ GHz}} \right)^{\alpha_{\text{baseline}}} \quad (4.1)$$

such that the total flux density is given by :

$$F_{\nu, \text{total}} = F_{\nu, \text{baseline}} + F_{\nu, \text{sync}} \quad (4.2)$$

[142]: McConnell et al. (2013), “Revisiting the Scaling Relations of Black Hole Masses and Host Galaxy Properties”

[143]: Perley et al. (2011), “The Expanded Very Large Array: A New Telescope for New Science”

[144]: Zwart et al. (2008), “The Arcminute Microkelvin Imager”

[145]: Jonas (2009), “MeerKAT - The South African Array With Composite Dishes and Wide-Band Single Pixel Feeds”

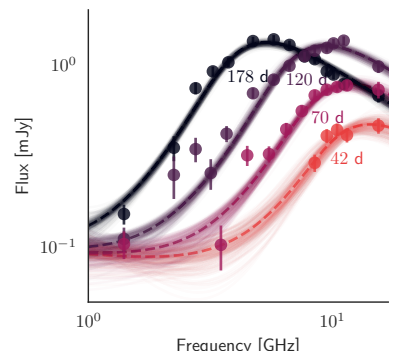


**Figure 4.6:** Radio observations of AT2019dsg.

**Table 4.1:** Peak frequency and peak flux density of the radio observations.

$\Delta t$ (days)	$F_{\text{peak}}$ (mJy)	$\nu_{\text{peak}}$ (GHz)
42	$0.41 \pm 0.04$	$14.8 \pm 1.0$
70	$0.71 \pm 0.04$	$12.0 \pm 0.5$
120	$1.20 \pm 0.04$	$9.4 \pm 0.3$
178	$1.24 \pm 0.04$	$5.4 \pm 0.1$

However, given the dramatic change in radio spectra between observation epochs, it is immediately clear that the majority of emission is indeed related to the transient rather than a steady host baseline. As outlined in Chapter ??, *synchrotron self-absorption* will suppress the observed flux up to a threshold frequency, leading to a characteristic break in the synchrotron emission spectrum. This break is also clearly visible for each epoch shown Figure 4.6. The intrinsic electron power law can be inferred from the *optically-thin* (high-frequency) component of the spectrum, along with the break frequency itself (the *synchrotron self-absorption frequency*).

[146]: Foreman-Mackey et al. (2013), “emcee: The MCMC Hammer”

A Markov chain Monte Carlo approach [146] was applied to determine a posterior probability distribution of the electron power-law index, as well as the peak frequency ( $\nu_{\text{peak}}$ ) and peak flux density ( $F_{\text{peak}}$ ) for each radio epoch. The measurement variance was allowed to be underestimated by some fractional amount  $f$ . The results are listed in Table 4.1. The resultant best fit is an electron spectrum with index  $p = 2.9 \pm 0.1$ , and a baseline with flux density  $F_{\text{baseline}} = 0.09 \pm 0.01$  mJy and spectral index  $\alpha_{\text{baseline}} = -0.2 \pm 0.1$ , along with a best fit fractional error of  $\ln f = -3.4$ . No significant covariance was found between the baseline flux density parameters and the peak frequency or peak flux density.

[147]: Barniol Duran et al. (2013), “Radius Constraints and Minimal Equipartition Energy of Relativistically Moving Synchrotron Sources”

Given the known distance to the source, and under particular assumptions about the source geometry, physical properties of the synchrotron-emitting region can be inferred from these data [147]. The emission was modelled with a conical geometry as expected for outflows (e.g., jets or winds) that are launched from—and collimated by—the inner parts of flared accretion disks that emit close to the Eddington limit. However these values depend critically upon assumed values for the so-called *microphysical parameters* ( $\epsilon_e, \epsilon_B$ ), where  $\epsilon_e$  and  $\epsilon_B$  respectively quantify the fraction of total energy carried by electrons and magnetic fields. The derived values also depend on the electron power-law index, so the uncertainty on  $p$  was propagated.

One common assumption for such calculations is to assume *equipartition*, where it is assumed that the system contains only electrons and magnetic fields. This yields a robust lower limit outflow energy, reached where  $\epsilon_e/\epsilon_B = 11/6$  [147], with any deviation from equipartition resulting in a higher total outflow energy. For the geometry of the outflow, the default model was two conical emitting regions with half-opening angles  $\phi = 30^\circ$ . However, it should be noted that the opening angle for the outflow is largely unconstrained. The inferred equipartition properties of the source for  $\phi = 30^\circ$  are given in the Table 4.2 for each epoch, alongside the corresponding values that would be derived for a spherical outflow.

Though the equipartition case provides a useful lower limit, it remains unrealistic as a central estimate because it neglects any contribution to

	$\Delta t$ (days)	equipartition: $\epsilon_e/\epsilon_B = 11/6$ (no protons)			
		$R_{\text{eq}}$ (cm)	$E_{\text{eq}}$ (erg)	$B_{\text{eq}}$ (G)	$n_{e,\text{eq}}$ ( $\text{cm}^{-3}$ )
Conical $(\phi = 30^\circ)$	42	16.29(0.02)	47.9(0.1)	-0.27(0.05)	3.5(0.1)
	70	16.47(0.02)	48.3(0.1)	-0.36(0.04)	3.3(0.1)
	120	16.68(0.02)	48.7(0.1)	-0.49(0.04)	3.0(0.1)
	178	16.93(0.02)	48.9(0.1)	-0.73(0.05)	2.6(0.1)
Spherical	42	15.92(0.02)	47.4(0.1)	-0.00(0.04)	4.0(0.1)
	70	16.10(0.02)	47.8(0.1)	-0.10(0.04)	3.8(0.1)
	120	16.31(0.02)	48.2(0.1)	-0.22(0.04)	3.6(0.1)
	178	16.56(0.02)	48.4(0.1)	-0.47(0.04)	3.1(0.1)

	$\Delta t$ (days)	proton model: $\epsilon_e = 0.1; \epsilon_B = 10^{-3}$			
		$R$ (cm)	$E$ (erg)	$B$ (G)	$n_e$ ( $\text{cm}^{-3}$ )
Conical $(\phi = 30^\circ)$	42	16.18(0.03)	49.4(0.1)	-0.68(0.05)	4.4(0.1)
	70	16.37(0.02)	49.7(0.1)	-0.78(0.04)	4.2(0.1)
	120	16.57(0.02)	50.1(0.1)	-0.91(0.04)	3.9(0.1)
	178	16.82(0.02)	50.3(0.1)	-1.16(0.04)	3.4(0.1)
Spherical	42	15.81(0.03)	48.8(0.1)	-0.41(0.04)	4.9(0.1)
	70	16.00(0.02)	49.2(0.1)	-0.52(0.04)	4.7(0.1)
	120	16.20(0.02)	49.6(0.1)	-0.65(0.04)	4.4(0.1)
	178	16.45(0.02)	49.8(0.1)	-0.89(0.04)	3.9(0.1)

outflow energy from protons. While our radio observations primarily probe electron emission, electrons are generally accelerated with much lower efficiency than protons in astrophysical accelerators [148], so it is reasonable to assume that protons will actually carry a significant portion of energy. Motivated by observations of GRB afterglows [149, 150], supernovae [151] and the relativistic TDE Swift J1644+57 [152], values of  $\epsilon_e = 0.1$  and  $\epsilon_B = 10^{-3}$  were assumed. The total estimated outflow energy, and other inferred properties for these assumptions, are given in Table 4.3. These inferred energies are, as expected, substantially larger than for the equipartition case.

The results in Table 4.3 revealed a third distinct spectral component, namely synchrotron emission from an extended synchrotron-emitting outflow. For a half-opening angle,  $\phi$ , of  $30^\circ$  a radius of  $R = 1.5 \times 10^{16}$  cm was found for the first epoch (41 days after discovery), increasing to  $R = 7 \times 10^{16}$  cm shortly after the neutrino detection (177 days after discovery). These values are substantially larger than the inferred blackbody radii from UV/optical/X-ray observations, indicating a separate emission zone for the synchrotron radiation. The implied expansion velocity of the outflow is roughly constant at  $v/c = \dot{R}/c = 0.12 \pm 0.01$  during the first three epochs, with a significant ( $> 3\sigma$ ) acceleration to  $v/c = 0.21 \pm 0.02$  for the last epoch. These are the expansion velocities of the synchrotron-emitting region itself, so provide a lower limit to the velocity at the base of the outflow. Indeed even the hotspots of relativistic jets from active galaxies that are frustrated by gas in their host galaxy are typically observed to have subrelativistic expansion velocities of  $\sim 0.1c$  [153].

The inferred outflow energy,  $E$ , shows a linear increase from  $2.5 \times 10^{49}$  erg to  $2 \times 10^{50}$  erg (Figure 4.7), which would not be expected from models of TDE radio emission which involve a single injection of energy [154, 155]. The constant increase of energy implies a constant injection rate

Table 4.2: Summary of the synchrotron modelling for the *equipartition case*. All inferred properties are given in  $\log_{10}$  scale, with errors given in brackets.

Table 4.3: Summary of the synchrotron modelling with the inclusion of protons. All inferred properties are given in  $\log_{10}$  scale, with errors given in brackets.

[148]: Morlino et al. (2012), “Strong evidence for hadron acceleration in Tycho’s supernova remnant”

[149]: Granot et al. (2014), “Gamma-Ray Burst Jets and their Radio Observations”

[150]: Fong et al. (2015), “A Decade of Short-duration Gamma-Ray Burst Broadband Afterglows: Energetics, Circumburst Densities, and Jet Opening Angles”

[151]: Horesh et al. (2013), “An early and comprehensive millimetre and centimetre wave and X-ray study of SN 2011dh: a non-equipartition blast wave expanding into a massive stellar wind”

[152]: Eftekhari et al. (2018), “Radio Monitoring of the Tidal Disruption Event Swift J164449.3+573451. III. Late-time Jet Energetics and a Deviation from Equipartition”

[153]: Polatidis et al. (2003), “Proper Motions in Compact Symmetric Objects”

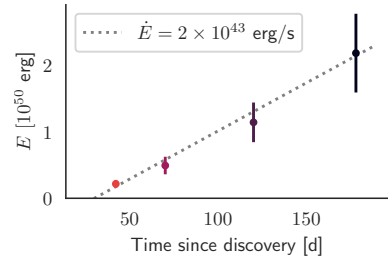
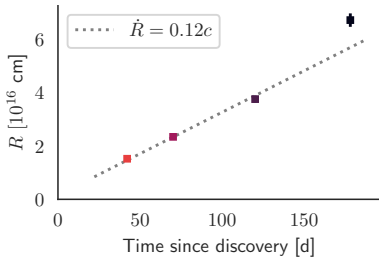


Figure 4.7: Inferred energy of the synchrotron-emitting outflow of AT2109dsg.



**Figure 4.8:** Inferred radius of the synchrotron-emitting outflow of AT2019dsg.

[154]: Alexander et al. (2016), “Discovery of an Outflow from Radio Observations of the Tidal Disruption Event ASASSN-14li”  
[155]: Krolik et al. (2016), “ASASSN-14li: A Model Tidal Disruption Event”

[156]: Pasham et al. (2018), “Discovery of a Time Lag between the Soft X-Ray and Radio Emission of the Tidal Disruption Flare ASASSN-14li: Evidence for Linear Disk-Jet Coupling”

[156]: Pasham et al. (2018), “Discovery of a Time Lag between the Soft X-Ray and Radio Emission of the Tidal Disruption Flare ASASSN-14li: Evidence for Linear Disk-Jet Coupling”

[157]: Atwood et al. (2009), “The Large Area Telescope on the Fermi Gamma-Ray Space Telescope Mission”

[158]: Garrappa et al. (2019), “Fermi-LAT Gamma-ray Observations of IceCube-191001A”

[159]: The Fermi-LAT collaboration (2019), “Fermi Large Area Telescope Fourth Source Catalog”

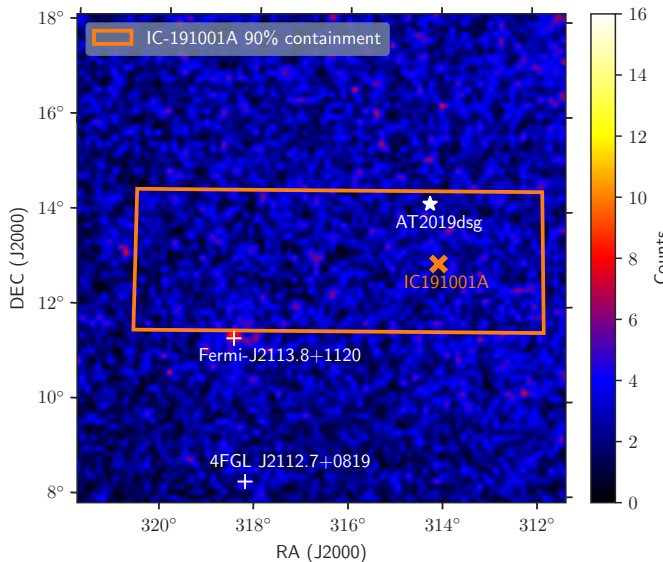
at the base of the outflow, of approximately  $2 \times 10^{43} \text{ erg s}^{-1}$ . While some scenarios can yield an increase in inferred energy from a single energy injection, none of these are consistent with the full set of observed properties. First, a single ejection with a range of velocities could explain the observed linear increase of energy with time (the slower ejecta arrive later), but is incompatible with the increasing velocity. Second, an increase of the efficiency for conversion of Poynting luminosity to relativistic particles is unlikely because the target density that is available to establish this conversion is decreasing. And finally, an apparent increase of the inferred energy due to an increase of solid angle that emits to our line of sight is only expected for relativistic outflows that decelerate. Instead, for AT2019dsg, the observations suggest the presence of a central engine that yields continuous energy injection through a coupling of accretion power to the radio emission [156], with acceleration in the final radio epoch due to a decrease in the slope of the ambient matter density profile.

There is, however, no evidence of correlation between the X-ray and radio emission in AT2019dsg. This is in contrast to coupling found for TDE ASASSN-14li [156]. Such a correlation would only be expected if the X-ray luminosity of AT2019dsg served as a tracer of disk power, but the rapid observed fading indicates that the observed X-ray emission in AT2019dsg is instead driven either by varying obscuration or temperature evolution.

## Gamma-Ray Observations

Gamma-ray observations were provided by the *Fermi* Large Area Telescope (*Fermi*-LAT) [157], sensitive to gamma rays with energies from 20 MeV to greater than 300 GeV. During its sky-survey operations, the pair-conversion telescope *Fermi*-LAT scans the entire sky every three hours, and can monitor the variable gamma-ray sky over short and long timescales. A search was performed within the 90% error region during both the 1-day and 1-month period prior to the arrival of the high-energy neutrino, as part of a systematic LAT realtime neutrino follow-up program [158]. No new gamma-ray source was identified, and there was no significant ( $\geq 5\sigma$ ) detection for any source from the fourth *Fermi*-LAT point source catalog (4FGL [159]).

Following the identification of AT2019dsg as a candidate neutrino source, a dedicated point-source analysis centred on the object was then performed over three different time intervals under the assumption of a power-law spectrum. The duration of each interval was motivated by the multi-wavelength behaviour of the source. The first interval (G1) includes 130 days of observations that include the peak of the optical emission from 2019 April 4 to 2019 August 12. The second (G2) spans from 2019 August 12 to 2019 November 20 and covers the apparent UV plateau and the peak of the radio emission. The third interval (G3) integrates the whole period between the start of G1 up to 2020 January 31. No significant emission was found, as can be seen in Figure 4.9. Upper limits were accordingly derived for the energy flux (integrated over the whole analysis energy range) have been derived for a power-law spectrum ( $dN/dE \propto E^{-\Gamma}$ ) with photon power-law index  $\Gamma = 2$  and are listed in Table 4.4, along with the respective time intervals.



Interval	MJD Start	MJD Stop	UL (erg cm <sup>-2</sup> s <sup>-1</sup> )
G1	58577	58707	$2.6 \times 10^{-12}$
G2	58707	58807	$1.2 \times 10^{-11}$
G3	58577	58879	$2.0 \times 10^{-12}$

In all three time intervals, a new non-catalogued gamma-ray emitter was detected in the RoI at a significance  $\geq 5\sigma$ . This source lies just outside the IC191001A 90% error region, as indicated in Figure 4.9. The source, labelled *Fermi*-J2113.8+1120, is likely the gamma-ray counterpart of the radio-loud object GB6 J2113+1121, classified as a flat-spectrum radio quasar with redshift  $z = 1.63$  [160]. The detection of an unrelated gamma-ray blazar within the neutrino uncertainty area is consistent with the background estimation. On average 1.5 4FGL gamma-ray blazars are expected in 20 sq. deg. A lightcurve analysis, shown in Figure 4.10, reveals that the source was last detected in gamma rays one month prior to the IC191001A detection, and was not significantly detected again until another month after the neutrino detection. This is compatible with the findings of the realtime follow-up of the region [158]. Such a long apparent lag between gamma-ray emission and neutrino emission is disfavoured by recent studies on the temporal behavior of hadronic processes in blazars [161, 162], suggesting that the blazar is unlikely to have produced the neutrino. There is thus no obvious connection between the gamma-ray observations of *Fermi*-J2113.8+1120 and IC191001A.

The HAWC observatory also reported a search for transient gamma-ray emission on short timescales in the localisation of IC191001A [163], and set an upper limit for their most significant position at 95% confidence of  $E^2 dN/dE = 3.51 \times 10^{-13} (E/\text{TeV})^{-0.3} \text{ TeV cm}^{-2} \text{ s}^{-1}$ , in the energy range 300 GeV to 100 TeV, for the period from 2019 September 30 05:46:52 UTC to 2019 October 02 06:03:29 UTC. We note that this search covered a relatively large region of the sky, and thus had a large associated trial factor. A dedicated search at the position of AT2019dsg would be more

**Figure 4.9:** LAT counts map of the Region Of Interest (ROI) in the integrated search period G3, showing the IC191001A 90% localisation region in orange. The neutrino best-fit position is marked with a orange ‘x’.

**Table 4.4:** Gamma-ray energy flux upper-limits for a point-source with power-law index  $\Gamma=2.0$  at the position of AT2019dsg integrated over the analysis energy range 0.1-800 GeV.

[160]: Pursimo et al. (2013), “The Micro-Arcsecond Scintillation-Induced Variability (MASIV) Survey. III. Optical Identifications and New Redshifts”

[161]: Diltz et al. (2015), “Time Dependent Hadronic Modeling of Flat Spectrum Radio Quasars”

[162]: Gao et al. (2019), “Modelling the coincident observation of a high-energy neutrino and a bright blazar flare”

[163]: Ayala (2019), “IceCube-191001A: HAWC follow-up”

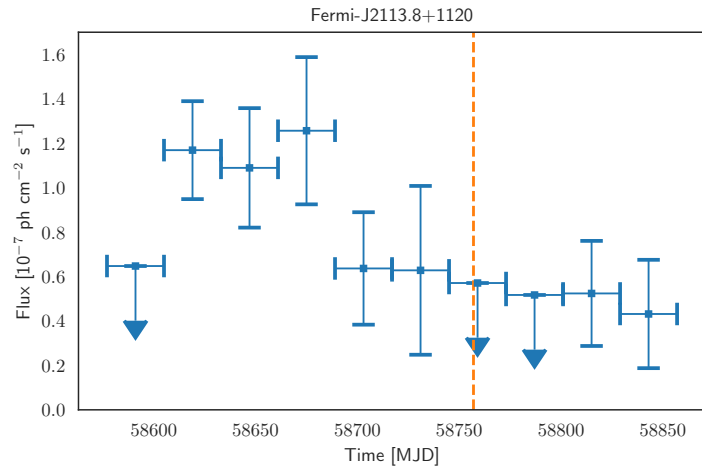


**Figure 4.10:** LAT lightcurve for the source *Fermi*-J2113.8+1120 in the time interval G3, with evenly spaced binning of 28 days. Vertical error bars represent  $1\sigma$  intervals, horizontal bars denote bin width.  $2\sigma$  upper limits are shown for bins with  $TS \leq 9$ . The orange dashed vertical line marks the arrival time of IC-191001A.

sensitive, especially one that additionally targeted the longer period over which the central engine is active.

## Spectroscopy

[164]: Nicholl et al. (2019), “ePESSTO+ classification of optical transients”

[165]: Miller et al. (1993), *Lick Obs. Tech. Rep.* 66

[166]: Oke et al. (1995), “The Keck Low-Resolution Imaging Spectrometer”

AT2019dsg was first classified as a TDE by ePESSTO+ on 2019 May 13 [164], and the redshift of AT2019dsg was measured to be  $z = 0.051$ . This implies a luminosity distance  $D \approx 230$  Mpc assuming a flat cosmology with  $\Omega_\Lambda = 0.7$  and  $H_0 = 70$  km s<sup>-1</sup> Mpc<sup>-1</sup>. Further high-resolution spectroscopic observations were conducted using the De Veny Spectrograph on the 4.3m Lowell Discovery Telescope (LDT), the Kast Double Spectrograph on the 3m Lick Observatory Shane Telescope (Lick) [165], and the Low Resolution Imaging Spectrograph on the 10m Keck Telescope (Keck) [166], with the most recent spectrum on 2019 September 25. These spectra confirmed that AT2019dsg belonged to the common spectroscopic class of TDEs with Bowen fluorescence emission lines and broad H $\alpha$  emission lines [59].

Following the identification of AT2019dsg as a candidate neutrino source, additional high-resolution spectra of the source were taken with the 200in Hale Telescope Double Spectrograph at Palomar Observatory (P200) on 2019 October 3 and again with Lick on 2019 October 5 and 2019 October 29. As seen in Figure 4.11, there is no evidence of any significant spectral evolution between these spectra and the most recent pre-neutrino spectrum from 2019 September 25, and the spectral evolution of AT2019dsg is consistent with that of other TDEs [59].

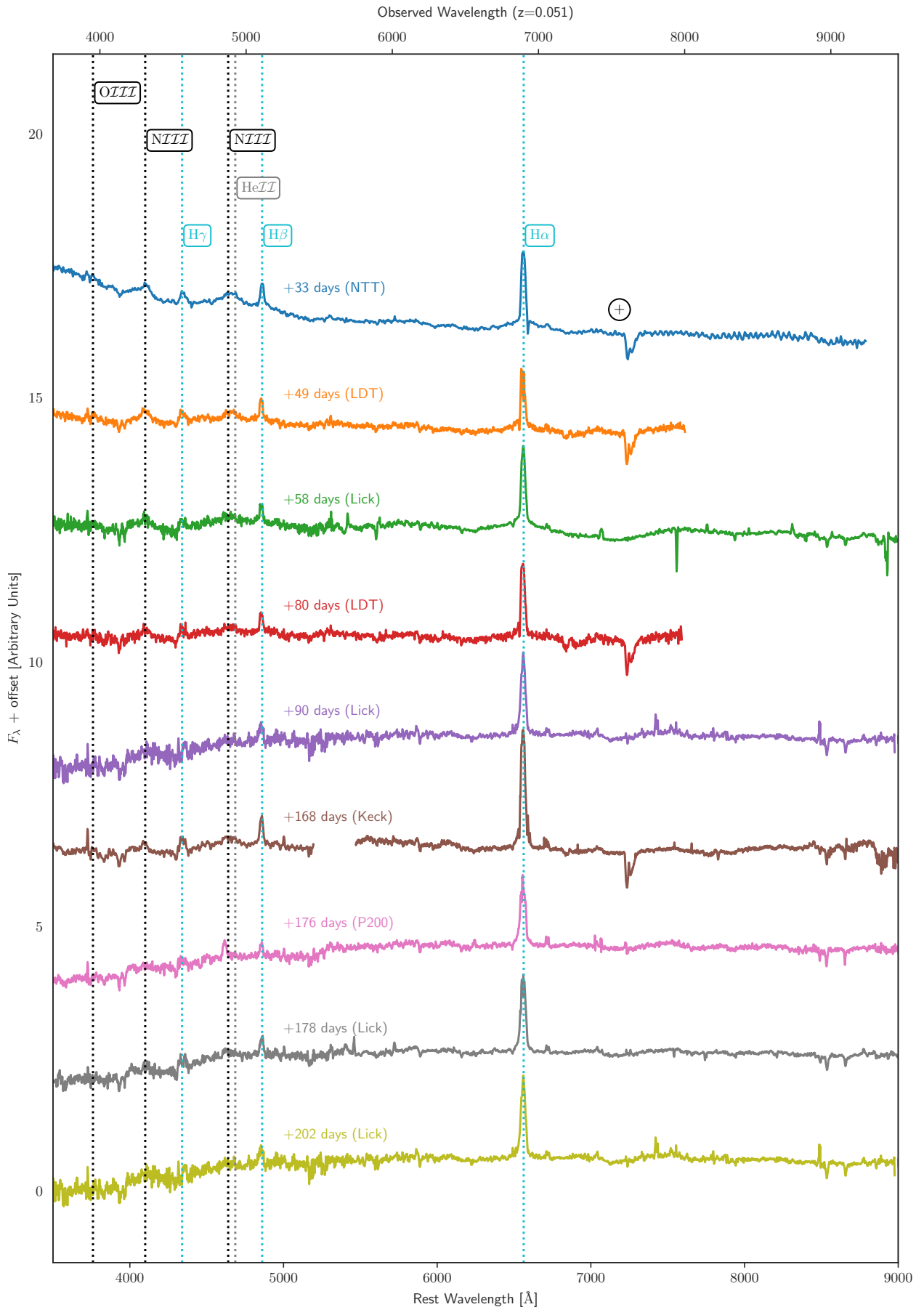


**Figure 4.11:** The spectroscopic evolution of AT2109dsg, beginning with the publicly available classification spectrum taken with the NTT [164], and further spectra from LDT, Lick, Keck and P200. The Balmer lines are highlighted in cyan, the HeII lines in gray, and the Bowen fluorescence lines (OIII at 3760Å, NIII at 4100Å and 4640Å) in black. Telluric lines are marked with +.

## 4.2 Probability of Chance Coincidence

One key question for the neutrino-TDE association is whether the observed coincidence is likely to have arisen merely by random chance. During the first 18 months of survey operations, ZTF identified 17 TDEs [59], distributed over 28000 deg of observed sky (the ZTF survey footprint, after removing sources with a Galactic latitude  $|b| < 7$ ). Of these TDEs, each was typically detected for  $\sim 6$  months[59]. The density of ZTF-detected TDEs can thus be estimated as approximately  $2.0 \times 10^{-4}$  per sq. deg. of sky in the survey footprint at any given time. Our follow-up pipeline requires that any candidate be detected by ZTF in ToO observations following a neutrino, in order to establish temporal coincidence. We assume that our neutrino pipeline does not have a significantly higher selection efficiency than the dedicated ZTF program to identify TDEs [59], and thus that the latter provides a reasonable estimate on the background rate of TDEs passing our pipeline.

Those TDEs with radio detections are considered the most promising candidates for neutrino production, as the radio emission serves as a tracer for the particle acceleration required in neutrino sources. We can consider the fraction of TDEs which would additionally be detected in radio, assuming that all could be observed. Among the ZTF sample of confirmed TDEs, radio follow-up observations were undertaken with the VLA for 6, of which 2 were detected. Taking this implied radio-emitting fraction of 33%, we find a final density of  $5.9 \times 10^{-5}$  radio-emitting TDEs per sq. deg. of surveyed sky.

ZTF has followed-up eight neutrinos up to January 2020, and has covered a combined localisation region of 81.05 sq. deg (see Table ??). With this sky area, the expected number of coincident radio-detected TDEs across all of our neutrino follow-up campaigns is  $4.8 \times 10^{-3}$ . The Poisson probability of observing at least one radio-emitting TDE during our entire neutrino follow-up campaign is thus  $4.8 \times 10^{-3}$ .

As radio follow-up observations of ZTF TDEs were biased towards those most likely to be detectable, this estimate is an overly conservative one. Because the bolometric energy flux derived from UV/optical observations (i.e., the blackbody luminosity over the square of the distance) serves as a proxy for the non-thermal emission, TDEs which were bright under this metric were preferentially selected for radio observations. To avoid this selection bias, we can instead directly use this bolometric energy flux as a proxy for neutrino flux to identify the most promising candidates for neutrino detection, namely those TDEs which are both nearby and luminous. Of the 17 TDEs observed by ZTF, AT2019dsg ranks second in this metric. The probability of finding a TDE in our neutrino follow-up campaign with a bolometric energy flux that is at least as high as AT2019dsg is thus  $1.9 \times 10^{-3}$ .

[85]: IceCube Collaboration et al. (2018), “Multimessenger observations of a flaring blazar coincident with high-energy neutrino IceCube-170922A”

[95]: Aartsen et al. (2020), “Time-Integrated Neutrino Source Searches with 10 Years of IceCube Data”

[167]: Graham et al. (2019), “The Zwicky Transient Facility: Science Objectives”

Like most other studies in neutrino astronomy [85, 95], these chance coincidence probability estimates do not account for the so-called “look-elsewhere effect” from multiple possible hypotheses. In our case, the ZTF program has sensitivity to four theoretically-motivated neutrino population hypotheses (TDEs, core-collapse supernovae, gamma-ray bursts and AGN flares) [167]. The impact of the testing multiple hypotheses is thus

modest, and a chance coincidence explanation for AT2019dsg-IC191001A remains unlikely.

Of these four, it should also be noted that TDEs are the one to which our program is most sensitive. As introduced in Chapter 2, follow-up programs are generally most effective in identifying neutrino emission from TDEs, since this flux should be dominated by nearby sources which can be detected by telescopes such as ZTF. Moreover, given their low rate, any individual TDE-neutrino association will be easier to identify than for more abundant populations such as AGN or supernovae. TDEs also evolve sufficiently slowly to enable extensive photometric and spectroscopic follow-up, in marked contrast to fast transients such as GRB afterglows, leading to a higher detection efficiency.

While an atmospheric origin for the IC191001A-AT2019dsg association cannot be excluded, the improbability of chance temporal and spatial coincidence substantially reinforces the independent energy-based evidence of an astrophysical origin for IC191001A, and indicates that any atmospheric origin is unlikely.

### 4.3 Neutrino production in AT2019dsg

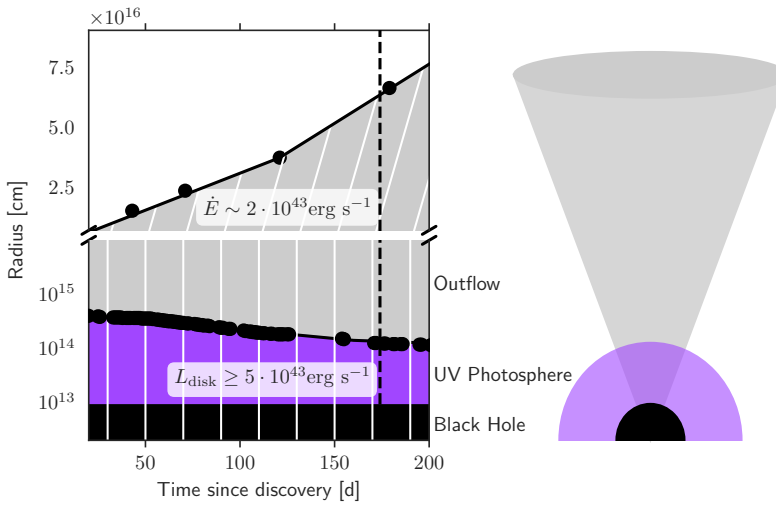


**Figure 4.12:** Left: temporal evolution of the three emission zones for AT2019dsg. Right: Illustration of the geometry of these three zones.

Given that an atmospheric origin for IC191001A is unlikely, we can instead consider whether it is realistic for AT2019dsg to be the source of neutrino IC191001A. There are several requirements that an object must satisfy to be a neutrino source. In particular, neutrino production requires hadrons to be accelerated to sufficiently high energies, and to collide with a suitably abundant target. As demonstrated in Section 4.1, there is strong evidence derived purely from multi-wavelength observations for the existence of three distinct emission zones in AT2019dsg, illustrated in Figure 4.12.

Radio observations confirm that particle acceleration is indeed occurring, and that this continues without decline through to the detection of the neutrino at  $\sim 180$  days post-discovery. Given that neutrinos typically take a fraction  $\eta_{pv} \sim 0.05$  of the parent proton energy, our accelerator must be capable of accelerating protons to at least 4 PeV. We evaluate the Hillas

[168]: Hillas (1984), “The Origin of Ultra-High-Energy Cosmic Rays”

criterion [168] introduced in Equation ?? of Chapter ??, that the proton Larmor radius be less than the system size, to determine whether this is possible:

$$\frac{E_{\max}}{\text{PeV}} \approx 1600 \times \frac{B}{\text{Gauss}} \times \frac{R}{10^{16} \text{ cm}} \times \beta Z \quad (4.3)$$

We use our estimates for conditions in the synchrotron zone at the time of neutrino detection, with  $B \sim 0.07$  G and  $R \sim 7 \times 10^{16}$  cm for the near-contemporaneous radio epoch. Taking this as a baseline, we find a maximum proton energy of  $\sim 160$  PeV, far in excess of our requirements. The Hillas criterion can also be satisfied within the engine that powers the radio-emitting outflow because the product  $BR$  is not expected to decrease at smaller radii (e.g.  $B \propto R^{-1}$  for a toroidal configuration).

In order for particle acceleration to occur up to these energies, the timescale required for particle acceleration must also be shorter than the associated particle cooling timescale. Previous work has found this condition can be satisfied in TDEs for relevant energies [169, 170], although a detailed calculation is beyond the scope of this thesis.

Assuming that protons are indeed accelerated to sufficient energies, these must then collide with a suitably abundant target. For neutrino production, this can be either photons ( $p\gamma$  interactions) or protons ( $p p$  interactions). For a photon target, neutrino production occurs above an energy determined by the mass of the  $\Delta$  resonance. This threshold, as introduced in Equation ?? of Chapter ??, can be approximated as:

$$E_\gamma E_p \sim \Gamma^2 0.16 \text{ GeV}^2 \quad (4.4)$$

Substituting  $E_\nu = \eta_{p\nu} E_p$  where again  $\eta_{p\nu} \sim 0.05$  and  $E_\nu$  is the energy of a single neutrino, this can then be translated into a threshold photon energy:

$$\frac{E_\gamma}{\text{eV}} \gtrsim \left(\frac{\Gamma}{1}\right)^2 \left(\frac{\eta_{p\nu}}{0.05}\right) \left(\frac{8 \text{ PeV}}{E_\nu}\right) \quad (4.5)$$

With this constraint, we can derive the necessary photon energies required for a target to produce IC191001A. Taking the reconstructed neutrino energy of  $\sim 0.2$  PeV directly, we find a threshold photon target of  $E_\gamma \gtrsim 40$  eV. However, these reconstructed neutrino energies typically have upper bounds an order of magnitude or more above the central estimate [85], so the true neutrino energy could be substantially higher. For example, with a true neutrino energy of  $\sim 1$  PeV, we would instead require photons  $E_\gamma \gtrsim 8$  eV for pion production. In principle, this suggests that both UV and X-ray photons would be suitable targets.

We can then consider whether these photons are suitably abundant for efficient pion production. We can derive the mean free path,  $\lambda$ , for a proton:

$$\lambda = \frac{1}{\sigma_{p\gamma} n_\gamma} \quad (4.6)$$

[85]: IceCube Collaboration et al. (2018), “Multimessenger observations of a flaring blazar coincident with high-energy neutrino IceCube-170922A”

with cross section  $\sigma_{p\gamma} \sim 5 \times 10^{-28} \text{ cm}^2$  and photon number density  $n_\gamma$ . For the UV photosphere with a blackbody of temperature  $T_{BB} \sim 10^{4.6} \text{ K}$ , the mean free path for the parent proton of a 1 PeV neutrino is  $\lambda \sim 2 \times 10^{13} \text{ cm}$ . Accounting for the fact that each proton interaction will lead to a typical energy reduction of 20%, we then find:

$$f_\pi(x) = 1 - e^{\left(\frac{-0.2x}{\lambda}\right)} \quad (4.7)$$

for path  $x$ , where  $f_\pi \leq 1$  is the conversion efficiency from total energy in protons,  $\epsilon_p$ , to total energy in pions,  $\epsilon_\pi$ , such that  $\epsilon_\pi = f_\pi \epsilon_p$ . Equating  $x$  with the radius of the UV photosphere  $x \approx 10^{14.6} \text{ cm}$ , we then find that each proton or neutron will typically undergo  $\sim 10$  interactions, which would represent a high efficiency  $f_\pi \sim 0.9$ , so the UV photosphere is indeed optically thick. At smaller radii, the X-rays would overtake the UV photons as dominant scattering targets. We caution that this estimate is only approximate, and that detailed numerical simulations are required to accurately calculate the pion production efficiency [171].

It is however clear that conditions in AT2019dsg are sufficient for pion production to occur. A further requirement for the association is that there are sufficient neutrinos produced at the source for the detection of one high-energy neutrino like IC191001A to occur. During pion production roughly half of the energy will be lost through the neutrino-less  $\pi^0$  channel [171], while for the charged pion channel energy is shared roughly equally among the decay products  $\pi^\pm \rightarrow e^\pm + \bar{\nu}_e + \bar{\nu}_\mu + \nu_\mu$  [172]. Thus  $\sim 3/8$  of the pion energy is transferred to neutrinos, with a 1:2:0 flavour composition at source. However, as introduced in Chapter ??, neutrino oscillations across the cosmological baseline travelled will lead to a mixed 1:1:1 composition on Earth. The IceCube realtime event selection is dominated by muon neutrinos, a channel which will then carry no more than  $\sim 1/8$  of the pionic energy. Thus we find:

$$\epsilon_\nu \approx f_\pi \frac{\epsilon_p}{8} \quad (4.8)$$

where  $\epsilon_\nu$  is the total energy carried by muon neutrinos. We can calculate the effective area for a single high-energy neutrino. Below 1 PeV, this corresponds to an approximately-constant threshold of  $6 \times 10^{-4} \text{ erg cm}^{-2}$  for an expectation of one neutrino alert. Given the redshift of AT2019dsg, we find a required total energy in neutrinos  $\epsilon_\nu \approx 4 \times 10^{51} \text{ erg}$  to produce a single neutrino alert. Approximating the sharply-peaked  $p\gamma$  neutrino spectrum as a monoenergetic flux anywhere between  $0.2 \text{ PeV} \lesssim E_{nu} \lesssim 1 \text{ PeV}$ , we can use Equation 4.8 to express the expected number of detected neutrinos as:

$$N_\nu \approx \left( \frac{\epsilon_\nu}{E_\nu} \right) \left( \frac{A_{\text{eff}}}{4\pi D_L^2} \right) \approx 3 \times \frac{f_{pi}}{0.9} \times \frac{\epsilon_p}{10^{53} \text{ erg}} \quad (4.9)$$

This expectation would also be valid for any power-law distribution in the same energy range, assuming a similarly high pion conversion efficiency  $f_\pi$ . To obtain the expected number of neutrino alerts from this source we have to estimate the energy carried by protons ( $E_p$ ) that are accelerated above the energy threshold needed to produce high-energy neutrinos. The outflow energy of  $2 \times 10^{50} \text{ erg}$  derived from the radio

[171]: Hümmer et al. (2010), “Simplified Models for Photohadronic Interactions in Cosmic Accelerators”

[172]: Waxman et al. (1999), “High energy neutrinos from astrophysical sources: An upper bound”

observations (Table 4.3) represent a lower bound to the energy that is available for particle acceleration in a central engine. Indeed, the total energy budget for a TDE is set by the mass of the disrupted star, with  $\epsilon_{\text{TDE}} \sim (1/2) 0.1 M_{\odot} c^2 \sim 10^{53}$  erg for a solar-mass star. We will assume 1% of this total energy budget is carried by relativistic protons,  $\epsilon_p \sim 10^{51}$  erg. We then find  $N_{\nu} \approx 0.03$ , a number that remains less than unity for any reasonable assumption of  $\epsilon_p$ .

However, this is not necessarily in tension with the IC191001A-AT2019dsg association, because the detection of a single high energy neutrino does not imply that a single source must have a neutrino alert expectation of  $\sim 1$  [90]. Rather, after accounting for Poisson counting uncertainty, the detection of a single high-energy neutrino such as IC191001A implies a mean expectation in the range  $0.05 < N_{\nu,\text{tot}} < 4.74$  at 90% confidence where  $N_{\nu,\text{tot}}$  is the cumulative neutrino expectation for all TDEs that ZTF has observed. For an individual TDE the expectation will then be significantly lower. AT2019dsg emits  $f_{\text{bol}} \sim 0.16$  of the population bolometric energy flux, and if we take this as a proxy for neutrino emission, we would expect  $0.008 \lesssim N_{\nu} \lesssim 0.76$  for this source assuming that conditions are similar in other ZTF TDEs. In that case, any optically-thick py scenario would be sufficient for AT2019dsg to produce IC191001A.

In the multi-zone model, shown in Figure 4.12, the thermal photons thus provide a guaranteed target for pion production. However hadrons could in principle also serve as a target, leading us to consider a single-zone scenario in which the protons are accelerated at the same location as the synchrotron-emitting electrons, with the neutrino spectrum following the same intrinsic energy power law as the protons and electrons. For pp neutrino production, high target densities of  $n_p \sim 1/(\sigma_{pp} R) \sim 10^8 \text{ cm}^{-3}$  would be required for efficient production of pions, where  $\sigma_{pp}$  is the proton-proton cross section and  $R \sim 10^{17} \text{ cm}$  is the characteristic size of the synchrotron-emitting region at the time of neutrino production. The synchrotron analysis provides an estimate of the number density of relativistic electrons, which in turn yields a lower limit to the total particle density in the radio region. For the energy and radius of last radio epoch, which was obtained a few days after the neutrino detection, we find an electron number density of  $10^{3.4 \pm 0.1} \text{ cm}^{-3}$  (see Table 4.3). It is expected that the proton number density should be higher, owing again to the more efficient acceleration of protons than electrons [148], but the exact value is largely unconstrained.

The high required proton density could in principle be provided by the unbound stellar debris from the tidal disruption itself, although this component moves with a typical maximum velocity of  $0.05 c$  [155], so the majority of this debris would need to have been swept up with the outflow. Alternatively, the density could be provided by pre-existing gas in the galaxy core, though it would be challenging to avoid accompanying signatures of pre-TDE accretion. More critically, in contrast to a peaked py neutrino spectrum, for pp production the neutrinos would instead follow a power law. Many of these neutrinos would then fall below the threshold of IceCube's alert selection, resulting in a lower  $N_{\nu}$ .

Following the publication of the coincidence, multiple theoretical works have independently suggested possible models for neutrino production in AT2019dsg. Motivated by the unusual X-ray-bright nature of the source

[90]: Strotjohann et al. (2019), “Eddington bias for cosmic neutrino sources”

[155]: Krolik et al. (2016), “ASASSN-14li: A Model Tidal Disruption Event”

at early times, one suggested mechanism for the association is an obscured relativistic jet in AT2019dsg [173]. In that scenario, the X-ray emission is assumed to continue at late times, providing target photons. Ultimately an  $N_\nu \approx 0.05$  was calculated, which would again be compatible with the observed association. An alternative explanation invoked a relativistic jet that was viewed somewhat off-axis (10-30°) for which optical/UV photons instead serve as a target [174]. Such a model can produce  $N_\nu \gtrsim 0.01$  without violating the gamma-ray constraints introduced in Section 4.1, providing another viable explanation. A third suggested explanation did not invoke a relativistic jet, instead favouring an AGN-like corona model for neutrino production with proton acceleration through plasma turbulence or magnetic reconnection [175]. Under optimistic assumptions such a scenario would be a possible explanation, yielding a sufficient  $N_\nu \approx 0.01$ .

Given these many different possible neutrino spectrum expectations, a search for accompanying lower-energy neutrinos could be used to probe the conditions at the site of proton interaction. As reported in Chapter 3, such a search was conducted as part of this thesis for an older sample of TDEs, but no such IceCube analysis has yet been performed for AT2019dsg.

An analysis was published by the ANTARES collaboration, and did not find any significant excess of neutrino emission from AT2019dsg [176]. A time-integrated search was performed from the date of ZTF TDE discovery, 2019 April 9, up to 2020 February 29. A muon neutrino upper limit was set of  $1.0 \times 10^{-7}$  GeV $^{-1}$  cm $^{-2}$  s $^{-1}$  for an E $^{-2}$  spectrum in the range 4 TeV - 4 PeV, corresponding to a fluence upper limit of 19 GeV cm $^{-2}$  or 0.03 erg cm $^{-2}$ . For such an E $^{-2}$  power law, the energy is distributed:

$$\frac{dN_\nu}{dE} = \phi_0 \left( \frac{E}{E_0} \right)^2 \quad (4.10)$$

$$\epsilon_\nu = \int_{E_{min}}^{E_{max}} E \frac{dN_\nu}{dE} dE = \phi_0 E_0^2 (\ln(E_{max}) - \ln(E_{min})) \quad (4.11)$$

The neutrino energy range of 0.2-1 PeV to which IceCube alerts are most sensitive to should carry 23% of the total energy in this range for an E $^{-2}$  power law, corresponding to a fluence of  $7 \times 10^{-3}$  erg cm $^{-2}$ . This limit is then a full order of magnitude greater than the flux required to produce a single high-energy neutrino alert in this energy range in IceCube, and far in excess of all reasonable predictions for neutrino emission in AT2019dsg. The ANTARES non-detection is thus not constraining for the scenarios outlined above, and not in tension with an association between IC191001A and AT2019dsg.

## 4.4 Compatibility with stacking limit

We can further estimate the contribution of TDEs to the diffuse neutrino flux that would be required to produce an observation of one association with our ZTF follow-up program. As outlined in Table ??, a total of eight neutrino alerts were observed through to January 2020. For all but one of

[173]: Winter et al. (2021), “A concordance scenario for the observed neutrino from a tidal disruption event”

[174]: Liu et al. (2020), “Neutrino emission from an off-axis jet driven by the tidal disruption event AT2019dsg”

[175]: Murase et al. (2020), “High-energy Neutrino and Gamma-Ray Emission from Tidal Disruption Events”

[176]: ANTARES Collaboration et al. (2021), “Search for neutrinos from the tidal disruption events AT2019dsg and AT2019fdr with the ANTARES telescope”

these, IceCube reported an estimate of the *signalness*, i.e., the probability for each to be astrophysical. It should be noted that this quantity is not an absolute value, but is rather derived under specific assumptions about the underlying neutrino source population. Nonetheless, if these estimates are taken at face value, and it is assumed that the additional event had the a signalness equal to the mean of reported events (0.5), we would expect a total of  $\sim 4.3$  astrophysical neutrinos in our sample. Taking the implied ZTF population expectation of  $0.05 < N_{\nu,\text{tot}} < 4.74$ , we would then require that a fraction  $0.01 < f < 1.00$  of the astrophysical neutrino flux was produced by ZTF-detected TDEs at 90% confidence.

We can further consider the contribution of those TDEs that ZTF has not detected following the procedure in Chapter ??, to estimate the cumulative contribution of all TDEs to the diffuse neutrino flux. As introduced in Chapter 3, this thesis has already constrained the contribution of such TDEs to be less than 39% of the total, under the assumption of an unbroken  $E^{-2.5}$  power law and a negative source evolution [118, 177]. We follow the same notation in Equation 4.12 of Chapter ??, with the power-law contribution of a transient source population to the diffuse neutrino flux is given by:

$$\frac{dN(E)}{dEdAdt} = \int_0^{\infty} \left[ (1+z)^{2-\gamma} \times \frac{\rho(z)\phi_0\Delta_{T'}}{4\pi D_L^2} \times \left(\frac{E}{E_0}\right)^{-\gamma} \right] \frac{dV_C}{dz} dz \quad (4.12)$$

where  $\rho(z)$  is the source rate density,  $\phi_0$  is the particle flux normalisation at reference energy  $E_0$  and  $\Delta_{T'}$  is the rest-frame duration of the transient. We can use this to calculate the cumulative distribution of neutrino flux as a function of redshift. This CDF is illustrated in Figure 4.13 for an  $E^{-2.5}$  power law, though the distribution only depends weakly on the assumed neutrino spectrum.

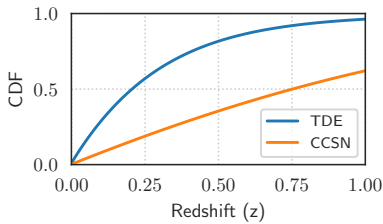


**Figure 4.13:** Cumulative distribution function (CDF) for TDE neutrino emission as a function of redshift, with the CCSN CDF plotted for comparison.

[178]: Pan-Starrs Collaboration et al. (2019), “Search for transient optical counterparts to high-energy IceCube neutrinos with Pan-STARRS1”

It is clear that, for this negative source evolution, the vast majority of TDE neutrinos are expected to arrive from sources in the local universe. This statement is independent of both the overall level of TDE neutrino production and the absolute TDE rate. ZTF has, thus far, reported the detection of TDEs up to a maximum redshift 0.212 [59]. If we simply assume that ZTF can routinely detect TDEs up to a redshift of 0.15, fully 40% of the total population flux should come from ZTF-detected sources. We would thus require that at least 2.8% of the astrophysical neutrino alerts are produced by TDEs, which is fully compatible with the stacking limit. TDE-neutrino associations can thus be detected even if the vast majority of the astrophysical neutrino flux is produced by other source classes. As is clear in Figure 4.13, the large relative contribution of detectable TDEs to the population neutrino flux is in marked contrast to supernova-like populations which are dominated by distant sources [178], so follow-up searches for TDEs are significantly more sensitive than for these other potential sources.

One further caveat introduced is that these stacking limits are derived under the assumptions of unbroken power laws which extend across a broad energy range (100 GeV - 10 PeV), where many additional neutrinos would be expected at lower energies. However, for the case of neutrino spectra dominated by high-energy components (as expected for pyc neutrino production), no such low-energy neutrinos would be expected, and these existing constraints would then be substantially weakened.

## 4.5 Implications of AT2019dsg

While the TDE-neutrino stacking analysis suggests that TDEs are not the dominant source of astrophysical neutrinos, the IC191001A-AT2019dsg association suggests that they may nonetheless contribute a subdominant component. Taken together, these two results would require TDEs as a population to contribute 3-39% of the diffuse neutrino flux. As TDE discovery rates have increased substantially since the previous IceCube analysis [59, 177], future searches will be able to study neutrino emission from TDEs with much greater sensitivity.

### Central Engine + new timescales

Of additional interest would be a new search for gamma-ray emission from TDEs which has so far not yet been observed [179]. For a pp neutrino production scenario, the associated gamma rays would however fall within the sensitive range of gamma-ray telescopes, so this scenario could be securely identified through a joint neutrino-gamma ray signal. While no gamma-ray emission was measured using the *Fermi*-LAT telescope for AT2019dsg, gamma-ray Cherenkov telescopes may be sensitive to the expected gamma-ray signal, and the corresponding low-energy (TeV) neutrino emission could confirm a hadronic origin. Conversely, the high optical depth of the UV photosphere would absorb any gamma rays accompanying py neutrino emission [180]. Some contribution from such gamma-dark sources is required to explain the large astrophysical neutrino flux [181].

The combination of gamma-ray and neutrino data would then provide an opportunity for multi-messenger analysis of TDEs. The detection of any gamma-rays would favour a pp neutrino production, while the measurement of O( $\sim$ 1-10) TeV neutrinos without accompanying gamma rays would indicate that neutrino production is occurring in the X-ray photosphere rather than in the UV photosphere. Indeed, such a detection would confirm the presence of a hidden X-ray source in the first place, while our electromagnetic observations cannot. Conversely, a lack of complementary low-energy neutrinos and gamma rays implies that only UV photons serve as a target. Neutrinos can uniquely serve as probes of the inner region of TDEs, using this novel method of extragalactic neutrino tomography.

[59]: van Velzen et al. (2020), “Seventeen Tidal Disruption Events from the First Half of ZTF Survey Observations: Entering a New Era of Population Studies”

[177]: Stein (2019), “Search for High-Energy Neutrinos from Populations of Optical Transients”

[179]: Peng et al. (2016), “Search for High-energy Gamma-ray Emission from Tidal Disruption Events with the Fermi Large Area Telescope”

[180]: Wang et al. (2016), “Tidal disruption jets of supermassive black holes as hidden sources of cosmic rays: Explaining the Ice-Cube TeV-PeV neutrinos”

[181]: Murase et al. (2016), “Hidden Cosmic-Ray Accelerators as an Origin of TeV-PeV Cosmic Neutrinos”



# **CONCLUSION**



## **APPENDIX**



# A

---

## TDE Catalogue Results

---

Table A.1: Summary of the Jetted TDE catalogue.

Source	R.A (deg.)	Dec (deg.)	Distance (Mpc)	T <sub>0</sub> (MJD)	T <sub>1</sub> (MJD)	n <sub>s</sub>
Swift J1644+57	251.21	57.58	1909	55644	55749	0.00
Swift J1112-82	167.95	-82.65	5821	55724	55828	0.00
Swift J2058+05	314.58	5.23	8308	55694	55798	1.51

**Table A.2:** Summary of the Golden TDE catalogue.

Source	R.A (deg.)	Dec (deg.)	Distance (Mpc)	$T_0$ (MJD)	$T_1$ (MJD)	$n_s$
iPTF16fnl	7.49	32.89	72	57600	57730	0.00
XMMSL1 J0740-85	115.03	85.66	76	56718	56848	0.00
ASASSN-15oi	309.79	-30.76	88	57228	57359	0.00
ASASSN-14li	192.06	17.77	91	56851	57072	0.00
ASASSN-14ae	167.17	34.10	195	56658	56851	3.40
PTF09ge	224.26	49.61	290	54953	55083	0.00
iPTF16axa	255.89	30.59	505	57432	57651	0.00
PTF09axc	223.30	22.24	538	55002	55135	0.00
PTF10nuj	246.60	54.71	627	55343	55473	0.47
PS1-10jh	242.37	53.67	826	55326	55470	0.00
PTF09djl	248.48	30.24	904	55020	55150	0.00
PTF11qlr	253.53	41.34	1031	55721	55860	0.00
PS1-11af	149.36	3.23	2232	55560	55690	0.00

**Table A.3:** Summary of the Silver TDE catalogue.

Source	R.A (deg.)	Dec (deg.)	Distance (Mpc)	$T_0$ (MJD)	$T_1$ (MJD)	$n_s$
NGC 247	11.79	-20.76	2	55593	57070	0.00
UGC 03317	83.41	73.72	18	55096	55568	0.00
PGC 1185375	225.96	1.13	23	55228	55358	0.00
PGC 1190358	226.37	1.29	33	55194	55363	0.00
PGC 015259	67.34	-4.76	64	55215	55345	1.48
AT2016ezh	29.52	-0.87	367	57597	57753	0.00
J233454	353.73	14.95	500	55129	55319	1.55
OGLE17aaaj	29.10	-71.07	546	57393	57858	0.00
F01004-2237	15.71	-22.37	555	55219	55528	0.00
J094608	146.54	35.21	561	55679	55834	3.51
XJ1500+0154	225.22	1.91	695	54509	54974	0.00
SDSSJ1201	180.40	30.05	700	54992	55457	0.00
CSS100217	157.30	40.71	705	55183	55350	0.00
SN2017bcc	172.97	30.00	711	57802	57938	0.00
DES14C1kia	53.70	-26.33	785	56972	57121	0.32
OGLE16aaa	16.84	-64.27	804	57373	57506	0.00
D23H-1	353.00	0.29	912	54342	54472	1.00
Dougie	182.20	43.02	942	54832	54962	0.00
PS1-10adi	310.69	15.51	1008	55391	55542	0.00
J094806	147.03	3.30	1031	54864	55079	0.57
PTF10iya	219.67	37.66	1127	55323	55453	0.00
ASASSN-15lh	330.56	-61.66	1175	57148	57278	0.00
PS1-13jw	131.22	42.96	1850	56323	56458	0.52
PS1-12yp	202.98	23.90	3447	55933	56126	6.65

**Table A.4:** Summary of the Obscured TDE catalogue.

Source	R.A (deg.)	Dec (deg.)	Distance (Mpc)	T <sub>0</sub> (MJD)	T <sub>1</sub> (MJD)	n <sub>s</sub>
J130819	197.08	43.76	162	54991	55456	7.10
J134244	205.69	5.52	162	54845	55310	0.65
J100933	152.39	23.38	328	54962	55427	0.00
J133737	204.40	20.40	331	54839	55304	0.00
J121116	182.82	0.23	349	54999	55464	0.00
J142401	216.01	29.84	394	54845	55310	0.00
J030257	45.74	-8.50	493	54857	55322	0.00
J141036	212.65	26.91	501	55206	55671	4.87
J113527	173.86	39.47	507	54974	55439	0.00
J145851	224.72	17.85	548	54857	55322	11.88
J133837	204.66	57.52	601	54983	55448	1.39
J155223	238.10	32.58	605	55045	55510	0.63
J091225	138.10	6.17	697	54955	55420	1.09
J123715	189.31	60.20	1083	54967	55432	1.74



# Bibliography

Here are the references in citation order.

- [1] M. Turatto. “Classification of Supernovae.” In: *Supernovae and Gamma-Ray Bursters*. Ed. by K. Weiler. Vol. 598. 2003, pp. 21–36. doi: [10.1007/3-540-45863-8\\_3](https://doi.org/10.1007/3-540-45863-8_3).
- [2] S. Chandrasekhar. “The Maximum Mass of Ideal White Dwarfs.” In: *ApJ* 74 (July 1931), p. 81. doi: [10.1086/143324](https://doi.org/10.1086/143324).
- [3] Christian D Ott. “The gravitational-wave signature of core-collapse supernovae.” In: *Classical and Quantum Gravity* 26.6, 063001 (Mar. 2009), p. 063001. doi: [10.1088/0264-9381/26/6/063001](https://doi.org/10.1088/0264-9381/26/6/063001).
- [4] B. P. Abbott et al. “Optically targeted search for gravitational waves emitted by core-collapse supernovae during the first and second observing runs of advanced LIGO and advanced Virgo.” In: *Phys. Rev. D* 101.8, 084002 (Apr. 2020), p. 084002. doi: [10.1103/PhysRevD.101.084002](https://doi.org/10.1103/PhysRevD.101.084002).
- [5] K. Hirata et al. “Observation of a neutrino burst from the supernova SN1987A.” In: *Phys. Rev. Lett.* 58.14 (Apr. 1987), pp. 1490–1493. doi: [10.1103/PhysRevLett.58.1490](https://doi.org/10.1103/PhysRevLett.58.1490).
- [6] A. Mirizzi et al. “Supernova neutrinos: production, oscillations and detection.” In: *Nuovo Cimento Rivista Serie* 39.1-2 (Feb. 2016), pp. 1–112. doi: [10.1393/ncr/i2016-10120-8](https://doi.org/10.1393/ncr/i2016-10120-8).
- [7] Kohta Murase et al. “New class of high-energy transients from crashes of supernova ejecta with massive circumstellar material shells.” In: *Phys. Rev. D* 84.4, 043003 (Aug. 2011), p. 043003. doi: [10.1103/PhysRevD.84.043003](https://doi.org/10.1103/PhysRevD.84.043003).
- [8] Alexander Johannes Stasik. “Search for High Energetic Neutrinos from Core Collapse Supernovae using the IceCube Neutrino Telescope.” PhD thesis. Humboldt-Universitaet zu Berlin, Mathematisch-Naturwissenschaftliche Fakultaet, 2018. doi: <http://dx.doi.org/10.18452/18729>.
- [9] Jon C. Mauerhan et al. “SN 2011ht: confirming a class of interacting supernovae with plateau light curves (Type IIn-P).” In: *MNRAS* 431.3 (May 2013), pp. 2599–2611. doi: [10.1093/mnras/stt360](https://doi.org/10.1093/mnras/stt360).
- [10] Eli Waxman and John Bahcall. “High Energy Neutrinos from Cosmological Gamma-Ray Burst Fireballs.” In: *Phys. Rev. Lett.* 78.12 (Mar. 1997), pp. 2292–2295. doi: [10.1103/PhysRevLett.78.2292](https://doi.org/10.1103/PhysRevLett.78.2292).
- [11] T. J. Galama et al. “An unusual supernova in the error box of the  $\gamma$ -ray burst of 25 April 1998.” In: *Nature* 395.6703 (Oct. 1998), pp. 670–672. doi: [10.1038/27150](https://doi.org/10.1038/27150).
- [12] M. G. Aartsen et al. “Extending the Search for Muon Neutrinos Coincident with Gamma-Ray Bursts in IceCube Data.” In: *ApJ* 843.2, 112 (July 2017), p. 112. doi: [10.3847/1538-4357/aa7569](https://doi.org/10.3847/1538-4357/aa7569).
- [13] MAGIC Collaboration et al. “Teraelectronvolt emission from the  $\gamma$ -ray burst GRB 190114C.” In: *Nature* 575.7783 (Nov. 2019), pp. 455–458. doi: [10.1038/s41586-019-1750-x](https://doi.org/10.1038/s41586-019-1750-x).
- [14] Razmik Mirzoyan. “First time detection of a GRB at sub-TeV energies; MAGIC detects the GRB 190114C.” In: *The Astronomer’s Telegram* 12390 (Jan. 2019), p. 1.
- [15] H. Abdalla et al. “A very-high-energy component deep in the  $\gamma$ -ray burst afterglow.” In: *Nature* 575.7783 (Nov. 2019), pp. 464–467. doi: [10.1038/s41586-019-1743-9](https://doi.org/10.1038/s41586-019-1743-9).
- [16] James David Casey. “Search for high energy GRB neutrinos in IceCube.” PhD thesis. Georgia Tech, 2015.
- [17] Enwei Liang et al. “Low-Luminosity Gamma-Ray Bursts as a Unique Population: Luminosity Function, Local Rate, and Beaming Factor.” In: *ApJ* 662.2 (June 2007), pp. 1111–1118. doi: [10.1086/517959](https://doi.org/10.1086/517959).
- [18] Ehud Nakar. “A Unified Picture for Low-luminosity and Long Gamma-Ray Bursts Based on the Extended Progenitor of llGRB 060218/SN 2006aj.” In: *ApJ* 807.2, 172 (July 2015), p. 172. doi: [10.1088/0004-637X/807/2/172](https://doi.org/10.1088/0004-637X/807/2/172).

- [19] Nicholas Senno, Kohta Murase, and Peter Mészáros. “Choked jets and low-luminosity gamma-ray bursts as hidden neutrino sources.” In: *Phys. Rev. D* 93.8, 083003 (Apr. 2016), p. 083003. doi: [10.1103/PhysRevD.93.083003](https://doi.org/10.1103/PhysRevD.93.083003).
- [20] Nora Linn Strotjohann. “Search for minute-scale transient neutrino sources with IceCube’s optical follow-up program.” PhD thesis. Humboldt-Universität zu Berlin, Mathematisch-Naturwissenschaftliche Fakultät, 2020. doi: <http://dx.doi.org/10.18452/20700> (cited on page 26).
- [21] Tycho Brahe. *De nova et nullius aevi memoria prius visa stella.* 1573.
- [22] T. C. Weekes et al. “Observation of TeV Gamma Rays from the Crab Nebula Using the Atmospheric Cerenkov Imaging Technique.” In: *ApJ* 342 (July 1989), p. 379. doi: [10.1086/167599](https://doi.org/10.1086/167599).
- [23] T. K. Gaisser, F. Halzen, and T. Stanev. “Particle astrophysics with high energy neutrinos.” In: *Phys. Rep.* 258 (July 1995), pp. 173–236. doi: [10.1016/0370-1573\(95\)00003-Y](https://doi.org/10.1016/0370-1573(95)00003-Y).
- [24] M. G. Aartsen et al. “Constraints on Galactic Neutrino Emission with Seven Years of IceCube Data.” In: *ApJ* 849.1, 67 (Nov. 2017), p. 67. doi: [10.3847/1538-4357/aa8dfb](https://doi.org/10.3847/1538-4357/aa8dfb).
- [25] A. Hewish et al. “Observation of a Rapidly Pulsating Radio Source.” In: *Nature* 217.5130 (Feb. 1968), pp. 709–713. doi: [10.1038/217709a0](https://doi.org/10.1038/217709a0).
- [26] W. Bednarek. “Neutrinos from the pulsar wind nebulae.” In: *A&A* 407 (Aug. 2003), pp. 1–6. doi: [10.1051/0004-6361:20030929](https://doi.org/10.1051/0004-6361:20030929).
- [27] M. G. Aartsen et al. “IceCube Search for High-energy Neutrino Emission from TeV Pulsar Wind Nebulae.” In: *ApJ* 898.2, 117 (Aug. 2020), p. 117. doi: [10.3847/1538-4357/ab9fa0](https://doi.org/10.3847/1538-4357/ab9fa0).
- [28] B. S. Sathyaprakash and Bernard F. Schutz. “Physics, Astrophysics and Cosmology with Gravitational Waves.” In: *Living Reviews in Relativity* 12.1, 2 (Dec. 2009), p. 2. doi: [10.12942/lrr-2009-2](https://doi.org/10.12942/lrr-2009-2).
- [29] B. P. Abbott et al. “Searches for Gravitational Waves from Known Pulsars at Two Harmonics in 2015–2017 LIGO Data.” In: *ApJ* 879.1, 10 (July 2019), p. 10. doi: [10.3847/1538-4357/ab20cb](https://doi.org/10.3847/1538-4357/ab20cb).
- [30] Victoria M. Kaspi and Andrei M. Beloborodov. “Magnetars.” In: *ARA&A* 55.1 (Aug. 2017), pp. 261–301. doi: [10.1146/annurev-astro-081915-023329](https://doi.org/10.1146/annurev-astro-081915-023329).
- [31] Bing Zhang et al. “High-Energy Neutrinos from Magnetars.” In: *ApJ* 595.1 (Sept. 2003), pp. 346–351. doi: [10.1086/377192](https://doi.org/10.1086/377192).
- [32] J. Ahrens et al. “Search for Extraterrestrial Point Sources of Neutrinos with AMANDA-II.” In: *Phys. Rev. Lett.* 92.7, 071102 (Feb. 2004), p. 071102. doi: [10.1103/PhysRevLett.92.071102](https://doi.org/10.1103/PhysRevLett.92.071102).
- [33] D. R. Lorimer et al. “A Bright Millisecond Radio Burst of Extragalactic Origin.” In: *Science* 318.5851 (Nov. 2007), p. 777. doi: [10.1126/science.1147532](https://doi.org/10.1126/science.1147532).
- [34] C. D. Bochenek et al. “A fast radio burst associated with a Galactic magnetar.” In: *Nature* 587.7832 (Nov. 2020), pp. 59–62. doi: [10.1038/s41586-020-2872-x](https://doi.org/10.1038/s41586-020-2872-x).
- [35] L. G. Spitler et al. “A repeating fast radio burst.” In: *Nature* 531.7593 (Mar. 2016), pp. 202–205. doi: [10.1038/nature17168](https://doi.org/10.1038/nature17168).
- [36] E. Petroff, J. W. T. Hessels, and D. R. Lorimer. “Fast radio bursts.” In: *A&A Rev.* 27.1, 4 (May 2019), p. 4. doi: [10.1007/s00159-019-0116-6](https://doi.org/10.1007/s00159-019-0116-6).
- [37] Xiang Li et al. “Model-dependent Estimate on the Connection between Fast Radio Bursts and Ultra High Energy Cosmic Rays.” In: *ApJ* 797.1, 33 (Dec. 2014), p. 33. doi: [10.1088/0004-637X/797/1/33](https://doi.org/10.1088/0004-637X/797/1/33).
- [38] R. Abbasi et al. “Follow-up of astrophysical transients in real time with the IceCube Neutrino Observatory.” In: *arXiv e-prints*, arXiv:2012.04577 (Dec. 2020), arXiv:2012.04577 (cited on page 42).
- [39] K. Ioka. “Magnetic deformation of magnetars for the giant flares of the soft gamma-ray repeaters.” In: *MNRAS* 327.2 (Oct. 2001), pp. 639–662. doi: [10.1046/j.1365-8711.2001.04756.x](https://doi.org/10.1046/j.1365-8711.2001.04756.x).
- [40] B. P. Abbott et al. “Search for Transient Gravitational-wave Signals Associated with Magnetar Bursts during Advanced LIGO’s Second Observing Run.” In: *ApJ* 874.2, 163 (Apr. 2019), p. 163. doi: [10.3847/1538-4357/ab0e15](https://doi.org/10.3847/1538-4357/ab0e15).

- [41] J. H. Taylor and J. M. Weisberg. "Further Experimental Tests of Relativistic Gravity Using the Binary Pulsar PSR 1913+16." In: *ApJ* 345 (Oct. 1989), p. 434. doi: [10.1086/167917](https://doi.org/10.1086/167917).
- [42] B. P. Abbott et al. "Observation of Gravitational Waves from a Binary Black Hole Merger." In: *Phys. Rev. Lett.* 116.6, 061102 (Feb. 2016), p. 061102. doi: [10.1103/PhysRevLett.116.061102](https://doi.org/10.1103/PhysRevLett.116.061102).
- [43] Kohta Murase et al. "Ultrafast Outflows from Black Hole Mergers with a Minidisk." In: *ApJ* 822.1, L9 (May 2016), p. L9. doi: [10.3847/2041-8205/822/1/L9](https://doi.org/10.3847/2041-8205/822/1/L9).
- [44] M. J. Graham et al. "Candidate Electromagnetic Counterpart to the Binary Black Hole Merger Gravitational-Wave Event S190521g\*." In: *Phys. Rev. Lett.* 124.25, 251102 (June 2020), p. 251102. doi: [10.1103/PhysRevLett.124.251102](https://doi.org/10.1103/PhysRevLett.124.251102).
- [45] M. G. Aartsen et al. "IceCube Search for Neutrinos Coincident with Compact Binary Mergers from LIGO-Virgo's First Gravitational-wave Transient Catalog." In: *ApJ* 898.1, L10 (July 2020), p. L10. doi: [10.3847/2041-8213/ab9d24](https://doi.org/10.3847/2041-8213/ab9d24).
- [46] B. P. Abbott et al. "GW170817: Observation of Gravitational Waves from a Binary Neutron Star Inspiral." In: *Phys. Rev. Lett.* 119.16, 161101 (Oct. 2017), p. 161101. doi: [10.1103/PhysRevLett.119.161101](https://doi.org/10.1103/PhysRevLett.119.161101).
- [47] B. P. Abbott et al. "Multi-messenger Observations of a Binary Neutron Star Merger." In: *ApJ* 848.2, L12 (Oct. 2017), p. L12. doi: [10.3847/2041-8213/aa91c9](https://doi.org/10.3847/2041-8213/aa91c9).
- [48] Ramesh Narayan, Bohdan Paczynski, and Tsvi Piran. "Gamma-Ray Bursts as the Death Throes of Massive Binary Stars." In: *ApJ* 395 (Aug. 1992), p. L83. doi: [10.1086/186493](https://doi.org/10.1086/186493).
- [49] Davide Lazzati et al. "Late Time Afterglow Observations Reveal a Collimated Relativistic Jet in the Ejecta of the Binary Neutron Star Merger GW170817." In: *Phys. Rev. Lett.* 120.24, 241103 (June 2018), p. 241103. doi: [10.1103/PhysRevLett.120.241103](https://doi.org/10.1103/PhysRevLett.120.241103).
- [50] B. P. Abbott et al. "Gravitational Waves and Gamma-Rays from a Binary Neutron Star Merger: GW170817 and GRB 170817A." In: *ApJ* 848.2, L13 (Oct. 2017), p. L13. doi: [10.3847/2041-8213/aa920c](https://doi.org/10.3847/2041-8213/aa920c).
- [51] R. Hussain, J. Vandenbroucke, and J. Wood. "A Search for IceCube Neutrinos from the First 29 Detected Gravitational Wave Events." In: *36th International Cosmic Ray Conference (ICRC2019)*. Vol. 36. International Cosmic Ray Conference. July 2019, 918, p. 918.
- [52] Li-Xin Li and Bohdan Paczyński. "Transient Events from Neutron Star Mergers." In: *ApJ* 507.1 (Nov. 1998), pp. L59–L62. doi: [10.1086/311680](https://doi.org/10.1086/311680).
- [53] Martin J. Rees. "Tidal disruption of stars by black holes of  $10^6$ - $10^8$  solar masses in nearby galaxies." In: *Nature* 333.6173 (June 1988), pp. 523–528. doi: [10.1038/333523a0](https://doi.org/10.1038/333523a0).
- [54] Charles R. Evans and Christopher S. Kochanek. "The Tidal Disruption of a Star by a Massive Black Hole." In: *ApJ* 346 (Nov. 1989), p. L13. doi: [10.1086/185567](https://doi.org/10.1086/185567).
- [55] Stefanie Komossa and Norbert Bade. "The giant X-ray outbursts in NGC 5905 and IC 3599: Follow-up observations and outburst scenarios." In: *A&A* 343 (Mar. 1999), pp. 775–787.
- [56] Katie Auchettl, James Guillochon, and Enrico Ramirez-Ruiz. "New Physical Insights about Tidal Disruption Events from a Comprehensive Observational Inventory at X-Ray Wavelengths." In: *ApJ* 838.2, 149 (Apr. 2017), p. 149. doi: [10.3847/1538-4357/aa633b](https://doi.org/10.3847/1538-4357/aa633b).
- [57] Joshua S. Bloom et al. "A Possible Relativistic Jetted Outburst from a Massive Black Hole Fed by a Tidally Disrupted Star." In: *Science* 333.6039 (July 2011), p. 203. doi: [10.1126/science.1207150](https://doi.org/10.1126/science.1207150).
- [58] S. Mattila et al. "A dust-enshrouded tidal disruption event with a resolved radio jet in a galaxy merger." In: *Science* 361.6401 (Aug. 2018), pp. 482–485. doi: [10.1126/science.aa04669](https://doi.org/10.1126/science.aa04669).
- [59] Sjoert van Velzen et al. "Seventeen Tidal Disruption Events from the First Half of ZTF Survey Observations: Entering a New Era of Population Studies." In: *arXiv e-prints*, arXiv:2001.01409 (Jan. 2020), arXiv:2001.01409 (cited on pages 51, 58, 60, 66, 67).
- [60] Kate D. Alexander et al. "Radio Properties of Tidal Disruption Events." In: *Space Sci. Rev.* 216.5, 81 (June 2020), p. 81. doi: [10.1007/s11214-020-00702-w](https://doi.org/10.1007/s11214-020-00702-w).

- [61] Dheeraj R. Pasham and Sjoert van Velzen. “Discovery of a Time Lag between the Soft X-Ray and Radio Emission of the Tidal Disruption Flare ASASSN-14li: Evidence for Linear Disk-Jet Coupling.” In: *ApJ* 856.1, 1 (Mar. 2018), p. 1. doi: [10.3847/1538-4357/aab361](https://doi.org/10.3847/1538-4357/aab361).
- [62] Glennys R. Farrar and Andrei Gruzinov. “Giant AGN Flares and Cosmic Ray Bursts.” In: *ApJ* 693.1 (Mar. 2009), pp. 329–332. doi: [10.1088/0004-637X/693/1/329](https://doi.org/10.1088/0004-637X/693/1/329).
- [63] Daniel Biehl et al. “Tidally disrupted stars as a possible origin of both cosmic rays and neutrinos at the highest energies.” In: *Sci. Rep.* 8.1 (2018), p. 10828. doi: [10.1038/s41598-018-29022-4](https://doi.org/10.1038/s41598-018-29022-4).
- [64] Shiro Kobayashi et al. “Gravitational Waves and X-Ray Signals from Stellar Disruption by a Massive Black Hole.” In: *ApJ* 615.2 (Nov. 2004), pp. 855–865. doi: [10.1086/424684](https://doi.org/10.1086/424684).
- [65] M. R. Drout et al. “Rapidly Evolving and Luminous Transients from Pan-STARRS1.” In: *ApJ* 794.1, 23 (Oct. 2014), p. 23. doi: [10.1088/0004-637X/794/1/23](https://doi.org/10.1088/0004-637X/794/1/23) (cited on pages 42, 43).
- [66] R. Margutti et al. “An Embedded X-Ray Source Shines through the Aspherical AT 2018cow: Revealing the Inner Workings of the Most Luminous Fast-evolving Optical Transients.” In: *Astrophys. J.* 872.1 (2019), p. 18. doi: [10.3847/1538-4357/aafa01](https://doi.org/10.3847/1538-4357/aafa01) (cited on page 42).
- [67] Daniel A. Perley et al. “The Fast, Luminous Ultraviolet Transient AT2018cow: Extreme Supernova, or Disruption of a Star by an Intermediate-Mass Black Hole?” In: *Mon. Not. Roy. Astron. Soc.* 484.1 (2019), pp. 1031–1049. doi: [10.1093/mnras/sty3420](https://doi.org/10.1093/mnras/sty3420) (cited on page 42).
- [68] Ke Fang et al. “Multimessenger Implications of AT2018cow: High-energy Cosmic-Ray and Neutrino Emissions from Magnetar-powered Superluminous Transients.” In: *ApJ* 878.1, 34 (June 2019), p. 34. doi: [10.3847/1538-4357/ab1b72](https://doi.org/10.3847/1538-4357/ab1b72).
- [69] Daniele Gaggero et al. “The Gamma-Ray and Neutrino Sky: A Consistent Picture of Fermi-LAT, Milagro, and IceCube Results.” In: *ApJ* 815.2, L25 (Dec. 2015), p. L25. doi: [10.1088/2041-8205/815/2/L25](https://doi.org/10.1088/2041-8205/815/2/L25).
- [70] Volker Beckmann and Chris R. Shrader. *Active Galactic Nuclei*. 2012.
- [71] Carl K. Seyfert. “Nuclear Emission in Spiral Nebulae.” In: *ApJ* 97 (Jan. 1943), p. 28. doi: [10.1086/144488](https://doi.org/10.1086/144488).
- [72] D. E. Osterbrock. “Seyfert galaxies with weak broad H alpha emission lines.” In: *ApJ* 249 (Oct. 1981), pp. 462–470. doi: [10.1086/159306](https://doi.org/10.1086/159306).
- [73] B. L. Fanaroff and J. M. Riley. “The morphology of extragalactic radio sources of high and low luminosity.” In: *MNRAS* 167 (May 1974), 31P–36P. doi: [10.1093/mnras/167.1.31P](https://doi.org/10.1093/mnras/167.1.31P).
- [74] C. Megan Urry and Paolo Padovani. “Unified Schemes for Radio-Loud Active Galactic Nuclei.” In: *PASP* 107 (Sept. 1995), p. 803. doi: [10.1086/133630](https://doi.org/10.1086/133630).
- [75] B. J. Shappee et al. “The Man behind the Curtain: X-Rays Drive the UV through NIR Variability in the 2013 Active Galactic Nucleus Outburst in NGC 2617.” In: *ApJ* 788.1, 48 (June 2014), p. 48. doi: [10.1088/0004-637X/788/1/48](https://doi.org/10.1088/0004-637X/788/1/48).
- [76] K. Mannheim. “The proton blazar.” In: *A&A* 269 (Mar. 1993), pp. 67–76.
- [77] Gabriele Ghisellini. “The Blazar Sequence 2.0.” In: *Galaxies* 4.4 (Sept. 2016), p. 36. doi: [10.3390/galaxies4040036](https://doi.org/10.3390/galaxies4040036).
- [78] S. Abdollahi et al. “Fermi Large Area Telescope Fourth Source Catalog.” In: *ApJS* 247.1, 33 (Mar. 2020), p. 33. doi: [10.3847/1538-4365/ab6bcb](https://doi.org/10.3847/1538-4365/ab6bcb).
- [79] M. Ajello et al. “The Origin of the Extragalactic Gamma-Ray Background and Implications for Dark Matter Annihilation.” In: *ApJ* 800.2, L27 (Feb. 2015), p. L27. doi: [10.1088/2041-8205/800/2/L27](https://doi.org/10.1088/2041-8205/800/2/L27).
- [80] M. Punch et al. “Detection of TeV photons from the active galaxy Markarian 421.” In: *Nature* 358.6386 (Aug. 1992), pp. 477–478. doi: [10.1038/358477a0](https://doi.org/10.1038/358477a0).
- [81] Justin D. Finke, Soebur Razzaque, and Charles D. Dermer. “Modeling the Extragalactic Background Light from Stars and Dust.” In: *ApJ* 712.1 (Mar. 2010), pp. 238–249. doi: [10.1088/0004-637X/712/1/238](https://doi.org/10.1088/0004-637X/712/1/238).

- [82] M. G. Aartsen et al. “The Contribution of Fermi-2LAC Blazars to Diffuse TeV-PeV Neutrino Flux.” In: *ApJ* 835.1, 45 (Jan. 2017), p. 45. doi: [10.3847/1538-4357/835/1/45](https://doi.org/10.3847/1538-4357/835/1/45).
- [83] Kohta Murase, Dafne Guetta, and Markus Ahlers. “Hidden Cosmic-Ray Accelerators as an Origin of TeV-PeV Cosmic Neutrinos.” In: *Phys. Rev. Lett.* 116.7, 071101 (Feb. 2016), p. 071101. doi: [10.1103/PhysRevLett.116.071101](https://doi.org/10.1103/PhysRevLett.116.071101).
- [84] Andrea Palladino et al. “Interpretation of the Diffuse Astrophysical Neutrino Flux in Terms of the Blazar Sequence.” In: *ApJ* 871.1, 41 (Jan. 2019), p. 41. doi: [10.3847/1538-4357/aaf507](https://doi.org/10.3847/1538-4357/aaf507).
- [85] IceCube Collaboration et al. “Multimessenger observations of a flaring blazar coincident with high-energy neutrino IceCube-170922A.” In: *Science* 361.6398, eaat1378 (July 2018), eaat1378. doi: [10.1126/science.aat1378](https://doi.org/10.1126/science.aat1378) (cited on pages 60, 62).
- [86] M. G. Aartsen et al. “Neutrino emission from the direction of the blazar TXS 0506+056 prior to the IceCube-170922A alert.” In: *Science* 361.6398 (2018), pp. 147–151. doi: [10.1126/science.aat2890](https://doi.org/10.1126/science.aat2890).
- [87] S. Garrappa et al. “Investigation of Two Fermi-LAT Gamma-Ray Blazars Coincident with High-energy Neutrinos Detected by IceCube.” In: *ApJ* 880.2, 103 (Aug. 2019), p. 103. doi: [10.3847/1538-4357/ab2ada](https://doi.org/10.3847/1538-4357/ab2ada).
- [88] Yasuyuki T. Tanaka, Sara Buson, and Daniel Kocevski. “Fermi-LAT detection of increased gamma-ray activity of TXS 0506+056, located inside the IceCube-170922A error region.” In: *The Astronomer’s Telegram* 10791 (Sept. 2017), p. 1.
- [89] Shan Gao et al. “Modelling the coincident observation of a high-energy neutrino and a bright blazar flare.” In: *Nature Astronomy* 3 (Jan. 2019), pp. 88–92. doi: [10.1038/s41550-018-0610-1](https://doi.org/10.1038/s41550-018-0610-1).
- [90] Nora Linn Strotjohann, Marek Kowalski, and Anna Franckowiak. “Eddington bias for cosmic neutrino sources.” In: *A&A* 622, L9 (Feb. 2019), p. L9. doi: [10.1051/0004-6361/201834750](https://doi.org/10.1051/0004-6361/201834750) (cited on page 64).
- [91] Xavier Rodrigues et al. “Leptohadronic Blazar Models Applied to the 2014-2015 Flare of TXS 0506+056.” In: *ApJ* 874.2, L29 (Apr. 2019), p. L29. doi: [10.3847/2041-8213/ab1267](https://doi.org/10.3847/2041-8213/ab1267).
- [92] Francis Halzen et al. “On the Neutrino Flares from the Direction of TXS 0506+056.” In: *ApJ* 874.1, L9 (Mar. 2019), p. L9. doi: [10.3847/2041-8213/ab0d27](https://doi.org/10.3847/2041-8213/ab0d27).
- [93] F. W. Stecker et al. “High-energy neutrinos from active galactic nuclei.” In: *Phys. Rev. Lett.* 66.21 (May 1991), pp. 2697–2700. doi: [10.1103/PhysRevLett.66.2697](https://doi.org/10.1103/PhysRevLett.66.2697).
- [94] Federica Bradascio. “Searches for cross-correlations between IceCube neutrinos and Active Galactic Nuclei selected in various bands of the electromagnetic spectrum.” PhD thesis. Humboldt-Universität zu Berlin, Mathematisch-Naturwissenschaftliche Fakultät, 2021. doi: [FIXME](#).
- [95] M. G. Aartsen et al. “Time-Integrated Neutrino Source Searches with 10 Years of IceCube Data.” In: *Phys. Rev. Lett.* 124.5, 051103 (Feb. 2020), p. 051103. doi: [10.1103/PhysRevLett.124.051103](https://doi.org/10.1103/PhysRevLett.124.051103) (cited on pages 7, 44, 60).
- [96] Yoshiyuki Inoue, Dmitry Khangulyan, and Akihiro Doi. “On the Origin of High-energy Neutrinos from NGC 1068: The Role of Nonthermal Coronal Activity.” In: *ApJ* 891.2, L33 (Mar. 2020), p. L33. doi: [10.3847/2041-8213/ab7661](https://doi.org/10.3847/2041-8213/ab7661).
- [97] Abraham Loeb and Eli Waxman. “The cumulative background of high energy neutrinos from starburst galaxies.” In: *J. Cosmology Astropart. Phys.* 2006.5, 003 (May 2006), p. 003. doi: [10.1088/1475-7516/2006/05/003](https://doi.org/10.1088/1475-7516/2006/05/003).
- [98] Keith Bechtol et al. “Evidence against Star-forming Galaxies as the Dominant Source of Icecube Neutrinos.” In: *ApJ* 836.1, 47 (Feb. 2017), p. 47. doi: [10.3847/1538-4357/836/1/47](https://doi.org/10.3847/1538-4357/836/1/47).
- [99] S. Detweiler. “Pulsar timing measurements and the search for gravitational waves.” In: *ApJ* 234 (Dec. 1979), pp. 1100–1104. doi: [10.1086/157593](https://doi.org/10.1086/157593).
- [100] Pau Amaro-Seoane et al. “Laser Interferometer Space Antenna.” In: *arXiv e-prints*, arXiv:1702.00786 (Feb. 2017), arXiv:1702.00786.
- [101] Chengchao Yuan et al. “High-energy neutrino emission subsequent to gravitational wave radiation from supermassive black hole mergers.” In: *Phys. Rev. D* 102.8, 083013 (Oct. 2020), p. 083013. doi: [10.1103/PhysRevD.102.083013](https://doi.org/10.1103/PhysRevD.102.083013).

- [102] P. B. Ivanov, A. G. Polnarev, and P. Saha. “The tidal disruption rate in dense galactic cusps containing a supermassive binary black hole.” In: *MNRAS* 358.4 (Apr. 2005), pp. 1361–1378. doi: [10.1111/j.1365-2966.2005.08843.x](https://doi.org/10.1111/j.1365-2966.2005.08843.x).
- [103] Ryan Edward Maunu. “A Search for Muon Neutrinos in Coincidence with Gamma-Ray Bursts in the Southern Hemisphere Sky Using the IceCube Neutrino Observatory.” PhD thesis. University of Maryland, Department of Physics, 2016. doi: <https://doi.org/10.13016/M2449P>.
- [104] M. G. Aartsen et al. “A Combined Maximum-likelihood Analysis of the High-energy Astrophysical Neutrino Flux Measured with IceCube.” In: *ApJ* 809.1, 98 (Aug. 2015), p. 98. doi: [10.1088/0004-637X/809/1/98](https://doi.org/10.1088/0004-637X/809/1/98) (cited on page 40).
- [105] The IceCube-Gen2 Collaboration et al. “IceCube-Gen2: The Window to the Extreme Universe.” In: *arXiv e-prints*, arXiv:2008.04323 (Aug. 2020), arXiv:2008.04323.
- [106] Robert Stein et al. *icecube/flarestack*. Apr. 2020. doi: [10.5281/zenodo.3619383](https://doi.org/10.5281/zenodo.3619383) (cited on pages 6, 25).
- [107] M. G. Aartsen et al. “The IceCube Neutrino Observatory: Instrumentation and Online Systems.” In: *JINST* 12.03 (2017), P03012. doi: [10.1088/1748-0221/12/03/P03012](https://doi.org/10.1088/1748-0221/12/03/P03012) (cited on page 7).
- [108] IceCube Collaboration et al. “Search for steady point-like sources in the astrophysical muon neutrino flux with 8 years of IceCube data.” In: *arXiv e-prints*, arXiv:1811.07979 (Nov. 2018), arXiv:1811.07979 (cited on page 7).
- [109] Patrick Heix et al. “Seasonal Variation of Atmospheric Neutrinos in IceCube.” In: *arXiv e-prints*, arXiv:1909.02036 (Sept. 2019), arXiv:1909.02036 (cited on page 8).
- [110] D. Chirkin and M. Rongen. “Light diffusion in birefringent polycrystals and the IceCube ice anisotropy.” In: *36th International Cosmic Ray Conference (ICRC2019)*. Vol. 36. International Cosmic Ray Conference. July 2019, 854, p. 854 (cited on page 9).
- [111] J. Neyman and E. S. Pearson. “On the Problem of the Most Efficient Tests of Statistical Hypotheses.” In: *Philosophical Transactions of the Royal Society of London Series A* 231 (Jan. 1933), pp. 289–337. doi: [10.1098/rsta.1933.0009](https://doi.org/10.1098/rsta.1933.0009) (cited on page 14).
- [112] Jim Braun et al. “Methods for point source analysis in high energy neutrino telescopes.” In: *Astroparticle Physics* 29.4 (May 2008), pp. 299–305. doi: [10.1016/j.astropartphys.2008.02.007](https://doi.org/10.1016/j.astropartphys.2008.02.007) (cited on page 14).
- [113] S.S. Wilks. “The Large-Sample Distribution of the Likelihood Ratio for Testing Composite Hypotheses.” In: *Annals Math. Statist.* 9.1 (1938), pp. 60–62. doi: [10.1214/aoms/1177732360](https://doi.org/10.1214/aoms/1177732360) (cited on page 15).
- [114] Alexander Johannes Stasik. “Search for High Energetic Neutrinos from Core Collapse Supernovae using the IceCube Neutrino Telescope.” PhD thesis. Humboldt U., Berlin, 2017. doi: [10.18452/18729](https://doi.org/10.18452/18729) (cited on page 22).
- [115] Daniel A. Perley et al. “The Zwicky Transient Facility Bright Transient Survey. II. A Public Statistical Sample for Exploring Supernova Demographics.” In: *ApJ* 904.1, 35 (Nov. 2020), p. 35. doi: [10.3847/1538-4357/abbd98](https://doi.org/10.3847/1538-4357/abbd98) (cited on pages 25, 30, 31).
- [116] Piero Madau and Mark Dickinson. “Cosmic Star-Formation History.” In: *ARA&A* 52 (Aug. 2014), pp. 415–486. doi: [10.1146/annurev-astro-081811-125615](https://doi.org/10.1146/annurev-astro-081811-125615) (cited on pages 26, 41, 43).
- [117] Louis-Gregory Strolger et al. “The Rate of Core Collapse Supernovae to Redshift 2.5 from the CANDELS and CLASH Supernova Surveys.” In: *ApJ* 813.2, 93 (Nov. 2015), p. 93. doi: [10.1088/0004-637X/813/2/93](https://doi.org/10.1088/0004-637X/813/2/93) (cited on page 26).
- [118] Hui Sun, Bing Zhang, and Zhuo Li. “Extragalactic High-energy Transients: Event Rate Densities and Luminosity Functions.” In: *Astrophys. J.* 812.1 (2015), p. 33. doi: [10.1088/0004-637X/812/1/33](https://doi.org/10.1088/0004-637X/812/1/33) (cited on pages 26, 40, 41, 66).
- [119] Astropy Collaboration et al. “Astropy: A community Python package for astronomy.” In: *A&A* 558, A33 (Oct. 2013), A33. doi: [10.1051/0004-6361/201322068](https://doi.org/10.1051/0004-6361/201322068) (cited on page 27).

- [120] Ali Kheirandish, Alex Pizzuto, and Justin Vandenbroucke. “Searches for neutrinos from fast radio bursts with IceCube.” In: *arXiv e-prints*, arXiv:1909.00078 (Aug. 2019), arXiv:1909.00078 (cited on page 32).
- [121] R. Stein. “Search for High-Energy Neutrinos from Populations of Optical Transients.” In: *36th International Cosmic Ray Conference (ICRC2019)*. Vol. 36. International Cosmic Ray Conference. July 2019, 1016, p. 1016 (cited on page 35).
- [122] Katie Auchettl, James Guillochon, and Enrico Ramirez-Ruiz. “New Physical Insights about Tidal Disruption Events from a Comprehensive Observational Inventory at X-Ray Wavelengths.” In: *ApJ* 838.2, 149 (Apr. 2017), p. 149. doi: [10.3847/1538-4357/aa633b](https://doi.org/10.3847/1538-4357/aa633b) (cited on page 36).
- [123] Tinggui Wang et al. “Long-Term Decline of the Mid-Infrared Emission of Normal Galaxies: Dust Echo of Tidal Disruption Flare?” In: *Mon. Not. Roy. Astron. Soc.* 477.3 (2018), pp. 2943–2965. doi: [10.1093/mnras/sty465](https://doi.org/10.1093/mnras/sty465) (cited on page 37).
- [124] S. van Velzen. “On the Mass and Luminosity Functions of Tidal Disruption Flares: Rate Suppression due to Black Hole Event Horizons.” In: *ApJ* 852.2, 72 (Jan. 2018), p. 72. doi: [10.3847/1538-4357/aa998e](https://doi.org/10.3847/1538-4357/aa998e) (cited on page 40).
- [125] S. E. Woosley and J. S. Bloom. “The Supernova Gamma-Ray Burst Connection.” In: *ARA&A* 44.1 (Sept. 2006), pp. 507–556. doi: [10.1146/annurev.astro.43.072103.150558](https://doi.org/10.1146/annurev.astro.43.072103.150558) (cited on page 42).
- [126] E. Blaufuss. “AT2018cow: IceCube neutrino search.” In: *The Astronomer’s Telegram* 11785 (June 2018) (cited on pages 42, 43).
- [127] Ke Fang et al. “Multimessenger Implications of AT2018cow: High-energy Cosmic-Ray and Neutrino Emissions from Magnetar-powered Superluminous Transients.” In: *ApJ* 878.1, 34 (June 2019), p. 34. doi: [10.3847/1538-4357/ab1b72](https://doi.org/10.3847/1538-4357/ab1b72) (cited on page 43).
- [128] Anna Y. Q. Ho et al. “The Koala: A Fast Blue Optical Transient with Luminous Radio Emission from a Starburst Dwarf Galaxy at  $z = 0.27$ .” In: *ApJ* 895.1, 49 (May 2020), p. 49. doi: [10.3847/1538-4357/ab8bcf](https://doi.org/10.3847/1538-4357/ab8bcf) (cited on page 43).
- [129] M. G. Aartsen et al. “All-sky Search for Time-integrated Neutrino Emission from Astrophysical Sources with 7 yr of IceCube Data.” In: *ApJ* 835.2, 151 (Feb. 2017), p. 151. doi: [10.3847/1538-4357/835/2/151](https://doi.org/10.3847/1538-4357/835/2/151) (cited on page 44).
- [130] Robert Stein et al. “A tidal disruption event coincident with a high-energy neutrino.” In: *Nature Astronomy* (Feb. 2021). doi: [10.1038/s41550-020-01295-8](https://doi.org/10.1038/s41550-020-01295-8) (cited on pages 49, 50).
- [131] R. Stein. “IceCube-191001A - IceCube observation of a high-energy neutrino candidate event.” In: *GCN Circular* 25913 (2019) (cited on pages 49, 50).
- [132] Robert Stein et al. “Candidate Counterparts to IceCube-191001A with ZTF.” In: *The Astronomer’s Telegram* 13160 (Oct. 2019), p. 1 (cited on page 49).
- [133] J. Nordin et al. “ZTF Transient Discovery Report for 2019-04-22.” In: *Transient Name Server Discovery Report* 2019-615 (Apr. 2019), p. 1 (cited on page 50).
- [134] Iain A. Steele et al. “The Liverpool Telescope: performance and first results.” In: *Proc. SPIE*. Ed. by Jr. Oschmann Jacobus M. Vol. 5489. Society of Photo-Optical Instrumentation Engineers (SPIE) Conference Series. 2004, pp. 679–692. doi: [10.1117/12.551456](https://doi.org/10.1117/12.551456) (cited on page 51).
- [135] N. Blagorodnova et al. “The SED Machine: A Robotic Spectrograph for Fast Transient Classification.” In: *PASP* 130.3 (Mar. 2018), p. 035003 (cited on page 51).
- [136] Peter W. A. Roming et al. “The Swift Ultra-Violet/Optical Telescope.” In: *Space Sci. Rev.* 120.3-4 (Oct. 2005), pp. 95–142. doi: [10.1007/s11214-005-5095-4](https://doi.org/10.1007/s11214-005-5095-4) (cited on page 51).
- [137] N. Gehrels et al. “The Swift Gamma-Ray Burst Mission.” In: *ApJ* 611.2 (Aug. 2004), pp. 1005–1020. doi: [10.1086/422091](https://doi.org/10.1086/422091) (cited on page 51).
- [138] Andrew Mummery and Steven A. Balbus. “The spectral evolution of disc dominated tidal disruption events.” In: *MNRAS* 492.4 (Mar. 2020), pp. 5655–5674. doi: [10.1093/mnras/staa192](https://doi.org/10.1093/mnras/staa192) (cited on pages 51, 52).

- [139] S. van Velzen et al. “Discovery of Transient Infrared Emission from Dust Heated by Stellar Tidal Disruption Flares.” In: *ApJ* 829.1, 19 (Sept. 2016), p. 19. doi: [10.3847/0004-637X/829/1/19](https://doi.org/10.3847/0004-637X/829/1/19) (cited on page 51).
- [140] David N. Burrows et al. “The Swift X-Ray Telescope.” In: *Space Sci. Rev.* 120.3-4 (Oct. 2005), pp. 165–195. doi: [10.1007/s11214-005-5097-2](https://doi.org/10.1007/s11214-005-5097-2) (cited on page 51).
- [141] F. Jansen et al. “XMM-Newton observatory. I. The spacecraft and operations.” In: *A&A* 365 (Jan. 2001), pp. L1–L6. doi: [10.1051/0004-6361:20000036](https://doi.org/10.1051/0004-6361:20000036) (cited on page 51).
- [142] Nicholas J. McConnell and Chung-Pei Ma. “Revisiting the Scaling Relations of Black Hole Masses and Host Galaxy Properties.” In: *ApJ* 764.2, 184 (Feb. 2013), p. 184. doi: [10.1088/0004-637X/764/2/184](https://doi.org/10.1088/0004-637X/764/2/184) (cited on page 53).
- [143] R. A. Perley et al. “The Expanded Very Large Array: A New Telescope for New Science.” In: *ApJ* 739.1, L1 (Sept. 2011), p. L1. doi: [10.1088/2041-8205/739/1/L1](https://doi.org/10.1088/2041-8205/739/1/L1) (cited on page 53).
- [144] J. T. L. Zwart et al. “The Arcminute Microkelvin Imager.” In: *MNRAS* 391.4 (Dec. 2008), pp. 1545–1558. doi: [10.1111/j.1365-2966.2008.13953.x](https://doi.org/10.1111/j.1365-2966.2008.13953.x) (cited on page 53).
- [145] J. L. Jonas. “MeerKAT - The South African Array With Composite Dishes and Wide-Band Single Pixel Feeds.” In: *IEEE Proceedings* 97.8 (Aug. 2009), pp. 1522–1530. doi: [10.1109/JPROC.2009.2020713](https://doi.org/10.1109/JPROC.2009.2020713) (cited on page 53).
- [146] Daniel Foreman-Mackey et al. “emcee: The MCMC Hammer.” In: *PASP* 125.925 (Mar. 2013), p. 306. doi: [10.1086/670067](https://doi.org/10.1086/670067) (cited on page 54).
- [147] Rodolfo Barniol Duran, Ehud Nakar, and Tsvi Piran. “Radius Constraints and Minimal Equipartition Energy of Relativistically Moving Synchrotron Sources.” In: *ApJ* 772.1, 78 (July 2013), p. 78. doi: [10.1088/0004-637X/772/1/78](https://doi.org/10.1088/0004-637X/772/1/78) (cited on page 54).
- [148] G. Morlino and D. Caprioli. “Strong evidence for hadron acceleration in Tycho’s supernova remnant.” In: *A&A* 538, A81 (Feb. 2012), A81. doi: [10.1051/0004-6361/201117855](https://doi.org/10.1051/0004-6361/201117855) (cited on pages 55, 64).
- [149] Jonathan Granot and Alexander J. van der Horst. “Gamma-Ray Burst Jets and their Radio Observations.” In: *PASA* 31, e008 (Feb. 2014), e008. doi: [10.1017/pasa.2013.44](https://doi.org/10.1017/pasa.2013.44) (cited on page 55).
- [150] W. Fong et al. “A Decade of Short-duration Gamma-Ray Burst Broadband Afterglows: Energetics, Circumburst Densities, and Jet Opening Angles.” In: *ApJ* 815.2, 102 (Dec. 2015), p. 102. doi: [10.1088/0004-637X/815/2/102](https://doi.org/10.1088/0004-637X/815/2/102) (cited on page 55).
- [151] Assaf Horesh et al. “An early and comprehensive millimetre and centimetre wave and X-ray study of SN 2011dh: a non-equipartition blast wave expanding into a massive stellar wind.” In: *MNRAS* 436.2 (Dec. 2013), pp. 1258–1267. doi: [10.1093/mnras/stt1645](https://doi.org/10.1093/mnras/stt1645) (cited on page 55).
- [152] T. Eftekhari et al. “Radio Monitoring of the Tidal Disruption Event Swift J164449.3+573451. III. Late-time Jet Energetics and a Deviation from Equipartition.” In: *ApJ* 854.2, 86 (Feb. 2018), p. 86. doi: [10.3847/1538-4357/aaa8e0](https://doi.org/10.3847/1538-4357/aaa8e0) (cited on page 55).
- [153] A. G. Polatidis and J. E. Conway. “Proper Motions in Compact Symmetric Objects.” In: *PASA* 20.1 (Jan. 2003), pp. 69–74. doi: [10.1071/AS02053](https://doi.org/10.1071/AS02053) (cited on page 55).
- [154] K. D. Alexander et al. “Discovery of an Outflow from Radio Observations of the Tidal Disruption Event ASASSN-14li.” In: *ApJ* 819.2, L25 (Mar. 2016), p. L25. doi: [10.3847/2041-8205/819/2/L25](https://doi.org/10.3847/2041-8205/819/2/L25) (cited on pages 55, 56).
- [155] Julian Krolik et al. “ASASSN-14li: A Model Tidal Disruption Event.” In: *ApJ* 827.2, 127 (Aug. 2016), p. 127. doi: [10.3847/0004-637X/827/2/127](https://doi.org/10.3847/0004-637X/827/2/127) (cited on pages 55, 56, 64).
- [156] Dheeraj R. Pasham and Sjoert van Velzen. “Discovery of a Time Lag between the Soft X-Ray and Radio Emission of the Tidal Disruption Flare ASASSN-14li: Evidence for Linear Disk-Jet Coupling.” In: *ApJ* 856.1, 1 (Mar. 2018), p. 1. doi: [10.3847/1538-4357/aab361](https://doi.org/10.3847/1538-4357/aab361) (cited on page 56).
- [157] W. B. Atwood, A. A. Abdo, M. Ackermann, et al. “The Large Area Telescope on the Fermi Gamma-Ray Space Telescope Mission.” In: *ApJ* 697 (June 2009), pp. 1071–1102. doi: [10.1088/0004-637X/697/2/1071](https://doi.org/10.1088/0004-637X/697/2/1071) (cited on page 56).

- [158] Simone Garrappa and Sara Buson. “Fermi-LAT Gamma-ray Observations of IceCube-191001A.” In: *GCN Circular* 25932 (2019) (cited on pages 56, 57).
- [159] The Fermi-LAT collaboration. “Fermi Large Area Telescope Fourth Source Catalog.” In: *arXiv e-prints*, arXiv:1902.10045 (Feb. 2019), arXiv:1902.10045 (cited on page 56).
- [160] Tapio Pursimo et al. “The Micro-Arcsecond Scintillation-Induced Variability (MASIV) Survey. III. Optical Identifications and New Redshifts.” In: *ApJ* 767.1, 14 (Apr. 2013), p. 14. doi: [10.1088/0004-637X/767/1/14](https://doi.org/10.1088/0004-637X/767/1/14) (cited on page 57).
- [161] C. Diltz, M. Böttcher, and G. Fossati. “Time Dependent Hadronic Modeling of Flat Spectrum Radio Quasars.” In: *ApJ* 802.2, 133 (Apr. 2015), p. 133. doi: [10.1088/0004-637X/802/2/133](https://doi.org/10.1088/0004-637X/802/2/133) (cited on page 57).
- [162] Shan Gao et al. “Modelling the coincident observation of a high-energy neutrino and a bright blazar flare.” In: *Nature Astronomy* 3 (Jan. 2019), pp. 88–92. doi: [10.1038/s41550-018-0610-1](https://doi.org/10.1038/s41550-018-0610-1) (cited on page 57).
- [163] Hugo Ayala. “IceCube-191001A: HAWC follow-up.” In: *GCN Circular* 25936 (2019) (cited on page 57).
- [164] M. Nicholl et al. “ePESSTO+ classification of optical transients.” In: *The Astronomer’s Telegram* 12752 (May 2019), p. 1 (cited on pages 58, 59).
- [165] J. S. Miller and R. P. S. Stone. *Lick Obs. Tech. Rep.* 66. Santa Cruz: Lick Obs., 1993 (cited on page 58).
- [166] J. B. Oke et al. “The Keck Low-Resolution Imaging Spectrometer.” In: *PASP* 107 (Apr. 1995), pp. 375–+. (cited on page 58).
- [167] Matthew J. Graham et al. “The Zwicky Transient Facility: Science Objectives.” In: *PASP* 131.1001 (July 2019), p. 078001. doi: [10.1088/1538-3873/ab006c](https://doi.org/10.1088/1538-3873/ab006c) (cited on page 60).
- [168] A. M. Hillas. “The Origin of Ultra-High-Energy Cosmic Rays.” In: *ARA&A* 22 (Jan. 1984), pp. 425–444. doi: [10.1146/annurev.aa.22.090184.002233](https://doi.org/10.1146/annurev.aa.22.090184.002233) (cited on page 62).
- [169] Nicholas Senno, Kohta Murase, and Peter Mészáros. “High-energy Neutrino Flares from X-Ray Bright and Dark Tidal Disruption Events.” In: *ApJ* 838.1, 3 (Mar. 2017), p. 3. doi: [10.3847/1538-4357/aa6344](https://doi.org/10.3847/1538-4357/aa6344) (cited on page 62).
- [170] Cecilia Lunardini and Walter Winter. “High energy neutrinos from the tidal disruption of stars.” In: *Phys. Rev. D* 95.12, 123001 (June 2017), p. 123001. doi: [10.1103/PhysRevD.95.123001](https://doi.org/10.1103/PhysRevD.95.123001) (cited on page 62).
- [171] S. Hümer et al. “Simplified Models for Photohadronic Interactions in Cosmic Accelerators.” In: *ApJ* 721.1 (Sept. 2010), pp. 630–652. doi: [10.1088/0004-637X/721/1/630](https://doi.org/10.1088/0004-637X/721/1/630) (cited on page 63).
- [172] Eli Waxman and John Bahcall. “High energy neutrinos from astrophysical sources: An upper bound.” In: *Phys. Rev. D* 59.2, 023002 (Jan. 1999), p. 023002. doi: [10.1103/PhysRevD.59.023002](https://doi.org/10.1103/PhysRevD.59.023002) (cited on page 63).
- [173] Walter Winter and Cecilia Lunardini. “A concordance scenario for the observed neutrino from a tidal disruption event.” In: *Nature Astronomy* (Feb. 2021). doi: [10.1038/s41550-021-01305-3](https://doi.org/10.1038/s41550-021-01305-3) (cited on page 65).
- [174] Ruo-Yu Liu, Shao-Qiang Xi, and Xiang-Yu Wang. “Neutrino emission from an off-axis jet driven by the tidal disruption event AT2019dsg.” In: *Phys. Rev. D* 102.8, 083028 (Oct. 2020), p. 083028. doi: [10.1103/PhysRevD.102.083028](https://doi.org/10.1103/PhysRevD.102.083028) (cited on page 65).
- [175] Kohta Murase et al. “High-energy Neutrino and Gamma-Ray Emission from Tidal Disruption Events.” In: *ApJ* 902.2, 108 (Oct. 2020), p. 108. doi: [10.3847/1538-4357/abb3c0](https://doi.org/10.3847/1538-4357/abb3c0) (cited on page 65).
- [176] ANTARES Collaboration et al. “Search for neutrinos from the tidal disruption events AT2019dsg and AT2019fdr with the ANTARES telescope.” In: *arXiv e-prints*, arXiv:2103.15526 (Mar. 2021), arXiv:2103.15526 (cited on page 65).
- [177] R. Stein. “Search for High-Energy Neutrinos from Populations of Optical Transients.” In: *36th International Cosmic Ray Conference (ICRC2019)*. Vol. 36. International Cosmic Ray Conference. July 2019, 1016, p. 1016 (cited on pages 66, 67).

- [178] Pan-Starrs Collaboration et al. “Search for transient optical counterparts to high-energy IceCube neutrinos with Pan-STARRS1.” In: *A&A* 626, A117 (June 2019), A117. doi: [10.1051/0004-6361/201935171](https://doi.org/10.1051/0004-6361/201935171) (cited on page 66).
- [179] Fang-Kun Peng, Qing-Wen Tang, and Xiang-Yu Wang. “Search for High-energy Gamma-ray Emission from Tidal Disruption Events with the Fermi Large Area Telescope.” In: *ApJ* 825.1, 47 (July 2016), p. 47. doi: [10.3847/0004-637X/825/1/47](https://doi.org/10.3847/0004-637X/825/1/47) (cited on page 67).
- [180] Xiang-Yu Wang and Ruo-Yu Liu. “Tidal disruption jets of supermassive black holes as hidden sources of cosmic rays: Explaining the IceCube TeV-PeV neutrinos.” In: *Phys. Rev. D* 93.8, 083005 (Apr. 2016), p. 083005. doi: [10.1103/PhysRevD.93.083005](https://doi.org/10.1103/PhysRevD.93.083005) (cited on page 67).
- [181] Kohta Murase, Dafne Guetta, and Markus Ahlers. “Hidden Cosmic-Ray Accelerators as an Origin of TeV-PeV Cosmic Neutrinos.” In: *Phys. Rev. Lett.* 116.7, 071101 (Feb. 2016), p. 071101. doi: [10.1103/PhysRevLett.116.071101](https://doi.org/10.1103/PhysRevLett.116.071101) (cited on page 67).

## Greek Letters with Pronunciations

Character	Name	Character	Name
$\alpha$	alpha <i>AL-fuh</i>	$\nu$	nu <i>NEW</i>
$\beta$	beta <i>BAY-tuh</i>	$\xi, \Xi$	xi <i>KSIGH</i>
$\gamma, \Gamma$	gamma <i>GAM-muh</i>	$\omicron$	omicron <i>OM-uh-CRON</i>
$\delta, \Delta$	delta <i>DEL-tuh</i>	$\pi, \Pi$	pi <i>PIE</i>
$\epsilon$	epsilon <i>EP-suh-lon</i>	$\rho$	rho <i>ROW</i>
$\zeta$	zeta <i>ZAY-tuh</i>	$\sigma, \Sigma$	sigma <i>SIG-muh</i>
$\eta$	eta <i>AY-tuh</i>	$\tau$	tau <i>TOW (as in cow)</i>
$\theta, \Theta$	theta <i>THAY-tuh</i>	$v, \text{Y}$	upsilon <i>OOP-suh-LON</i>
$\iota$	iota <i>eye-OH-tuh</i>	$\phi, \Phi$	phi <i>FEE, or FI (as in hi)</i>
$\kappa$	kappa <i>KAP-uh</i>	$\chi$	chi <i>KI (as in hi)</i>
$\lambda, \Lambda$	lambda <i>LAM-duh</i>	$\psi, \Psi$	psi <i>SIGH, or PSIGH</i>
$\mu$	mu <i>MEW</i>	$\omega, \Omega$	omega <i>oh-MAY-guh</i>

Capitals shown are the ones that differ from Roman capitals.

# **Alphabetical Index**

preface, v